



Final Report

Hybrid Oxides for Thermoelectric and Piezoelectric Energy Applications

By Panupong Jaiban

Final Report

Hybrid Oxides for Thermoelectric and Piezoelectric Energy Applications

Panupong Jaiban King Mongkut's University of Technology North Bangkok

Project Granted by the Thailand Research Fund and Office of the Higher Education Commission

บทคัดย่อ

รหัสโครงการ: MRG6180109

ชื่อโครงการ: ไฮบริดออกไซด์สำหรับการประยุกต์ใช้งานด้านพลังงานเทอร์โมอิเล็กทริกและ

ไพอิโซอิเล็กทริก

ชื่อนักวิจัย และสถาบัน ผู้ช่วยศาสตราจารย์ ดร.ภาณุพงศ์ ใจบาล

มหาวิทยาลัยเทคโนโลยีพระจอมเกล้าพระนครเหนือ

อีเมล์: panupong.j@sciee.kmutnb.ac.th

ระยะเวลาโครงการ: 2 พฤษภาคม 2561 – 31 สิงหาคม 2562

บทคัดย่อ:

โครงการวิจัยนี้ได้เตรียมเซรามิกออกไซด์ไฮบริดระหว่างวัสดุไพอิโซอิเล็กทริกและเทอร์ โมอิเล็กทริกด้วยกระบวนการเผาผนึกแบบดั่งเดิม เซรามิกออกไซด์แบบไฮบริดสามารถแบ่งออก ได้เป็น 3 ระบบ ได้แก่ ระบบแบเรียมแคลเซียมเซอร์โคเนตไททาเนต-โคบอลไลต์ (BCZT-CCO), ระบบแบเรียมแคลเซียมเซอร์โคเนตไททาเนต-แคลเซียมแมงกาเนต (BCZT-CMNO) และระบบแบเรียมแคลเซียมเซอร์โคเนตไททาเนต-ซิงค์ออกไซด์ (BCZT-ZAO) สภาวะอุณหภูมิ การเผาผนึกที่เหมาะสมขึ้นอยู่กับแต่ละระบบ โดยอยู่ในช่วงอุณหภูมิจาก 1,050 ถึง1,350 °C ลักษณะรูปแบบการเลี้ยวเบนของรังสีเอกซ์ของเซรามิกแสดงให้เห็นว่าลักษณะเฟสของไฮบริด ออกไซด์เป็นสารละลายของแข็ง และคอมโพสิต ที่ขึ้นอยู่กับแต่ละส่วนผสม การเติม CCO, CMNO, และ ZAO ส่งผลต่อลักษณะโครงสร้างจุลภาค ขนาดเกรนเฉลี่ย และการกระจายตัวของ ขนาดเกรน ของออกไซด์ใฮบริด ผลการดูดซับรังสีเอกซ์ (XAS) และการปลดปล่อยอิเล็กตรอน จากรังสีเอกซ์ (XPS) แสดงให้เห็นถึงการบิดเบี้ยวทางโครงสร้างผลึก และสถานะทางไฟฟ้าของ แต่ละธาตุในออกไซด์เซรามิก โดยเซรามิกออกไซด์ไฮบริดสามารถแสดงสมบัติทางเพียโซอิ เล็กทริกหรือเทอร์โมอิเล็กทริกได้อย่างใดอย่างหนึ่งเท่านั้น เนื่องจากสภาพการนำไฟฟ้าของ เซรามิกออกไซด์ อย่างไรก็ตาม การศึกษาในโครงการวิจัยนี้ พบว่า ระบบเซรามิกไฮบริด BCZT-CCO สามารถแสดงสมบัติทางใดอิเล็กทริก และเทอร์โมอิเล็กทริกได้ดีกว่าเซรามิกระบบ BCZT-CMNO และ BCZT-ZAO คาดว่า ข้อมูลใหม่ที่เกี่ยวข้องกับเซรามิกออกไซด์ไฮบริด เหล่านี้ จะเป็นประโยชน์อย่างยิ่งสำหรับนักวิจัยที่สนใจทางด้านวัสดุไพอิโซอิเล็กทริก และเทอร์ โมอิเล็กทริก

คำหลัก :

ออกไซด์ใฮบริด, วัสดุไฮบริดเพียโซอิเล็กทริกและเทอร์โมอิเล็กทริก, BCZT-CCO, BCZT-CMNO, BCZT-ZAO **Abstract**

Project Code: MRG6180109

Project Title: Hybrid Oxides for Thermoelectric and Piezoelectric Energy Applications

Investigator: Assistant Professor Dr. Panupong Jaiban

E-mail Address: p.jaiban@gmail.com

Project Period: 2 May 2018 - 31 August 2019

Abstract:

In this work, the hybrid oxides of piezoelectric and thermoelectric materials were fabricated using solid-state sintering process. The hybrid oxides were composed of three systems, which were barium calcium zirconate titanate-calcium cobolite (BCZT-CCO), barium calcium zirconate titanate-calcium manganate (BCZT-CMNO), and barium calcium zirconate titanate-zinc oxide (BCZT-ZAO). The optimized sintering condition for BCZT-CCO, BCZT-CMNO, and BCZT-ZAO was ranged from 1,050 to 1,350 °C, dependent on each system. X-ray diffraction patterns indicated that the solid solution and composite phase, which depending on each composition. The increase in CCO, CMNO, and ZAO concentration affected their microstructure, grain size, and grain size distribution. The local structure and oxidation state of each element were revealed by Xray absorption spectroscopy (XAS) and X-ray photoemission spectroscopy (XPS). The ceramics could respond either piezoelectricity or thermoelectricity due to their electrical conductivity. However, with these ceramics, we found that BCZT-CCO has promoted the dielectric and thermoelectric response better than another system. The new information relating to these hybrid oxides would be useful for researcher, who are interested in piezoelectric and thermoelectric materials.

Keywords:

Hybrid oxide, Hybrid thermoelectric and piezoelectric materials, BCZT-CCO, BCZT-CMNO, BCZT-ZAO

Executive Summary

1. Introduction to the research problem and its significance

Nowadays, energy consumption keeps increasing due to a rapid increase of population around the world. The energy produced from petroleum and fossil-fuel resource may be insufficient for our demand in the near future. Therefore, this problem becomes hot issue and a challenge for scientists and researchers to find an alternative energy reserve. The power from solar, wind, water, fuel cell and bio-mass system are a well-known alternative energy. Beside these energy sources, it is found that waste-heat at high temperature (600 to 1500 K) from boilers, furnaces and automobile vehicles and a vibrational power from human and automotive motions can be another alternative energy source. Although their power generation capability is in order of milliwatt to watts which are quite low as compared with those of other well-known resources that can produce power in kilowatt to megawatt range, the electric power from heat and vibration is considered to become potential candidate for future energy applications. This is therefore the main focus of this project in which the utilization of both waste-heat and vibrational energy sources. The materials which can convert thermal gradient and applied mechanical energy to electricity are called "thermoelectric" and "piezoelectric", respectively.

Among thermoelectric ceramics, thermoelectric oxides i.e. Ca₃Co₄O₉ (CCO), CaMnNbO₃ (CMNO) and ZnAlO (ZAO) are suitable choices for such thermal energy harvesting because their stability at high temperature and nontoxicity. In case of piezoelectric ceramics, Ba_{0.85}Ca_{0.15}Zr_{0.1}Ti_{0.9}O₃ (BCZT) lead-free oxide ceramic can be a potential candidate for mechanical energy harvesting since its piezoelectric performance is comparable to a commercial lead-based materials and it is also non-toxic. However, electric power generation of these materials is quite low (in order of milliwatt to watt) as compared with those of alternative sources. Thus, enhancement in their energy efficiency is still an attractive challenge.

In this project, the hybrid oxide materials can be divided into three systems including Ca₃Co₄O₉-Ba_{0.85}Ca_{0.15}Zr_{0.1}Ti_{0.9}O₃ (CCO-BCZT), CaMnNbO₃-Ba_{0.85}Ca_{0.15}Zr_{0.1}Ti_{0.9}O₃ (CMNO-BCZT) and ZnAlO-Ba_{0.85}Ca_{0.15}Zr_{0.1}Ti_{0.9}O₃ (ZAO-BCZT). BCZT composing of large ions of barium and having low thermal conductivity due to phonon scattering contribution may induce a decrease of the total thermal conductivity in hybrid material. Beside thermal contribution, electrical conduction of BCZT increases rapidly at high temperature. This may improve electrical conductivity of hybrid material.

Thermoelectric performance of hybrid system may possibly be enhanced if Seebeck coefficient does not significantly change. In case of CCO, CMNO and ZAO, the structural difference of these thermoelectric materials on BCZT is expected to produce a change in structural deformation and microstructure of the latter, affecting directly its polarization behavior and domain wall mobility, respectively. Moreover, the different oxidation state of each element in these oxides can induce creation of structural defects which may enhance piezoelectric performance of hybrid materials. It is expected that the result from crystal structure together with local structure in this project can reflect changes in thermoelectric and piezoelectric response of these hybrid systems. This would become the original knowledge involving thermoelectric-piezoelectric materials. It is believed that combination of thermoelectric and piezoelectric materials at suitable composition could give better energy efficiency for further application in simultaneous energy harvesting from both waste-heat and vibrational energy. The fabrication and the studied properties of these hybrid oxide materials would give a new knowledge in Thailand and increase skill of scientists and researchers participating in this project. Moreover, this will also be of interest to large scientific community which will encourage them to get more involved in waste-heat and vibrational alternative energy area.

2. Literature review

2.1 Thermoelectric materials

Thermoelectric material can make the direct conversion of heat energy to electrical energy (so-called Seebeck effect). Also, electrical energy can be transformed to thermal gradient by the same material (i.e. Peltier effect). There are two types of thermoelectric components employed in each system for electrical and thermal conduction; those having positive charge carriers (p-type) and negative charge carriers (n-type). Figure 1 shows the principle of Seebeck and Peltier effects in thermoelectric devices. Regarding Seebeck effect, upon thermal gradient, movement of electrons and holes to cool side induces electricity. Meanwhile, when an external electric field is applied, heat energy is absorbed at the top surface and released to other side by charge carriers through electrical current, causing creation of thermal gradient (Peltier effect). This provides a route to solid-state heating or refrigeration.

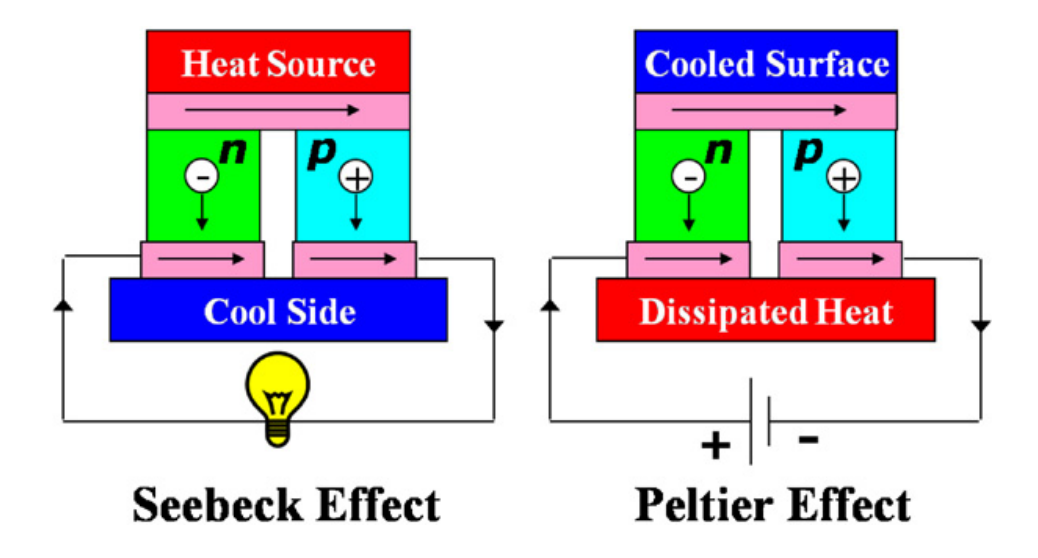


Figure 1. Principle of thermoelectric devices [1].

The generation of voltage due to temperature gradient by Seebeck effect makes such thermoelectric material attractive and can be developed for alternative energy application. The important factors of thermoelectric properties relating application in energy harvesting are Seebeck coefficient, electrical conductivity and thermal conductivity. These three characteristics are captured in the dimensionless figure of merit (ZT), which is given by

$$ZT = \frac{S^2 \sigma T}{\kappa} \tag{1}$$

where σ is the electrical conductivity $((\Omega-cm)^{-1}), S$ is Seebeck coefficient $(\mu V/K)$, κ is thermal conductivity (W/(m-K)) and T is temperature. From the equation, it can be seen that thermoelectric materials possessing large ZT should have high Seebeck coefficient and electrical conductivity but thermal conductivity should be low. Beside the figure of merit, an efficiency in energy conversion (η) of thermoelectric materials can be expressed by

$$\eta = \frac{T_H - T_C}{T_H} \left[\frac{(1 + Z\overline{T})^{1/2} - 1}{(1 + Z\overline{T})^{1/2} + (T_C / T_H)} \right]$$
 (2)

where T_H and T_C is the temperature at hot and cool side, respectively. \overline{T} is an average temperature between hot and cool side. The materials having large thermoelectric performance should have ZT close to 1 or higher. The large ZT can be found in metal alloy compound including tellurium-, antinony- and germanium-based

compounds [1-6] (see Fig. 2). However the drawbacks of these compounds are instability at high temperature and their toxicity during operation. Hence, oxide thermoelectric has therefore been developed in order to replace these compounds for applications at high temperature since an oxide compound is quite stable at high temperature and does not produce toxicity [7].

Most of oxide thermoelectric materials are not conductive. Thus, their electrical conductivity is lower than non-oxide compounds. However, the feature of low thermal conductivity often results in an enhancement of their thermoelectric properties. Figure 3 displays possible application of several thermoelectric materials for waste-heat harvesting from automotive vehicles, boilers and furnace (corresponding to the temperature range from 600 to 1500 K). Regarding the impact on environment, oxide thermoelectric seems to be a good choice due to the fact they are relatively nonpoisonous for human and environment. Beside eco-benign aspect, they can also be used under normal atmosphere. This project therefore will pay attention to develop oxide thermoelectric material to enhance their thermoelectric performance.

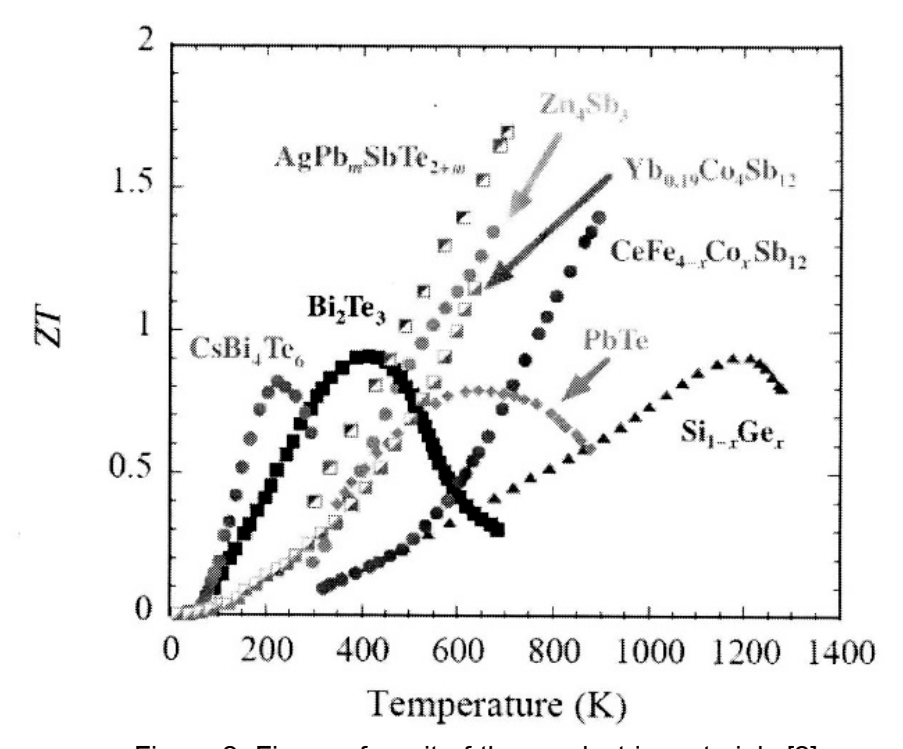


Figure 2. Figure of merit of thermoelectric materials [2]

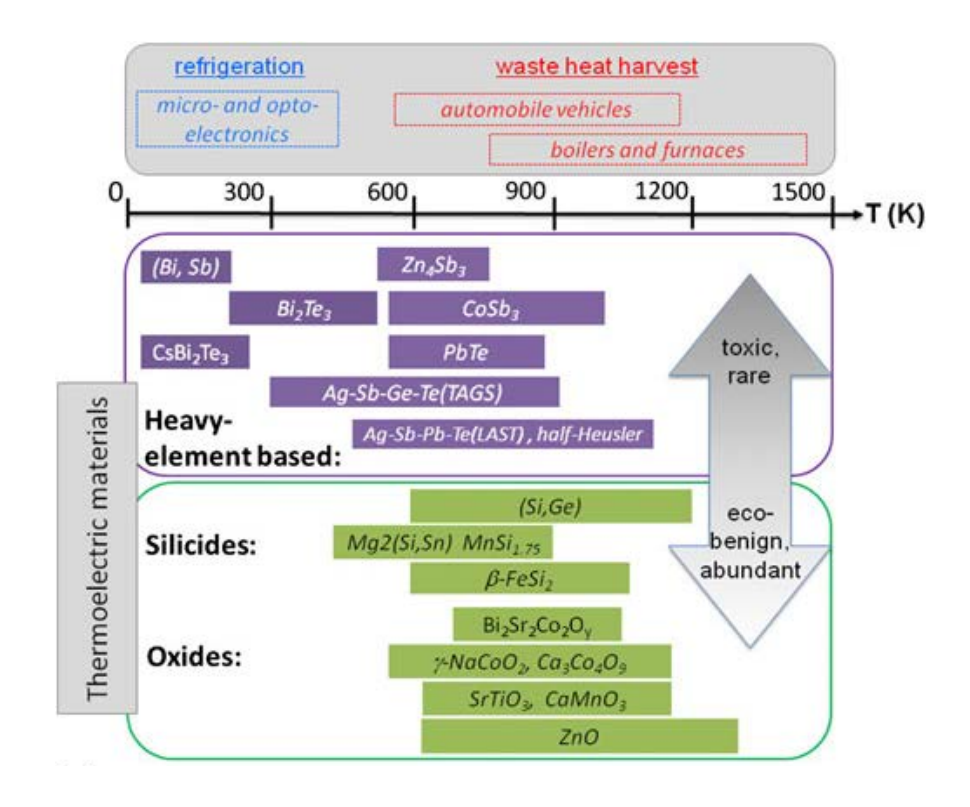


Figure 3. Application of thermoelectric material for energy harvesting [7].

ZT of p-type oxides and non-oxide thermoelectric materials are compared in Figure 4. Although thermoelectric properties of several non-oxide materials are better, oxide-based compounds should be alternative thermoelectric material due to their stability at high temperature and nontoxicity. Among p-type oxide thermoelectric, calcium cobaltite (Ca₃Co₄O₉) and sodium cobaltite (Na₂CoO₄) exhibit good ZT (\geq 0.4). It is believed that these compounds can become promising candidates of oxide material for p-type thermoelectric. However, the characteristic of sodium with volatility at high temperature and hygroscopicity of Na₂CoO₄ limit its application for electric power generation [9]. Although Na₂CoO₄ has better thermoelectric properties, Ca₃Co₄O₉ attracts more interest for this project due to its stability at high temperature and humidity resistance. Thus, this project would focus on Ca₃Co₄O₉ material. The compound is composed of two layers of CoO2 (Co atom is surrounded by six O atoms in octahedral configuration) and triple rock-salt structure of Ca₂CoO₃ layer (see Figure 5). Regarding the listed data in Table 1, thermal conductivity of Ca₃Co₄O₉ seems to be the main factor for dropped value of ZT as considered together with $Yb_{14}MnSb_{11}$ (ZT = 1). In general, heat transfer of solid is attributed to electronic mobility and lattice (phonons) contribution. In case of oxide, the thermal conduction is mainly due to phonon contribution. Li et al have enhanced thermoelectric performance of Ca₃Co₄O₉ by decreasing the thermal conductivity with larger ions substitution of bismuth (Bi) into Ca [15]. Similarly, Wang et al have decreased thermal conduction with addition of large mass of silver (Ag) [16]. However, ZT of Ca₃Co₄O₉ is still lower than non-oxide compounds. Beside decreasing thermal conductivity, Koshibae et al have suggested that this material can have large Seebeck coefficient attributed to the low spin state of Co³⁺ [17]. Variation in oxidation state of Co ions can occur from different oxygen content during fabrication, affecting thermoelectric properties of Ca₃Co₄O₉ [18]. So far, it is found that the focus on this aspect is quite scarce. Thus, an investigation in the local structure which reflects directly the oxidation state of Co ions is very attractive and worthwhile.

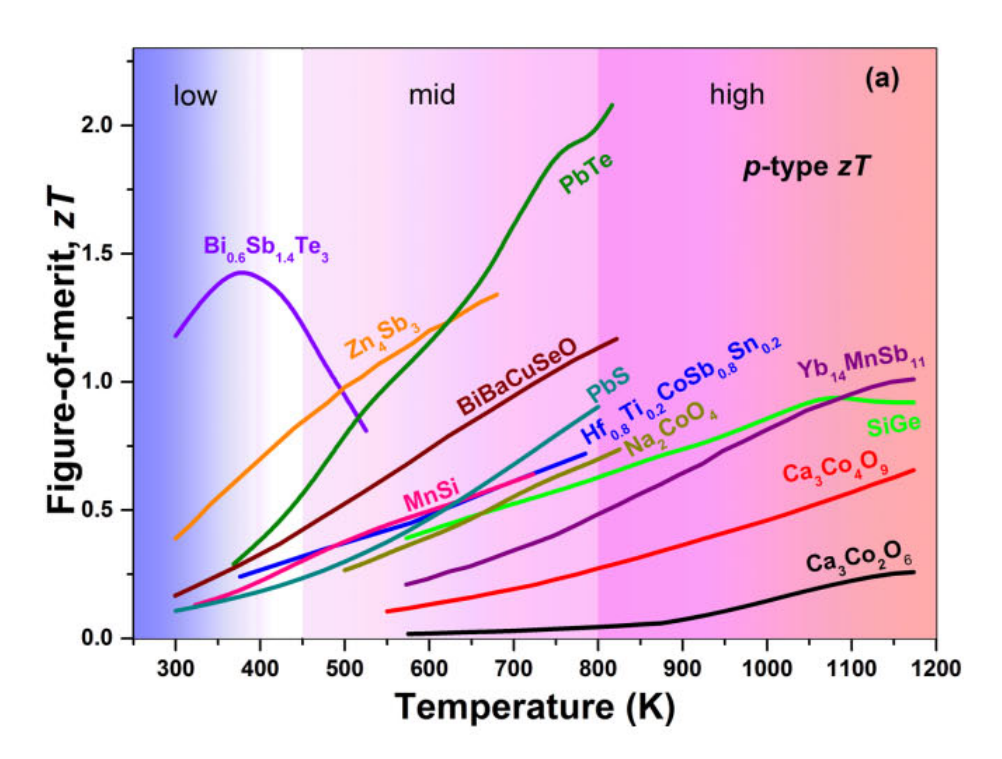


Figure 4. ZT of p-type thermoelectric materials [8].

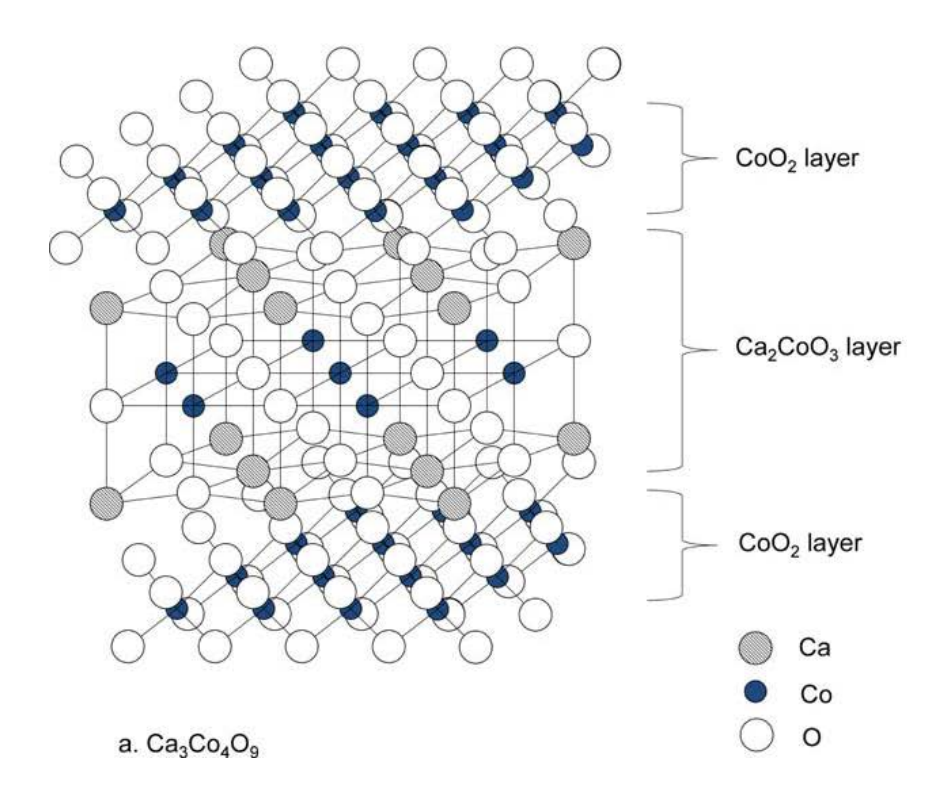


Figure 5. Structure of Ca₃Co₄O₉ material [10].

Table 1. The thermoelectric properties and ZT of p-type thermoelectric materials

	Materials	S ($\mu V/K$)	σ $(\Omega-cm)^{-1}$	$\mathbf{K}W/(m-K)$	ZT
p-	Yb ₁₄ MnSb ₁₁ [11]	185	185	0.7	~1 (1200 K)
type	0.23B-0.77Si _{0.8} Ge _{0.2}	168	820	4.1	~0.62 (1200
	[12]				K)
	Na _{1.5} Co _{1.8} Ag _{0.2} O ₄ [13]	101	152		
	LaCoO ₃ [14]	635	0.06		0.1
	La _{0.98} Sr _{0.02} CoO ₃ [14]	330	3.77		
	based-Ca ₃ Co ₄ O ₉ [10]	~180	~251	~1.7	~0.4 (1000 K)
	based-Na _x CoO ₂ [10]	~200	~316	~1.6	~0.8 (950 K)

In case of n-type thermoelectric, a large ZT of oxide materials can be found in calcium manganite (CaMnO₃), strontium titanate (SrTiO₃) and zinc oxide (ZnO), as shown in Figure 6. Thus, it is believed that these materials can become a promising candidate for n-type thermoelectric. In case of SrTiO₃, Koumoto et al suggest that this material degrades rapidly at the temperature above 700 K under normal atmosphere [9]. This indicates that SrTiO₃ may be suitable for power generation at low temperature

(from 300 to 500 K). This project is however focusing on high temperature thermoelectric materials. Thus, ZnO and $CaMnO_3$ are selected for a detailed study in this project.

ZnO is an oxide material with wurtzite structure as shown in Figure 7. As seen in Table 2, this material shows large ZT (~0.6) because it has relatively large Seebeck coefficient and high electrical conductivity. However, the primary drawback of this material is its high thermal conductivity as compared with other oxide materials. The microstructural feature seems to affect significantly the thermal conduction characteristic and electrical conductivity of ZnO as suggested by Ohtaki et al [22]. Moreover, Kinemuchi et al have found that the figure of merit becomes better for large grains [23]. These results indicate the governance of microstructure on thermoelectric properties of ZnO. Thus, it is believed that microstructural investigation in this project will give more understanding on thermoelectric performance of ZnO.

CaMnO₃ compound possesses perovskite structure (see Fig. 8). With the structure formula ABO3, the A site is at the corner of the cube while B is octahedrally coordinated by oxygen. As seen in Table 2, it is found that this material has good ZT (~0.2). Due to its rather low Seebeck coefficient and electrical conductivity, the feature of low thermal conductivity should be the most significant factor promoting a good ZT. Thus, most researches tend to increase the magnitude of Seebeck coefficient and electrical conductivity [10]. It is well known that electrical properties of perovskite material can be changed by creation of structural defects with aliovalent substitution. Wang et al have enhanced ZT of modified CaMnO₃ by co-doping of ytterbium (Yb) and dysprosium (Dy) ions, causing an increase of Seebeck coefficient and decrease of thermal conductivity [25]. With another ion doping, niobium (Nb) substitution into manganese (Mn) site lead to an improvement of electrical conductivity (donor doping) and decrease thermal conductivity, as found by Xu et al [26]. Beside enhancement of ZT, Koshibae et al have suggested that different oxidation state of transition metals dominates the intrinsic transport which enhances thermopower in lightly doped systems [17]. The focus on oxidation state and structural deformation on thermoelectric performance of CaMnO₃ is quite scarce. Thus, it is believed that an investigation in the local structure of this material would give further insight on factors affecting thermoelectric performance of CaMnO₃.

Recently, Funahashi et al have developed thermoelectric modules composing of 108 pairs of p-type Ca_{2.7}Bi_{0.3}CoO₉ and n-type Ca_{0.9}Yb_{0.1}MnO₃ legs [27]. The module can generate up to 13 V and 12 W of open circuit voltage and maximum power,

respectively, at 873 K of the hot end temperature of the oxide device [4]. Meanwhile, Hung et al have developed thermoelectric modules composing of $Ca_3Co_4O_{9+}\delta$ as p-leg and $Zn_{0.98}Al_{0.02}O$ as n-leg. The output power density can be generated up to 6.5 kW/m² at a temperature difference of 700 K [8]. These investigations have exhibited the possible energy application of $Ca_3Co_4O_9$, $CaMnO_3$ and ZnO materials for energy harvesting device. It is believed that knowledge relating to these materials in this project would be useful for development of energy harvesting device in the future.

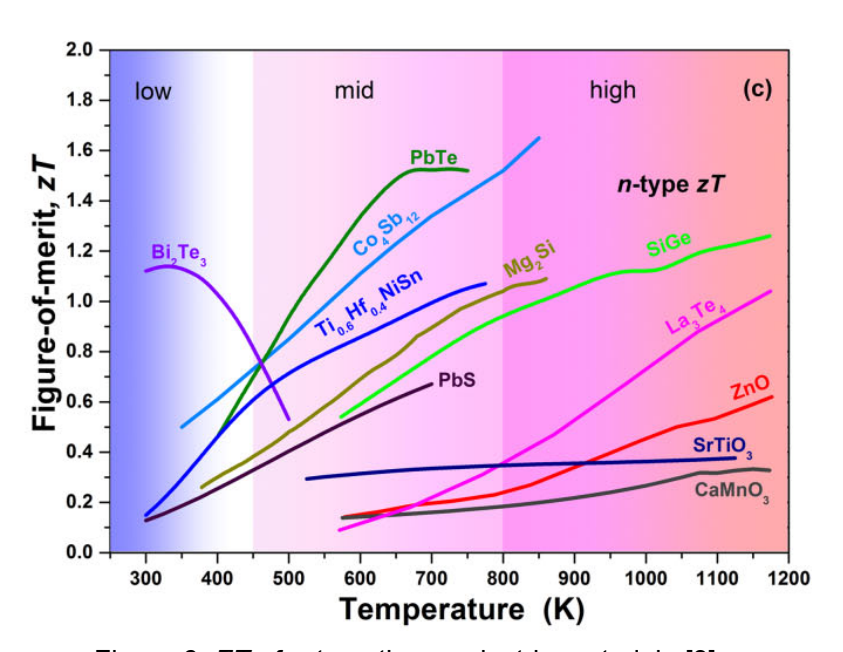


Figure 6. ZT of n-type thermoelectric materials [8].

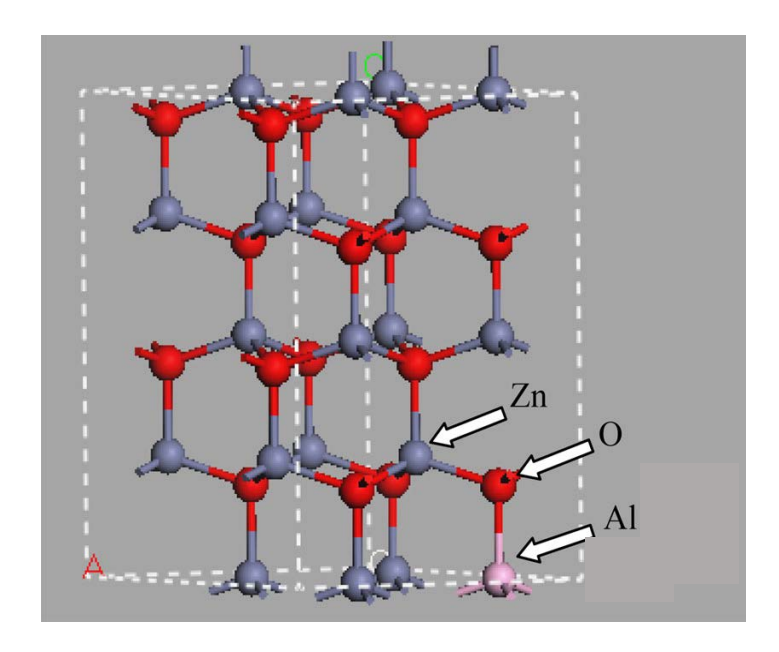


Figure 7. Structure of ZnO [19].

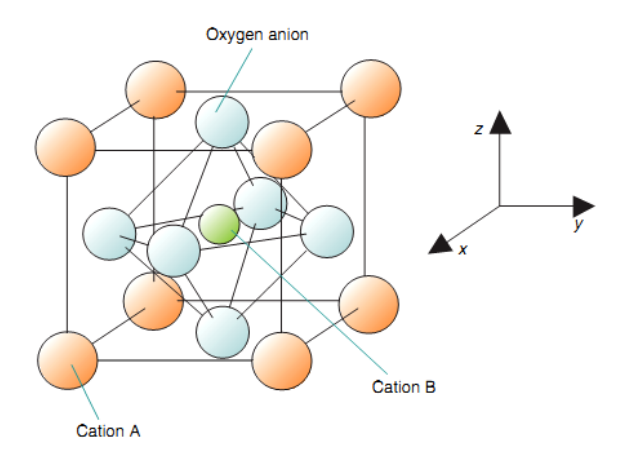


Figure 8. Structure of ABO₃ perovskite [24].

Table 2. The thermoelectric properties and ZT of n-type thermoelectric materials

	Materials	S $(\mu V/K)$	σ $(\Omega - cm)^{-1}$	K $W/(m-K)$	ZT
n-	Bi ₂ Te ₃ [20]	-200	1000		1.2
type	0.59P-0.41Si _{0.8} Ge _{0.2}	-171	1351	4.2	1.15 (1200 K)
	[12]				
	based SrTiO ₃ [10]	-260	250	3.1	~0.35 (1050
					K)
	Sr _{0.9} Dy _{0.1} TiO ₃ [21]	-190	357	2.6	0.22 (573 K)
	$Sr_xBa_{1-x}Nb_2O_{6-\delta}$ [1]	-147	323	2.28	0.17 (550 K)
	based-CaMnO ₃ [10]	-150	~130	1.5	~0.2 (1000 K)
	based-ZnO [10]	-250	~560	5	~0.6 (1100 K)

2.2 Piezoelectric materials

Piezoelectric materials can transform directly vibrational energy into electric energy as called "direct effect". Moreover, application of external electric field can induce its mechanical deformation known as "indirect effect" (see in Figure 9). Upon indirect effect, this material is widely used in several electronic devices such as sensor, actuator and fuel injection [28]. Beside application in electronic devices, the electricity generating characteristic when external force is applied makes this material attractive for mechanical energy harvesting. Piezoelectric material can be used at both non-resonant and resonant frequencies depending on each material. At non-resonant frequency, the figure of merit (FOM) of piezoelectric material for energy harvesting application is given by

$$FOM_{non-resonant} = d \cdot g \tag{3}$$

where d is piezoelectric coefficient (pC/N) and g is piezoelectric voltage coefficient (mV.m/N). From the equation, piezoelectric materials used for energy harvester should have large piezoelectric coefficient and voltage coefficient. In case of resonant frequency, FOM of piezoelectric material is given by

$$FOM_{resonant} = k^2 \cdot Q_m \tag{4}$$

where k is electromechanical coupling factor and \mathcal{Q}_m is mechanical quality factor. From the equation, it can be seen that piezoelectric material suitable for energy harvesting application at resonant frequency should have large electromechanical coupling factor and quality factor.

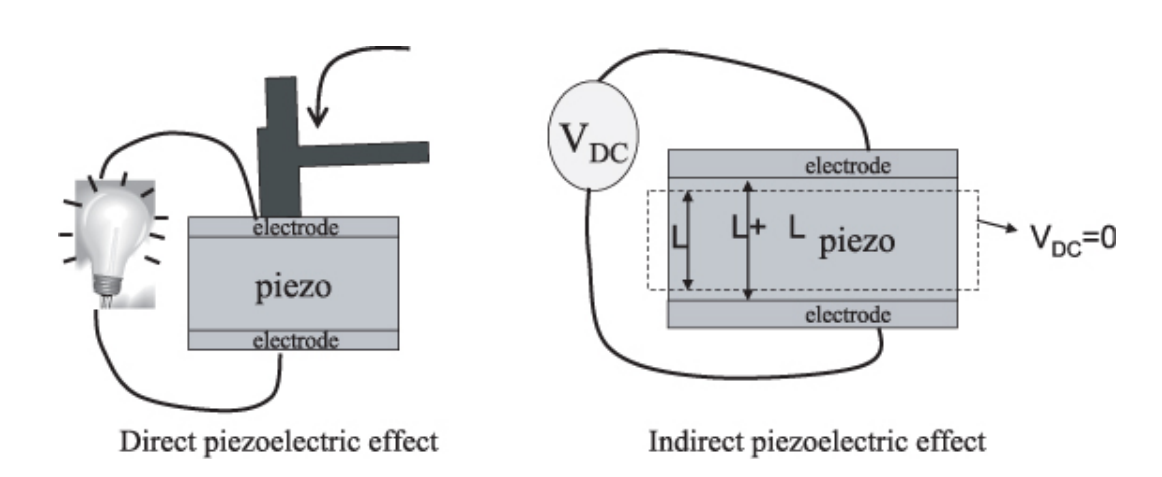


Figure 9. Direct and indirect effect of piezoelectric materials [29].

Lead zirconate titanate (PZT) is a well-known piezoelectric material and is widely used in many electronic devices. Due to its outstanding piezoelectric performance, Shen et al have used PZT cantilever for a low frequency vibration harvesting application. They found that the average power and power density from PZT were 0.32 W and 416 W/cm³ [30]. This indicates possible ability of piezoelectric materials for energy harvesting. However, the drawback of PZT compound is its toxicity because it is composed of heavy metal, affecting harmfully human and environment [31]. Thus, lead-free piezoelectric material has continuously been developed in order to replace PZT in current electronic devices. The quantitative data of piezoelectric properties and FOM between commercial material (PZT) and lead-free material are listed in Table 3. It is

found that potassium sodium niobate-based compound (KNN) exhibits promising figure of merit at resonant frequency (~726). This value is higher than that of PZT-8. However, it is found that the fabrication process of KNN is quite difficult due to volatility and hygroscopicity of sodium [42]. Thus, most researches are focusing on its fabrication. According to this issue, it is believed that KNN material is still far away from being used in practical application.

Regarding another lead-free materials, barium calcium titanate zirconate ((Ba,Ca)(Zr,Ti)O₃; BZCT) compound is one of the attractive materials because it exhibits a promising piezoelectric coefficient (~546 pC/N). This value is higher than several commercial PZTs. Regarding the application for energy harvesting at non-resonant frequency, it is seen that piezoelectric performance of this material is slightly lower (~8.4) than PZT-5H. However, it is believed that BZCT can become a promising candidate for energy harvesting in the future. Rödel et al have confirmed that BZCT material can be a promising candidate for piezoelectric energy harvesting at non-resonant frequency (see Figure 10) [28]. Thus, BZCT material is of interest in this project in order to improve its piezoelectric performance.

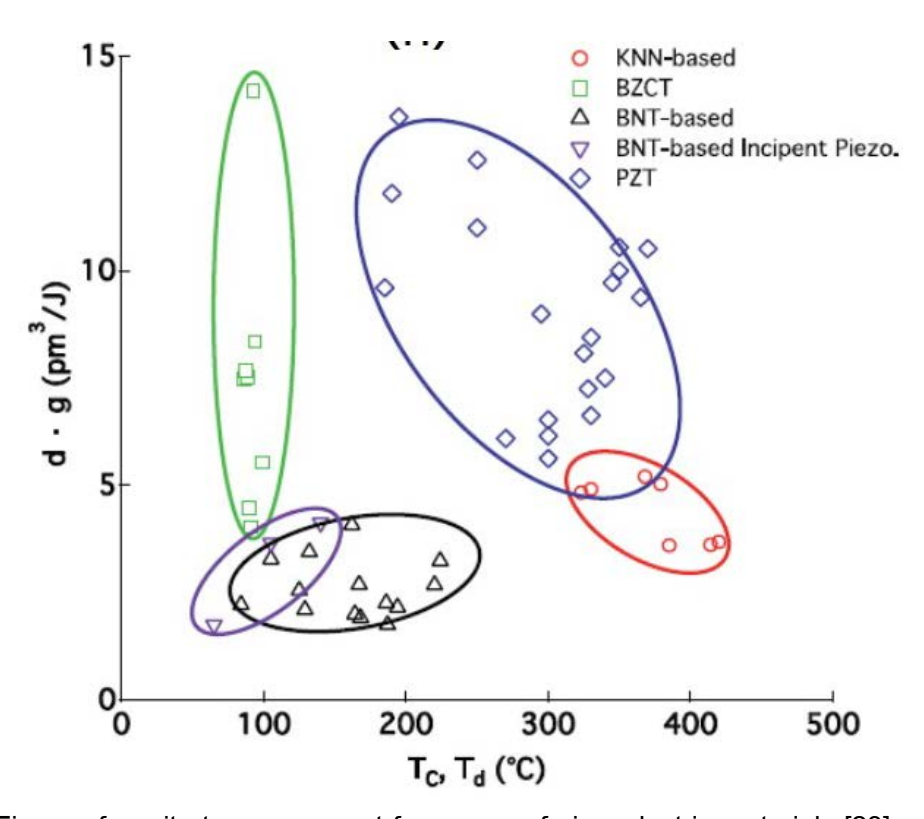


Figure 10. Figure of merit at non-resonant frequency of piezoelectric materials [28].

Table 3. The piezoelectric properties and FOM of PZT and lead-free materials.

materials	d ₃₃ (pC/ N)	g ₃₃ (mV.m/N)	k ₃₃	Q_m	$k^2 \cdot Q_m$	<i>d•g</i> (pm³/J)
PZT-4 [28, 31]	290	25	0.7	>500	-	-
PZT-5A [28, 31]	375	25	0.71	75	-	-
PZT-8 [28, 31]	225	25	0.64	>100 0	583	-
PZT-5H [28, 31]	590	20	0.75	65	23	12
BaTiO ₃ [31]	190	-	0.5	-	-	-
(K,Na,Li)NbO ₃ based [32]	93	-	-	1400	726	-
(K,Na)(Nb,Ta)O ₃ based [33]	-	-	0.41	1400	-	-
(K,Na)NbO ₃ - Bi(Na,K)ZrO ₃ [34]	490	-	-	-	-	-
(Bi,Na)TiO ₃ based [35]	110	-	0.41	500	-	-
(K,Na,Li)NbO ₃ based [36]	295	-	0.46	84	-	-
(K,Na)NbO ₃ based [37]	420	-	0.54	-	-	-
(Ba,Ca)(Zr,Ti)O ₃ [38, 39]	546	15.3	0.65	-	-	8.4
BNT-BKT-ST [40]	-	-	-	-	-	-
BNT-BT-KNN [41]	30	-	-	-	-	-

Among BZCT composition, Lie et al have investigated (Ba_{0.85}Ca_{0.15})(Zr_{0.1}Ti_{0.9})O₃ ceramics (BZT-50BCT) and found that this composition shows a largest piezoelectric coefficient as compared with other piezoelectric materials [39] (see Figure 11). Beside piezoelectric coefficient, this composition also has a large signal piezoelectric coefficient (d^{*}), relating the feature of strain hysteresis loop. This characteristic suggests the application of this material for fuel or inkjet injection [28]. Large piezoelectric response in

this material due to the coexistence of rhombohedral and tetragonal phases (morphotropic phase boundary; MPB) and tri critical point (TCP) (see Figure 12), where the energy barrier of rotating polarization is low. Beside piezoelectric properties, this composition shows large dielectric constant at room temperature (~3000), which makes this material a good candidate for capacitor devices. At room temperature, (Ba_{0.85}Ca_{0.15})(Zr_{0.1}Ti_{0.9})O₃ ceramic is a binary phase with MPB between rhombodedral and tetragonal phase. The phase transition from ferroelectric to paraelectric phase is found below 373 K. Beside piezoelectric and dielectric properties, it is found that the thermoelectric feature of this composition has not been reported. Thus, it is the main interest of this project to investigate piezoelectric properties of (Ba_{0.85}Ca_{0.15})(Zr_{0.1}Ti_{0.9})O₃ composition together with thermoelectric properties for future application in energy harvesting.

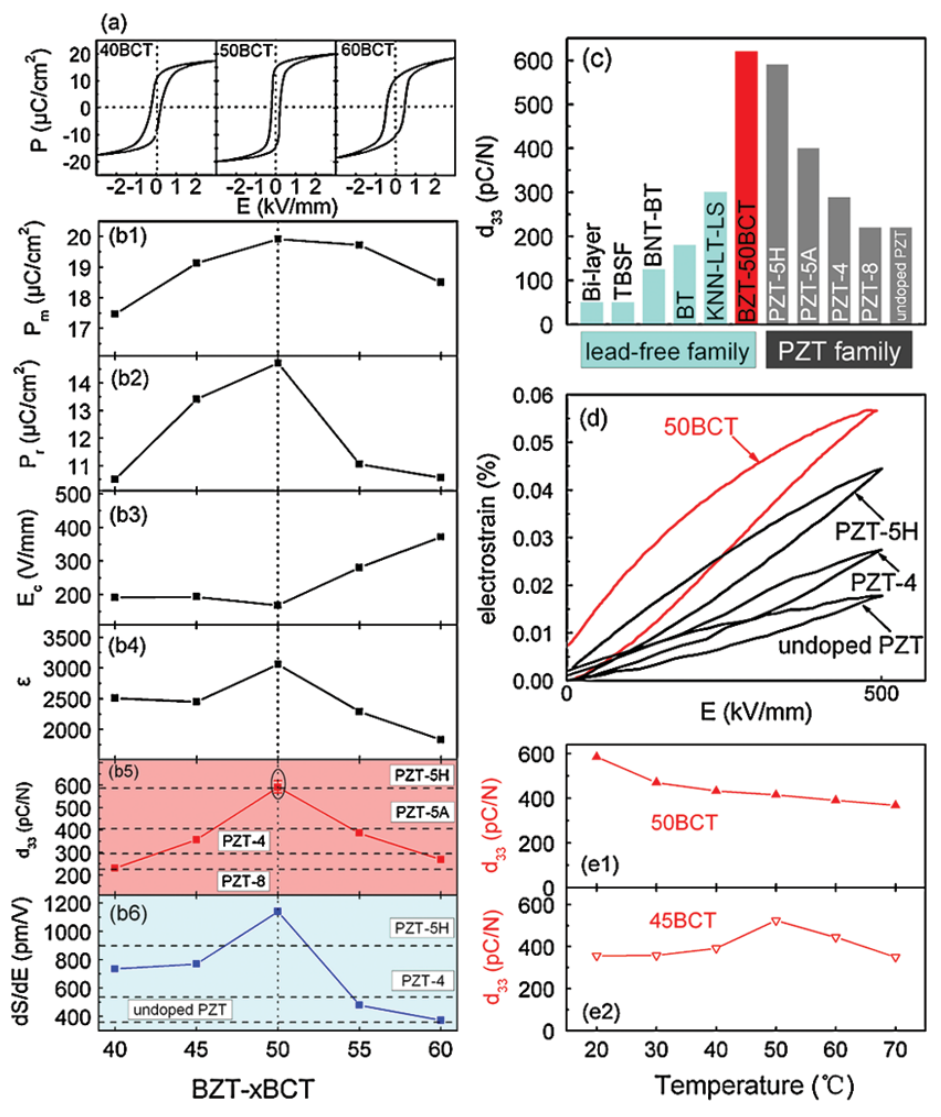


Figure 11. Electrical properties of (Ba_{0.85}Ca_{0.15})(Zr_{0.1}Ti_{0.9})O₃ ceramics [39].

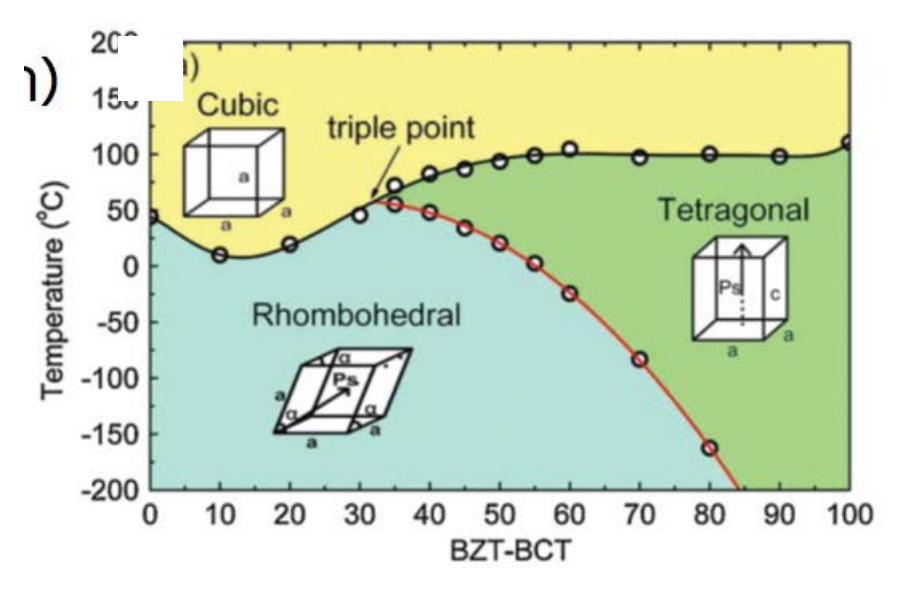


Figure 12. Binary phase diagram of BZT-BCT ceramics [39].

2.3 thermoelectric-piezoelectric material (TPM)

As mentioned in section 5.1 and 5.2, it can be seen that most of researches separately only studied either thermoelectric or piezoelectric materials. However, it is found that the attention of composite system between both materials is mentioned scarcely. Thus, combination of thermoelectric and piezoelectric materials has attracted the attention of this project in order to develop a hybrid oxide material for application in thermal and vibrational energy harvesting. Muta et al [43] have studied thermoelectric properties of binary ceramics between piezoelectric BaTiO₃ and thermoelectric SrTiO₃. Upon increasing BaTiO₃ content, they found that Seebeck coefficient and thermal conductivity of SrTiO₃ was enhanced. The maximum figure of merit was found at about 400 K with the composition Ba_{0.3}Sr_{0.6}La_{0.1}TiO₃ as shown in Figure 13. Unfortunately, the piezoelectric properties was not investigated in their work. In addition, the interface between BaTiO₃ and SrTiO₃ can give excellent piezoelectric response, as suggested by Hu et al [44]. This indicates that solid solution of BaTiO₃-SrTiO₃ is a good example of thermoelectric-piezoelectric material.

From the section 5.1 and 5.2, it can be seen that $Ca_3Co_4O_9$ (CCO), $CaMnO_3$ (CMO) and ZnO (ZO) compound are attractive thermoelectric oxides while $Ba_{0.85}Ca_{0.15}Zr_{0.1}Ti_{0.9}O_3$ (BCZT) compound is an attractive piezoelectric oxide. Since the hybrid systems of $Ca_3Co_4O_9$ - $Ba_{0.85}Ca_{0.15}Zr_{0.1}Ti_{0.9}O_3$ (CCO-BCZT), $CaMnO_3$ - $Ba_{0.85}Ca_{0.15}Zr_{0.1}Ti_{0.9}O_3$ (CMO-BCZT) and ZnO- $Ba_{0.85}Ca_{0.15}Zr_{0.1}Ti_{0.9}O_3$ (ZO-BCZT) have not been studied, this has become our motivation to fabricate and study thermoelectric and piezoelectric properties of these binary systems.

Regarding thermoelectric-piezoelectric materials in this project, it is expected that addition of thermoelectric materials can enhance piezoelectric performance (Eqn. 3 and 4) of BCZT. In case of ZO-BCZT system, it is assumed that Zn^{2+} ions may substitute Ti^{4+} ions due to ionic radius similarity, resulting in a lattice distortion and creation of structural defects. This may promote better piezoelectric performance. Lee et all have used ZnO addition for enhancement of K_p and Q_m (see in Fig. 14) of $Bi_{0.5}Na_{0.5}TiO_3$ piezoelectric ceramics [45]. Beside structural effect, Tsai et all found that ZnO doping increased the average grain size, resulting in an enhancement of piezoelectric properties of PZT-PMN based ceramics [46]. Similarly, the effects of lattice distortion or microstructural feature can be a significant factor for improvement of piezoelectric properties of CCO-BCZT and CMO-BCZT hybrid systems. Until now, the addition of CCO or CMO in piezoelectric material has not been studied. Thus, these hypotheses need to be demonstrated with actual experiments.

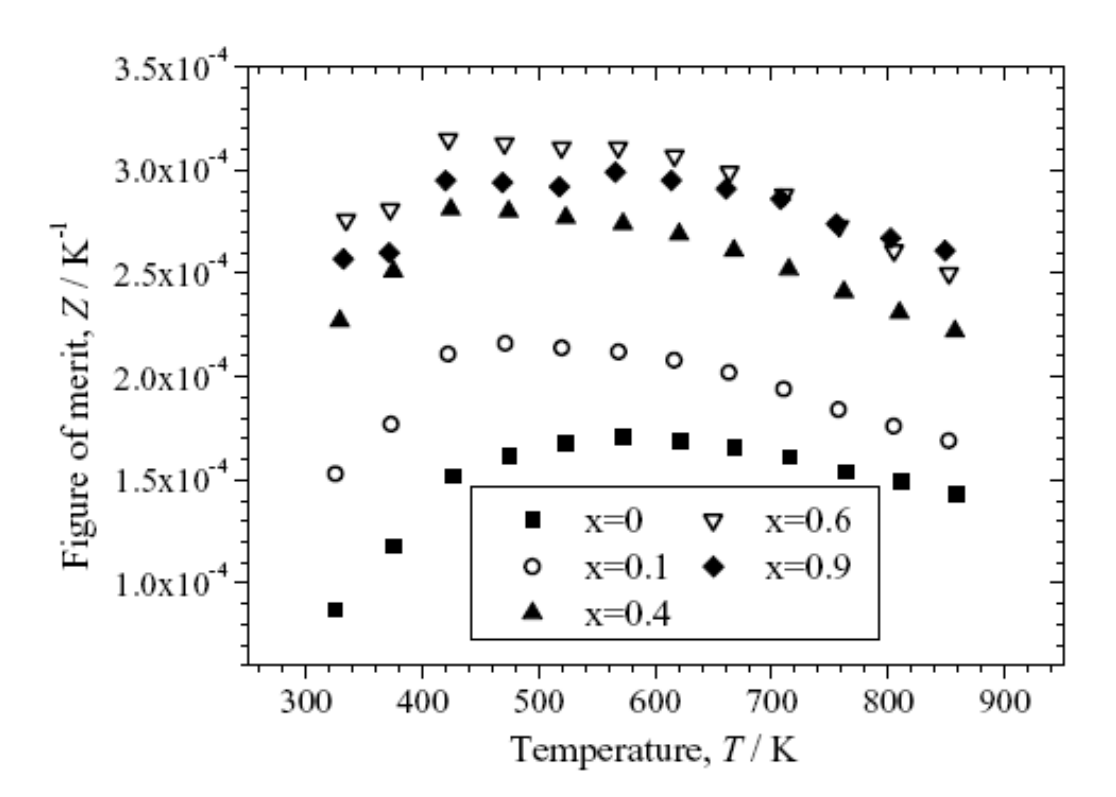


Figure 13. Figure of merit of Ba_{1-x}Sr_xLa_{0.1}TiO₃ ceramics [43].

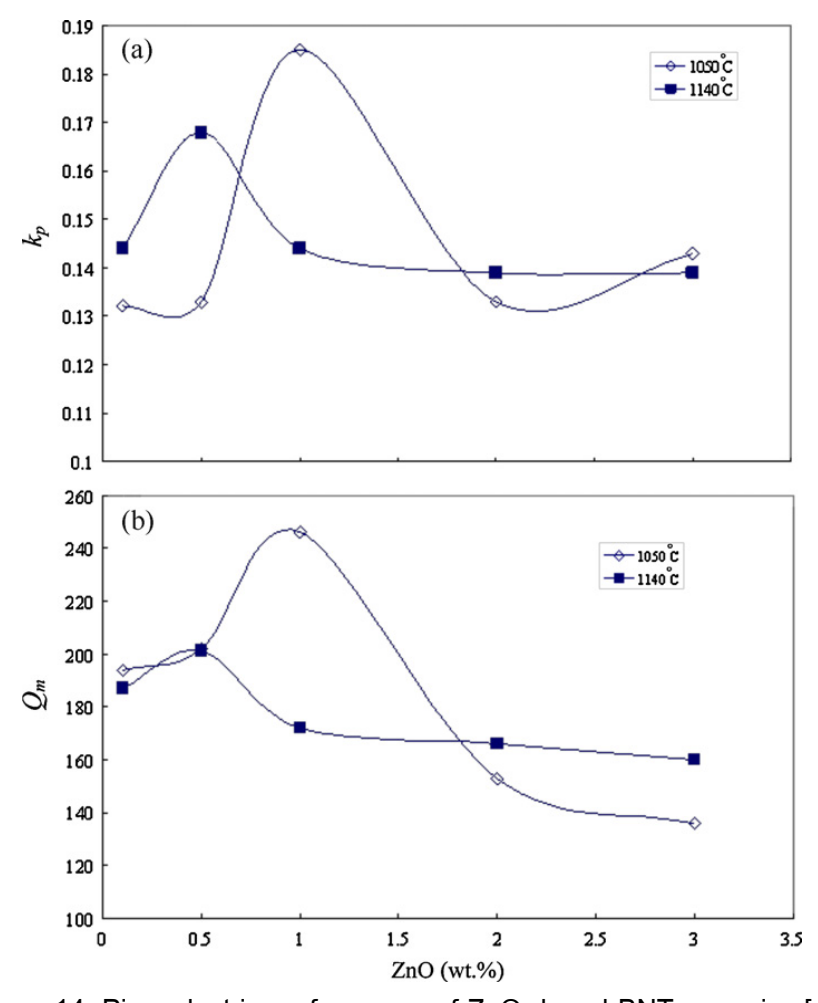


Figure 14. Piezoelectric performance of ZnO-doped BNT ceramics [45].

Beside the expected piezoelectric enhancement by ZO, CCO and CMO thermoelectric materials in this project, it is also believed that the existence of piezoelectric BCZT can enhance thermoelectric performance (Eqn. 1) of the hybrid systems. Chaouchi et al have measured electrical conductivity of BCZT at high temperature and found that the value increased from $\sim 10^{-7}$ (Ω cm) $^{-1}$ at temperature of 400 K to ~ 2 (Ω cm) $^{-1}$ at 800 K as shown in Figure 15 [47]. This indicates a dramatic increase of σ with increasing temperature. It is expected that this temperature dependence of electrical conductivity may enhance ZT of thermoelectric-piezoelectric binary ceramics. The investigation relating to electrical conduction of BCZT is quite limited. Also, Seebeck coefficient and thermal conductivity of BCZT ceramic have not been studied. Hence, the acquired knowledge based on BCZT's hybrid systems may be useful for development of novel compounds suitable for additional energy-related application. Although thermal conductivity of BCZT has not been reported, the thermal conduction feature of this material attributed mainly to phonon scattering (similarly to that in BaTiO₃ as suggested by Aggarwal et al [48]) is expected to improve

thermoelectric performance of CCO, CMO and ZO ceramics. These hypotheses will also need further verification by carrying out real experiments.

In this project, it is expected that finding the most suitable fabrication procedure and chemical composition, and simultaneous investigation of thermoelectric and piezoelectric performance of hybrid ceramics including CCO-BCZT, CMO-BCZT and ZO-BCZT can give novel insights for these novel thermoelectric-piezoelectric materials. The results are expected to be highly beneficial for the development of new oxide material for application in both waste-heat and vibrational energy harvesting.

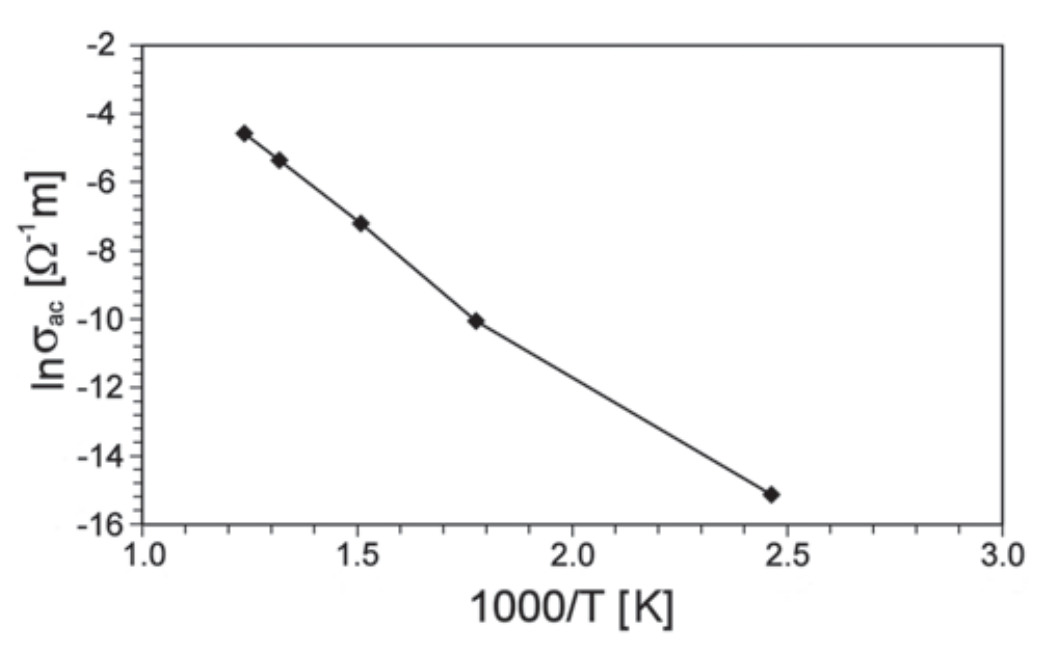


Figure 15. Electrical conductivity of BCZT ceramics [47].

References

- [1] S. Lee, J.A. Bock, S.T.M. Kinstry and C.A. Randall, Ferroelectric-thermoelectricity and Mott transition of ferroelectric oxides with high electronic conductivity, J. Eur. Ceram. Soc., 32, (2012) 3971-3988.
- [2] T.M. Tritt, ed., "Recent Trends in Thermoelectric Materials Research," Semiconductors and Semimetals, Vols. 69-71, treatise editors, R.K. Willardson and E. Weber, Academic Press, New York (2000).
- [3] A.F. loffe, semiconductor Thermoelements and Thermoelectric Cooling, Infosearch, London (1957).
- [4] G.S. Nolas, J.W. Sharp and H.J. Goldsmid, Thermoelectrics: Basic Principles and New Materials Developments, Springer-Verlag, 2001.
- [5] H.J. Goldsmid, Electronic Refrigeration, Pion Limited, London (1986).

- [6] T.M. Tritt and M.A. Subramanian, Thermoelectric materials, phenomena, and applications: a bird's eye view, MRS Bulletin, 31, 3 (2006) 188-194.
- [7] J. He, Y. Liu and R. Funahashi, Oxide thermoelectrics: The challenges, progress and outlook, J. Mater. Res., 26, (2011) 1762-1772.
- [8] L.T. Hung, N.V. Nong, S. Linderoth and N. Pryds, Segmentation of low-cost high efficiency oxide-based thermoelectric materials, Phys. Status. Solidi. A, 212, (2015) 767-774.
- [9] K. Koumoto, R. Funahashi, E. Guilmeau, Y. Miyazaki, A. Weidenkaff, Y. Wang and C. Wan, Thermoelectric ceramics for energy harvesting, J. Am. Ceram. Soc., 96 [1] (2013) 1-23.
- [10] J.W. Fergus, Oxide materials for high temperature thermoelectric energy convesion, J. Eur. Ceram. Soc. 32 (2012) 525–540
- [11] S.R. Brown, S.M. Kauzlarich, F. Gascoin, G.J. Snyder, Yb14MnSb11: new high efficiency thermoelectric material for power generation, Chem. Mater. 18 (2006) 1873–7.
- [12] C.B. Vining, W. Laskow, J.O. Hanson, R.R. Van der Beck, P.D. Gorsuch, Thermoelectric properties of pressure-sintered silicon-germanium (Si0.8Ge0.2) thermoelectric alloys. J. Appl. Phys., 69 (1991) 4333–40.
- [13] T. Seetawan, V. Amornkitbamrung, T. Burinprakhon, S. Maensiri, K. Kurosaki, H. Muta, et al. Thermoelectric power and electrical resistivity of Ag doped Na1.5Co2O4. J. Alloys. Compd. 407 (2006) 314–7.
- [14] S. Hebert, D. Flahaut, C. Martin, S. Lemonnier, J. Noudem, C. Goupil, et al. Thermoelectric properties of perovskites: sign change of the Seebeck coefficient and high temperature properties, Prog. Solid. State. Chem. 35 (2007) 457–67.
- [15] Y. Liu, Y. Lin, L. Jiang, C.W Nan, Z. Shen, Thermoelectric properties of Bi³⁺ substituted Co-based misfit-layered oxides. J. Electroceram. 21 (2008) 748–51.
- [16] Y. Wang, Y. Sui, J. Cheng, X. Wang, W. Su, Comparison of the high temperature thermoelectric properties for Ag-doped and Ag-added Ca₂Co₄O₉, J. Alloys. Comp., 477 (2009) 817-821.
- [17] W. Koshibae and S. Maekawa, Effect of Spin and Orbital on Thermopower in Strongly Correlated Electron Systems, J. Mag. Mag. Mater., 216–18 (2003) 258– 259.
- [18] M. Karppinen, H. Fjellvag, T. Konno, Y. Morita, T. Motohashi and H. Yamauchi, Evidence for oxygen vacancies in misfit-layered calcium cobalt oxide [CoCa2O3]qCoO2, Chem. Mater. 16 (2004) 2790-2793.

- [19] S. Jantrasee, S. Pinitsoontorn and P. Moontragoon, First-principles study of the electronic structure and thermoelectric properties of Al-doped ZnO, J. Electro. Mater., 43 (2014) 6.
- [20] G.D. Mahan, Good thermoelectrics, Solid. State. Phys., 51 (1997) 81–157.
- [21] H. Muta, K. Kurosaki, S. Yamanaka. Thermoelectric properties of rare earth doped SrTiO₃, J. Alloys. Compd. 350 (2003) 292–5.
- [22] M. Ohtaki, T. Tsubota, K. Eguchi, H. Arai, High-temperature thermoelectric properties of (Zn1¬xAlx)O, J. Appl. Phys. 79 (1996) 1816–8.
- [23] Y. Kinemuchi, M. Mikami, K. Kobayashi, K. Watari, Y. Hotta, Thermoelectric properties of nanograined ZnO, J. Electron. Mater. 39 (2010) 2059–63.
- [24] Z.L. Wang and Z.C. Kang, Functional, and Smart Materials, Plenum Press, New York, 1998.
- [25] Y. Wang, Y. Sui, X. Wang, W. Su. Enhancement of thermoelectric efficiency in (Ca,Dy)MnO₃-(Ca,Yb)MnO₃ solid solutions. Appl. Phys. Lett., 97 (2010) 052109-1–3.
- [26] G. Xu, R. Funahashi, Q. Pu, B. Liu, R. Tao G. Wang, et al. High-temperature transport properties of Nb and Ta substituted CaMnO₃ system. Solid. State. lonics., 172 (2004) 147–51.
- [27] R. Funahashi, S. Urata, T. Mihara, N. Nabeshima, and K. Iwasaki, Power Generation Using Oxide Thermoelectric Modules, Industrial Ceram., 28, (2008) 227–33.
- [28] J. Rödel, K.G. Webber, R. Dittmer, W. Jo, M. Kimura, et al., Transferring lead-free piezoelectric ceramics into application, *J. Eur. Ceram. Soc.*, 35 (2015) 1659-1681.
- [29] E. Defay, Integration of ferroelectric and piezoelectric thin films: Concepts and application for microsystems, John Wiley & Sons, Inc, Hoboken USA, 2011.
- [30] D. Shen, J.H. Park, J.H. Noh, S.Y. Choe, S.H. Kim, H.C. Wikle and D.J. Kim, Micromachined PZT cantilever based on SOI structure for low frequency vibration energy harvesting, Sensors and Actuators A: Physical, 154, (2009) 103-108.
- [31] T.R. Shrout and S.J. Zhang, Lead-free piezoelectric ceramics: Alternatives for PZT, *J. Electroceram.*, 19 (2007) 111-124
- [32] E. Li, H. Kakemoto, T. Hoshina and T. Tsurumi, Shear-mode ultrasonic motor using potassium sodium niobate-based ceramics with high mechanical quality factor, *Jpn. J. Appl. Phys.*, 47 (2008) 7702-6.

- [33] M. Matsubara, T. Yamaguchi, W. Sakamoto, K. Kikuta, T. Yogo and S. Hirano, Processing and piezoelectric properties of lead-free (K,Na)(Na,Ta)O₃ ceramics, *J. Am. Ceram. Soc.*, 88 (2005) 1190-6.
- [34] X. Wang, J. Wu, D. Xiao, X. Cheng, T. Zheng, et al., Giant piezoelectricity in potassium-sodium niobate lead-free ceramics. *J. Am. Chem. Soc.*, 136 (2014) 2905-10.
- [35] T. Tou, Y. Hamaguti, Y. Maida, H. Yamamori, K. Takahashi and Y. Terashima, Properties of (Bi_{0.5}Na_{0.5})TiO₃-BaTiO₃-(Bi_{0.5}Na_{0.5})(Mn_{1/3}Nb_{2/3})O₃ lead-free piezoelectric ceramics and its application to ultrasonic cleaner, *Jpn. J. Appl. Phys.* 48 (2009) 07GM3.
- [36] D. Tanaka, T. Tsukada, M. Furukawa, S. Wada and Y. Kuroiwa, Thermal reliability of alkaline niobate-based lead-free piezoelectric ceramics, *Jpn. J. Appl. Phys.* 48 (2009) 09KD08.
- [37] R. Wang, H. Bando, M. Itoh, DO-033.0 Xi'am. China: IMF-ISAF; 2009.
- [38] D. Xue, Y. Zhou, H. Bao, C. Zhou, J. Gao, X. Ren, Elastic, piezoelectric, and dielectric properties of Ba(Zr_{0.2}Ti_{0.8})O₃-50(Ba_{0.7}Ca_{0.3})TiO₃ Pb-free ceramic at the morphotopic phase boundary, *J. Appl. Phys.* 109 (2011) 054110.
- [39] W.F. Liu and X.B. Ren, Large piezoelectric effect in Pb-free ceramics, *Phys. Rev. Lett.* 103 (2009) 257602.
- [40] K. Wang, A. Hussain, W. Jo and J. Rödel, Temperature-dependent properties of (Bi_{1/2}Na_{1/2})TiO₃-(Bi_{1/2}K_{1/2})TiO₃-SrTiO₃ lead-free piezoceramic. J. Am. Ceram. Soc. 95 (2012) 2241-7.
- [41] S.T. Zhang, A.B. Kounga, E. Aulbach, T. Granzow, W. Jo, H.J. Kleebe, et al., Lead-free piezoelectrics with giant strain in the system Bi_{0.5}Na_{0.5}TiO₃-BaTiO₃-K_{0.5}Na_{0.5}NbO₃, I. Structure and room temperature properties, J. Appl. Phys. 103 (2008) 034107.
- [42] P.K. Panda and B. Sahoo, PZT to lead free piezo ceramics: A review, Ferroelectrics, 474 (2015) 128-143.
- [43] H. Muta, K. Kurosaki and S. Yamanaka, Thermoelectric properties of doped BaTiO₃-SrTiO₃ solid solution, J. Alloys Compd., 368 (2004) 22-24.

- [44] D. Hu, H. Ma, Y. Tanaka, L. Zhao and Q. Feng, Ferroelectric mesocrystalline BaTiO₃/SrTiO₃ nanocomposites with enhanced dielectric and piezoelectric responses, Chem. Mater., 27 (2015) 4983-4994.
- [45] Y.C. Lee, T.K. Lee and J.H. Jan, Piezoelectric properties and microstructures of ZnO-doped Bi_{0.5}Na_{0.5}TiO₃ ceramics, J. Eur. Ceram. Soc., 31 (2011) 3145-3152.
- [46] C.C. Tsai, C.S. Hong, C.C. Shih and S.Y. Chu, Electrical properties and temperature behavior of ZnO-doped PZT-PMnN modified piezoelectric ceramics and their applications on therapeutic transducers, J. Alloys Compd., 511 (2012) 54-62.
- [47] A. Chaouchi and S. Kennour, Impedance spectroscopy studies on lead free (Ba_{0.85}Ca_{0.15})(Ti_{0.9}Zr_{0.1})O₃ ceramics, Processing. Appli. Ceram. 6[4] (2012) 201-207.
- [48] G.K. Aggarwal, A. Kumar and U.C. Naithani, Field dependent thermal conductivity of SrTiO₃, BaTiO₃ and KTaO₃ ferroelectric perovskites, International J. Eng. Res. Develop. 4 (2012) 61-67.

3. Objectives

- 3.1 To fabricate a hybrid oxides between thermoelectric and piezoelectric materials including CCO-BCZT, CMNO-BCZT and ZAO-BCZT systems and to investigate the influences of a crystal structure, microstructure and local structure on thermoelectric and piezoelectric properties of these hybrid oxides.
- 3.2 To seek new materials which exhibits simultaneously a thermoelectricity and piezoelectricity. These materials are expected to be alternative materials for an additional energy harvesting from waste-heat and vibrational source.

4. Research methodology

- 1. Powder preparation of CCO, CMNO, ZAO and BCZT compounds. The chemical compounds in this project are composed of $Ca_3Co_4O_9$ (CCO), CaMnNbO $_3$ (CMNO), ZnAIO (ZAO) and $Ba_{0.85}Ca_{0.15}Zr_{0.1}Ti_{0.9}O_3$ (BCZT). The starting powders of each compound will be weighed following its stoichiometry and mixed a mixed oxide method. After that, the dried powders will be calcined in an alumina crucible at calcination temperature of 800 to 1,200 °C in air atmosphere with heating/cooling rate of 5 °C/min. The compositions in this project are composed of (1-x)CCO-(x)BCZT, (1-x)CMNO-(x)BCZT and (1-x)ZAO-(x)BCZT where x=0, 0.1, 0.2, 0.3, 0.4, 0.5, 0.6, 0.7, 0.8, 0.9 and 1 weight fraction. After obtaining CCO, CMNO, ZAO and BCZT powders, the compound will be weighed following its composition and mixed again using mixed oxide method for 6 hrs.
- 2. Ceramic fabrication of CCO-BCZT, CMNO-BCZT and ZAO-BCZT hybrid systems. The powders will be pressed using uniaxial technique as a green body (pellet). To fabricate (1-x)CCO-(x)BCZT, (1-x)CMNO-(x)BCZT and (1-x)ZAO-(x)BCZT ceramics, the pellets will be sintered by a solid state sintering technique in alumina plate at sintering temperature of 1100 to 1,400 °C in air atmosphere with heating/cooling rate of 5 °C/min.
- 3. Characterization of CCO-BCZT, CMNO-BCZT and ZAO-BCZT ceramics. The focus on physical properties in this project are shrinkage, weight loss and bulk density of all ceramics. X-ray diffraction technique (XRD) will be used to study crystal structure and phase characteristic of all ceramics. Scanning electron microscopy (SEM) will be used to observe microstructure (grain size, grain morphology and grain size distribution) of dense ceramics. Beside microstructural feature, Energy-dispersive X-ray spectroscopy (EDX) will be used to explore a chemical composition of all ceramics. The local structure will be studied by Synchrotron X-ray Absorption Spectroscopy (XAS) measurements of the Siam Photon Laboratory, Synchrotron Light Research Institute (SLRI), with electron energy of 1.2 GeV. With transmission mode, the powder will be pressed within mold of instrument. For fluorescence mode, the ceramic surface will be cleaned in acetone by ultrasonic vibration and then will be dried at 120 °C for 24 hrs.

- 4. Thermoelectric measurement of all ceramics. The thermoelectric performance is composed of electrical conductivity (σ), Seebeck coefficient (S) and thermal conductivity (k). Electrical conductivity, Seebeck coefficient and thermal conductivity will be measured simultaneously in the temperature range from 25 °C to 700 °C (~300 to 1000 K). Sample preparation for thermoelectric measurement.
- 5. Piezoelectric measurement of all ceramics. This project would focus on piezoelectric coefficient (d_{33}) , piezoelectric voltage coefficient (g_{33}) and electromechanical coupling factor (k). Sample preparation for piezoelectric measurement.

Result

Figure 1 Images of BCZT-CCO powder



Figure 2 BCZT-CCO ceramics

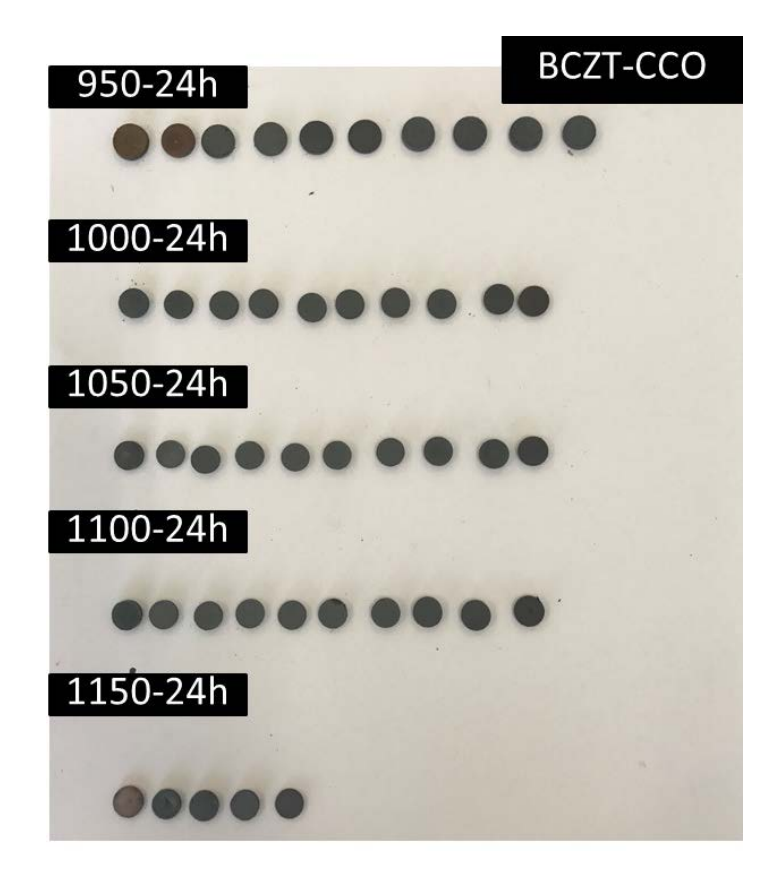


Figure 3 Bulk density of BCZT-CCO ceramics

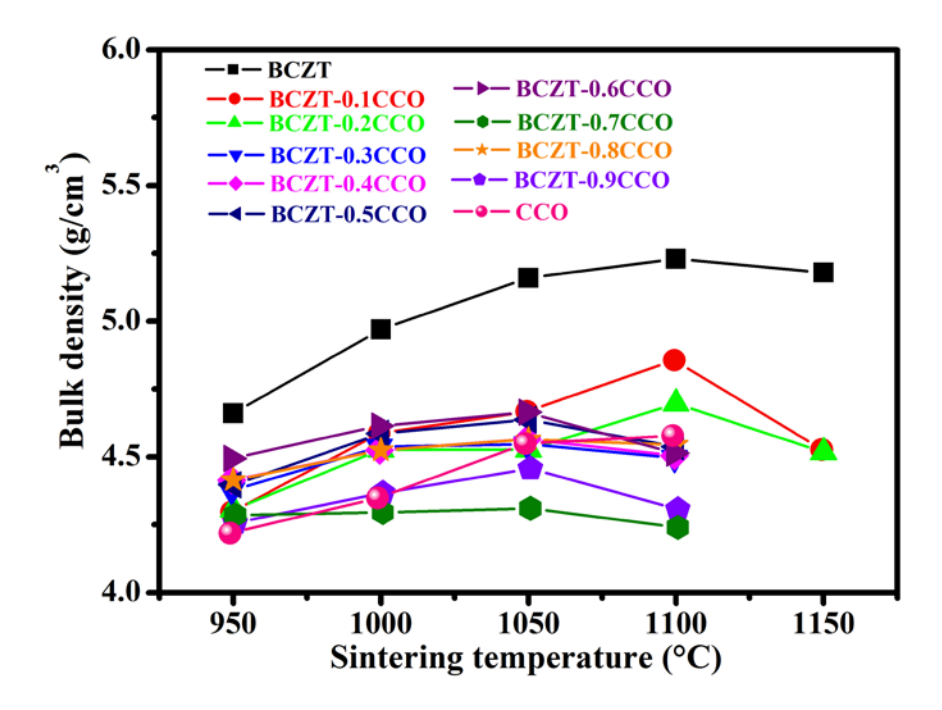


Figure 4 XRD patterns of BCZT-CCO ceramics

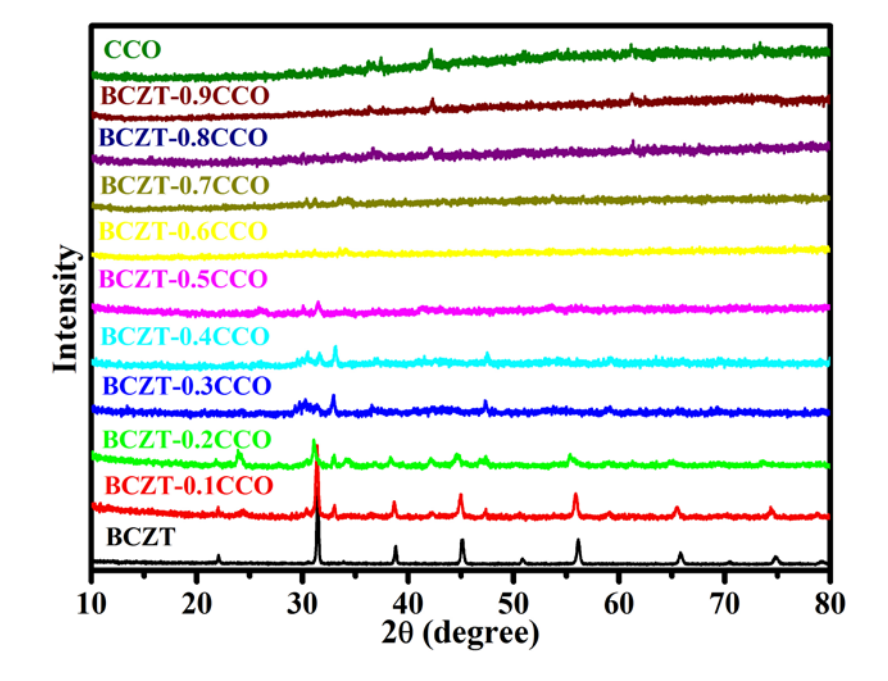


Figure 5 Microstructure of BCZT-CCO ceramics

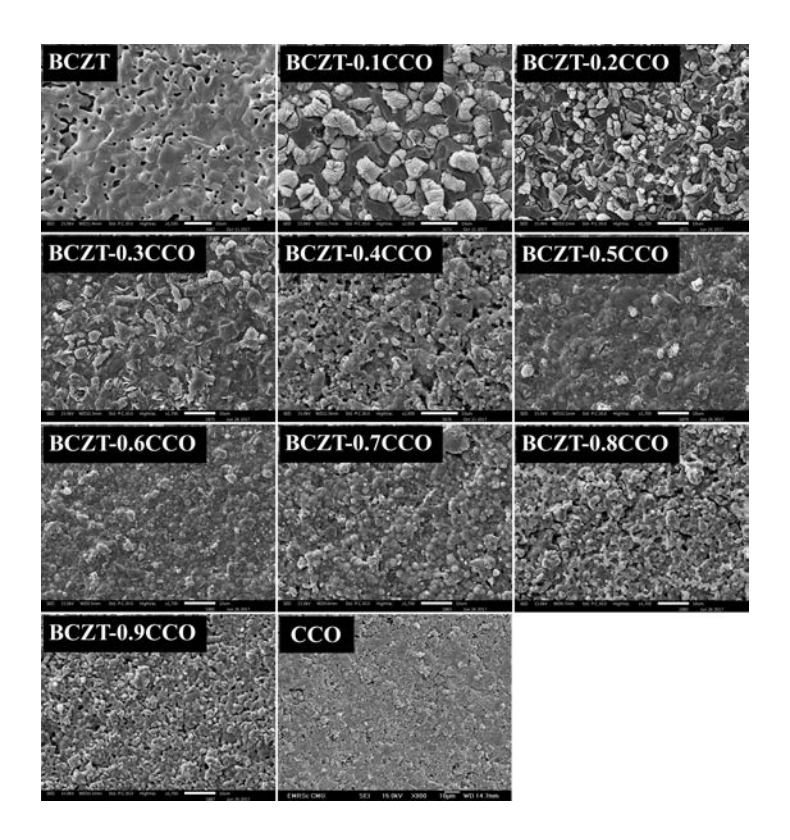


Figure 6 Images of BCZT-CMNO powder



Figure 7 BCZT-CMNO ceramics

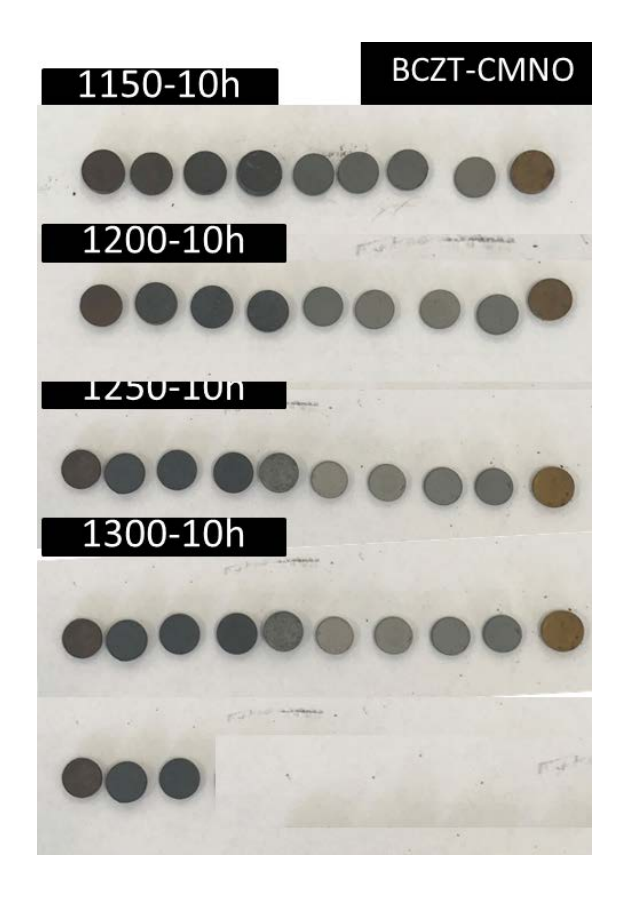


Figure 8 Bulk density of BCZT-CMNO ceramics

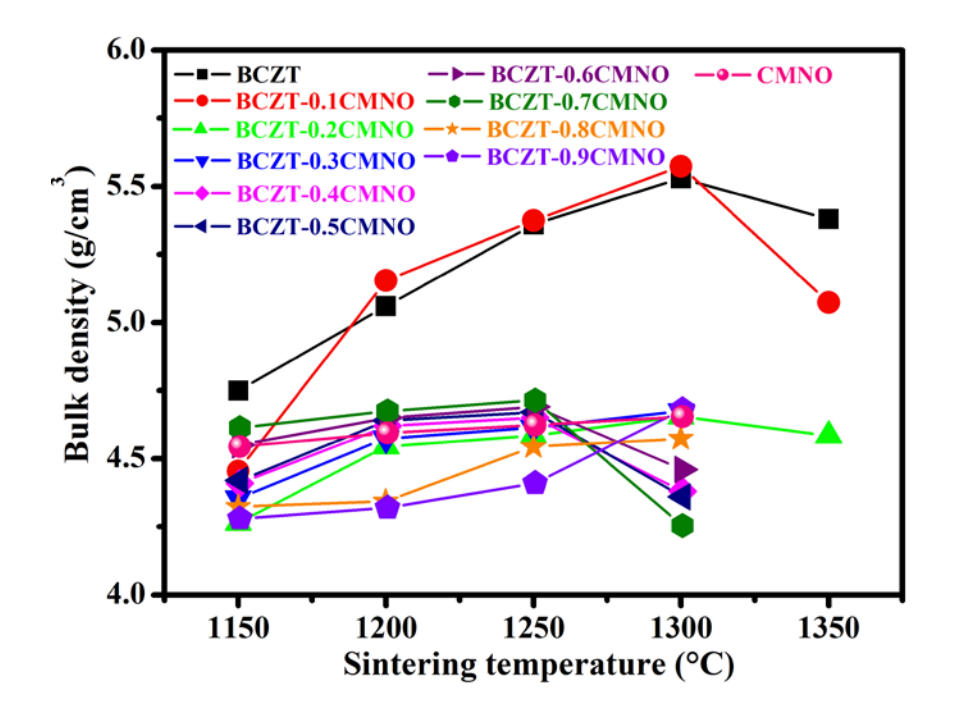


Figure 9 XRD patterns of BCZT-CMNO ceramics

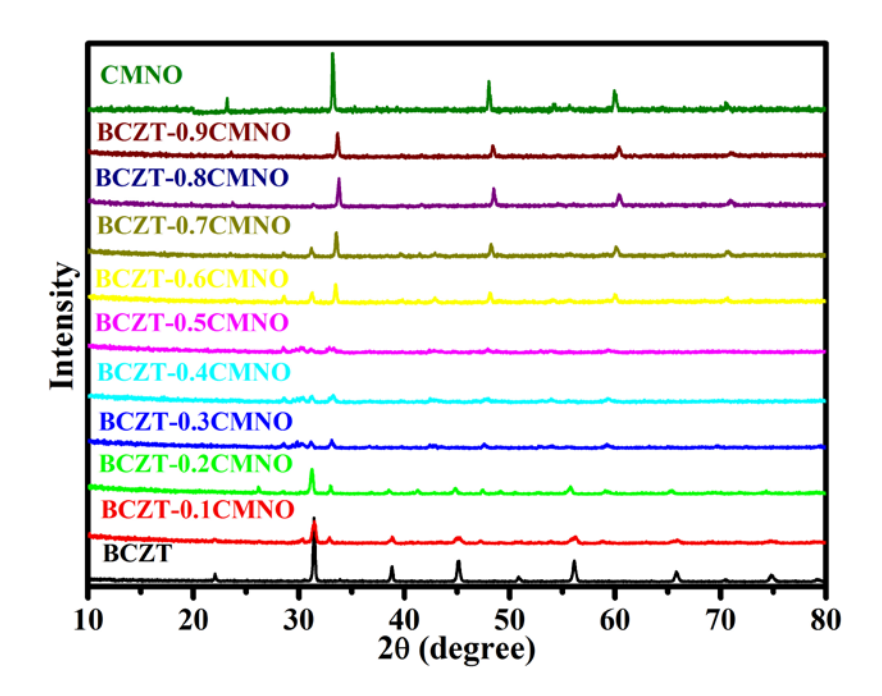


Figure 10 Microstructure of BCZT-CCO ceramics

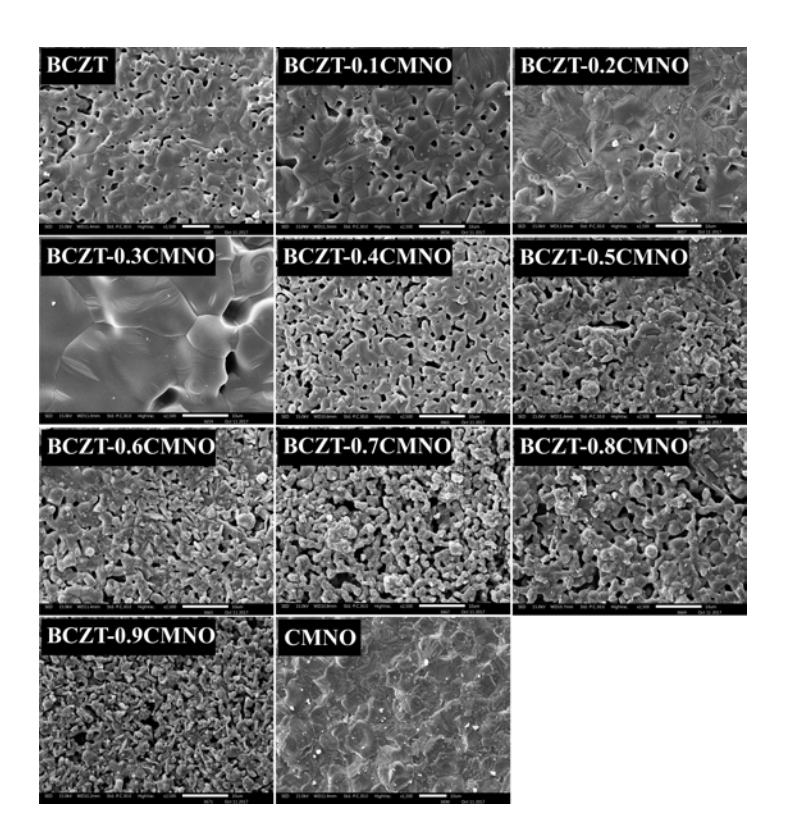


Figure 11 Images of BCZT-ZAO powder



Figure 12 BCZT-ZAO ceramics

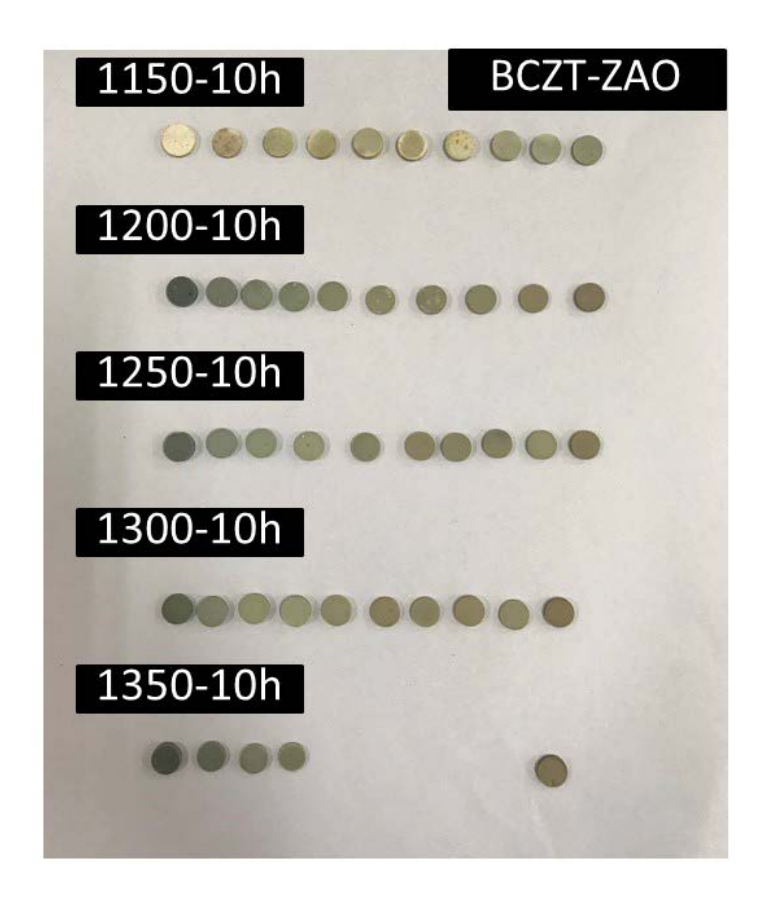


Figure 13 Bulk density of BCZT-ZAO ceramics

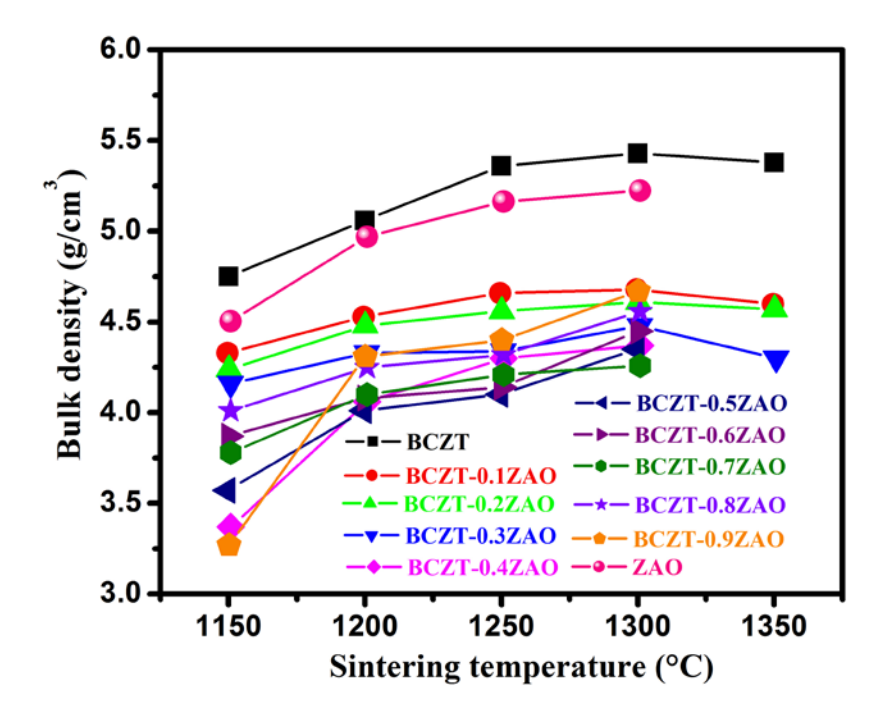


Figure 14 XRD patterns of BCZT-ZAO ceramics

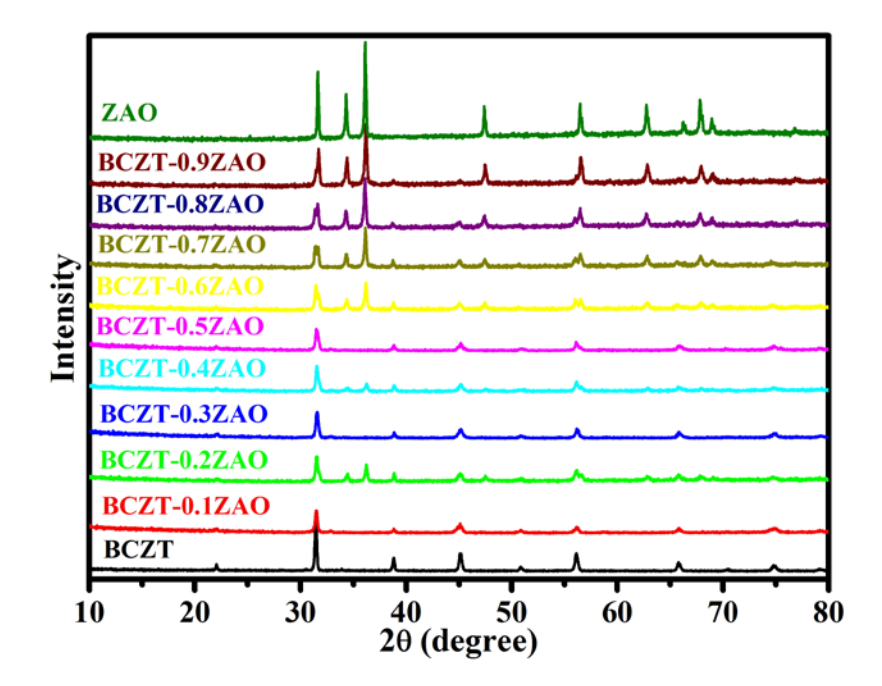


Figure 15 Microstructure of BCZT-ZAO ceramics

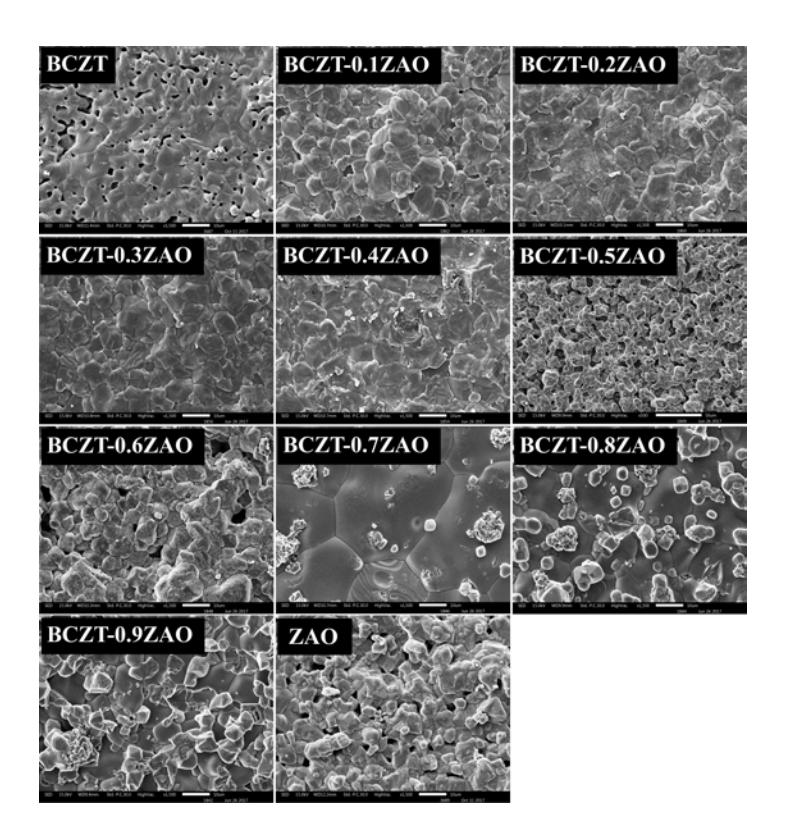


Figure 16 Electrical conductivity of BCZT-CCO ceramics

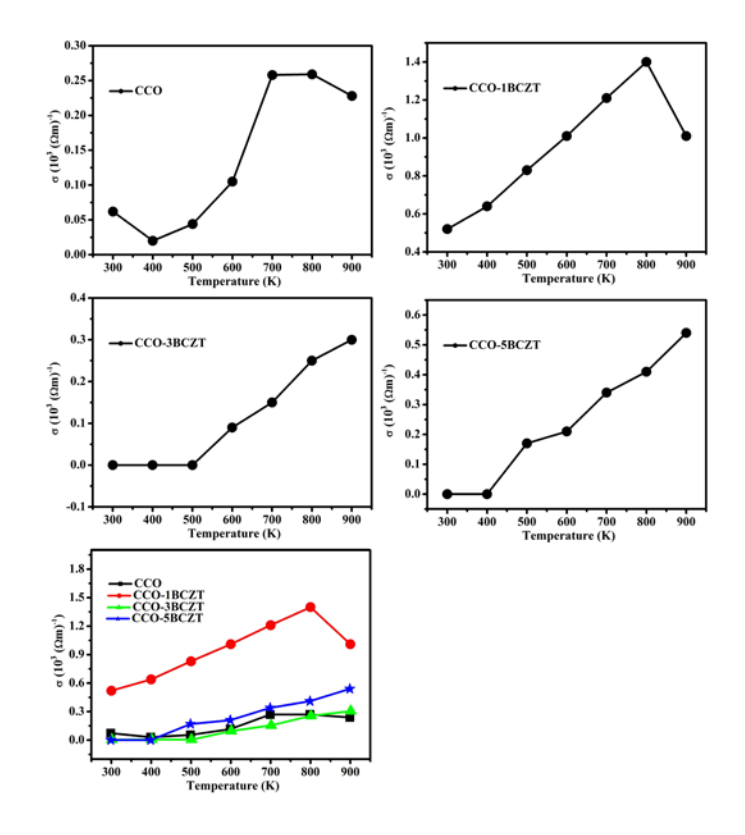


Figure 17 Seebeck coefficient of BCZT-CCO ceramics

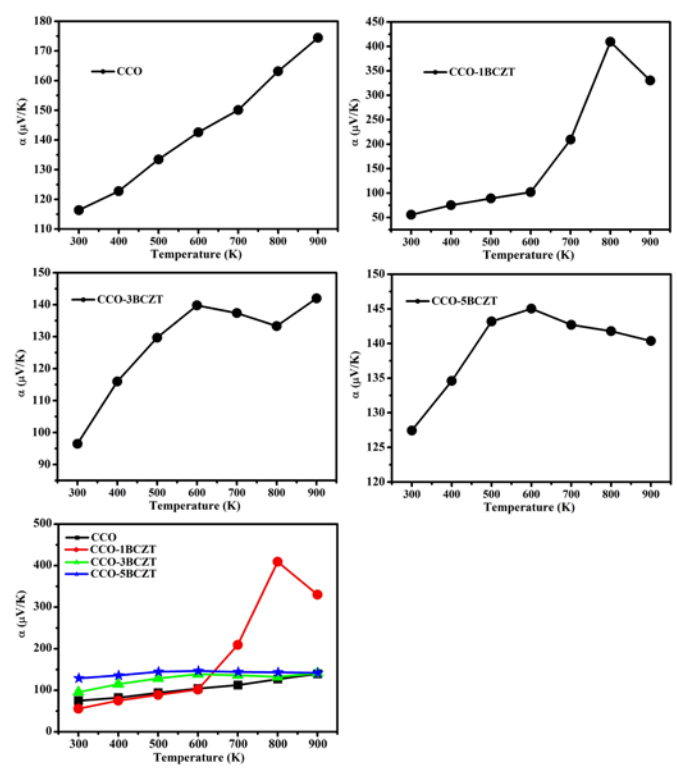


Figure 18 Thermal conductivity of BCZT-CCO ceramics

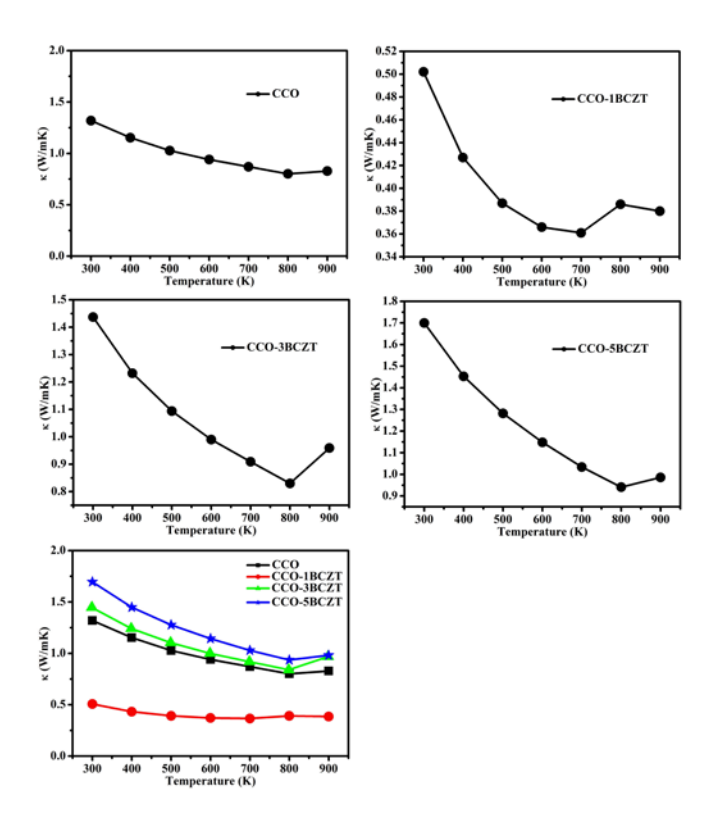


Figure 19 Dielectric properties of the selected ceramics

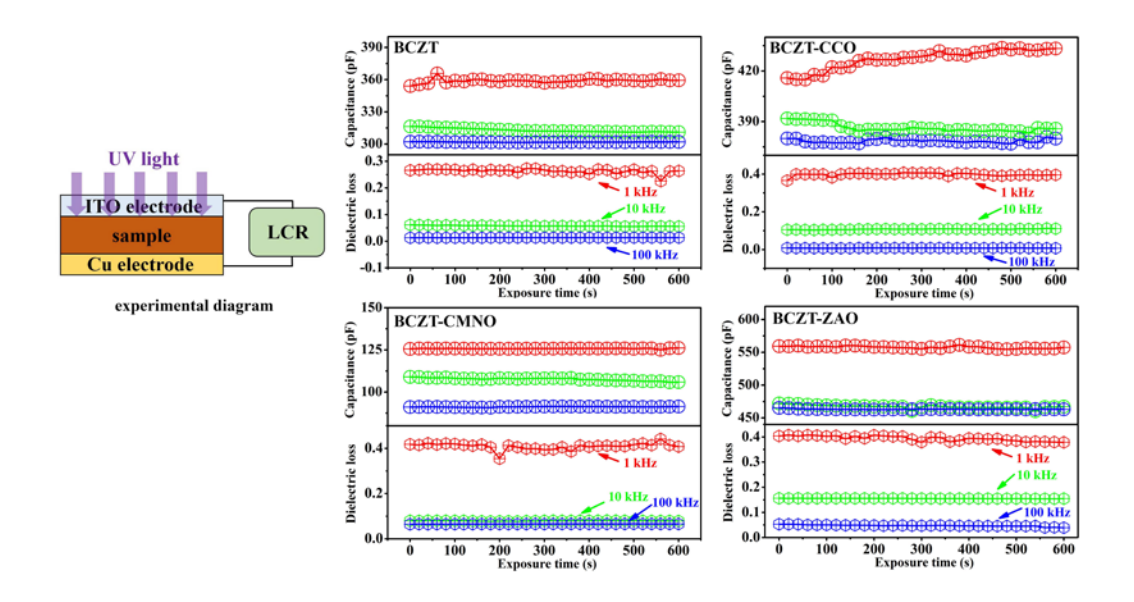


Figure 20 XRD, XPS, and microstructure of the selected ceramics

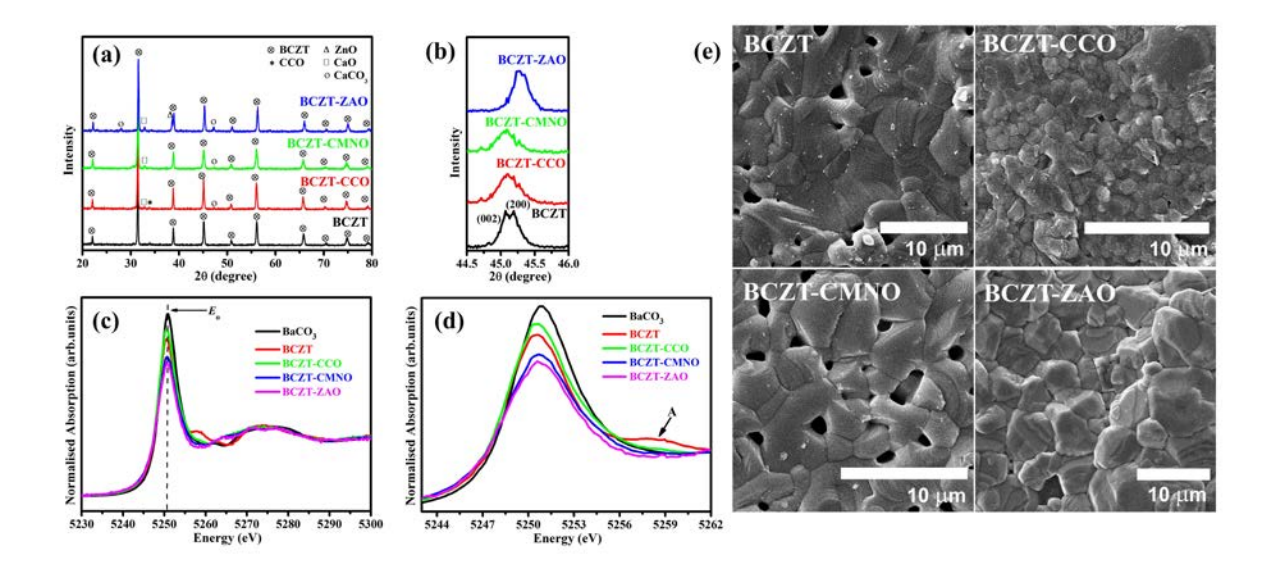


Figure 21 Dielectric properties of the selected ceramics

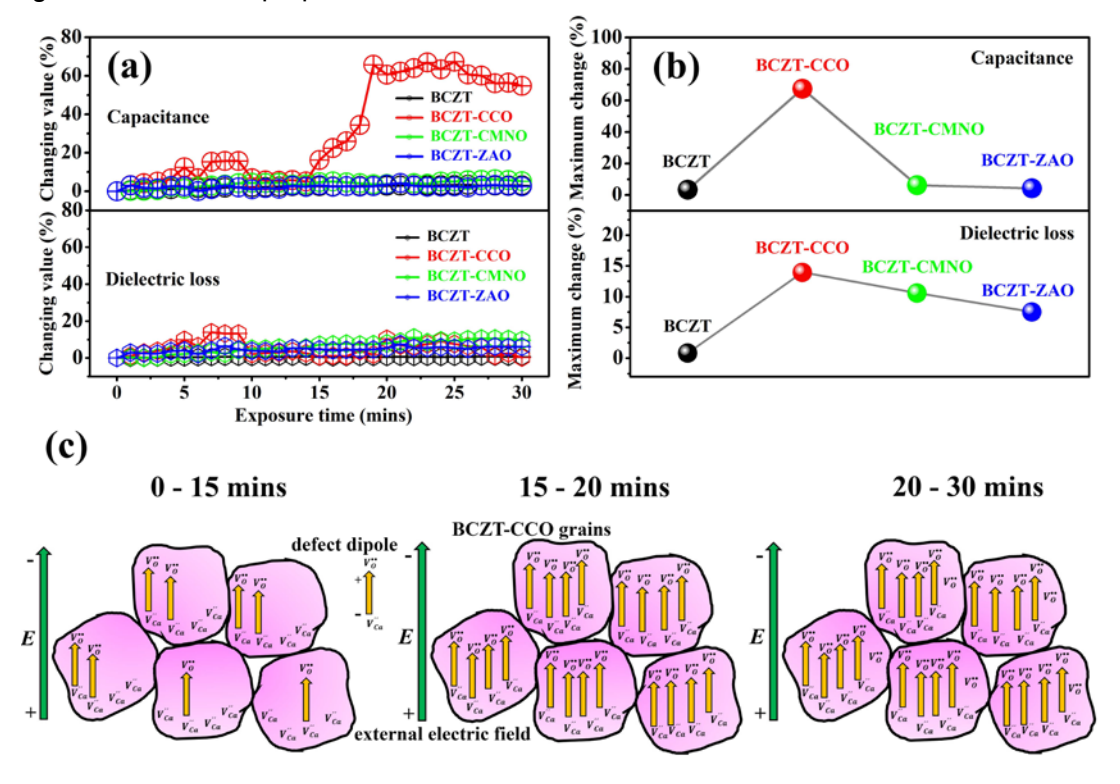


Figure 22 Dielectric properties of the selected ceramics

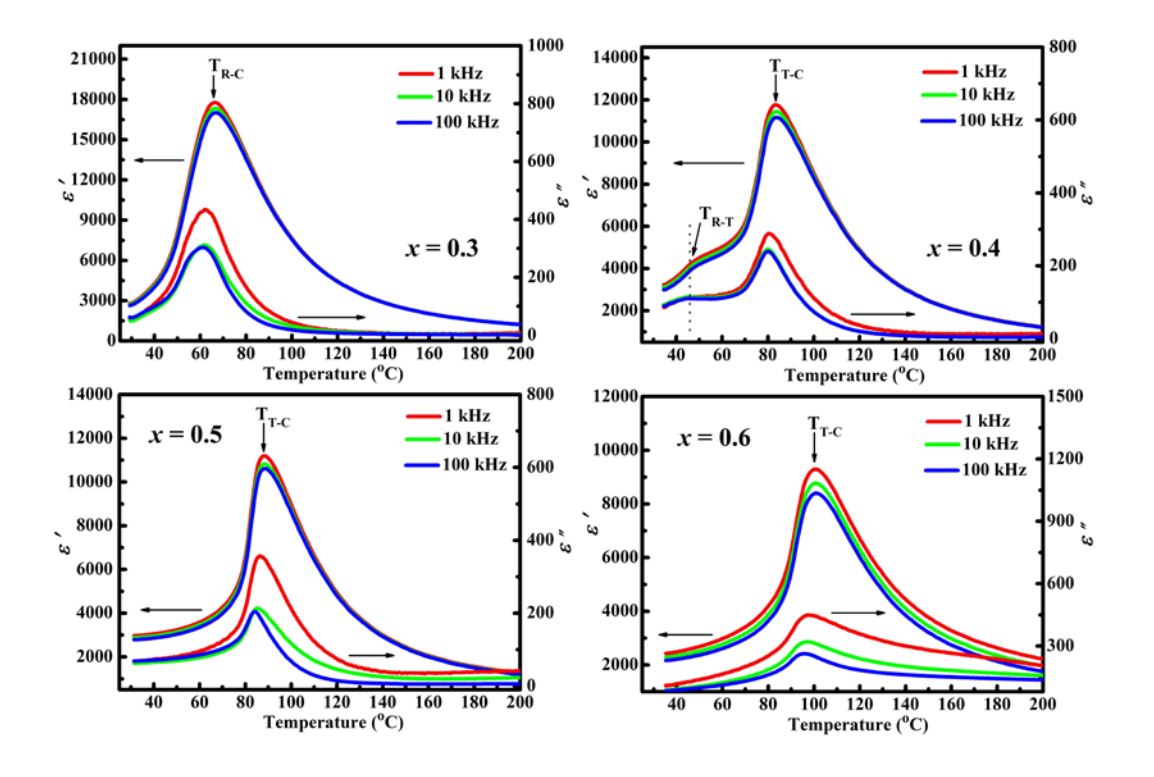


Figure 23 XPS spectrum of the selected ceramics

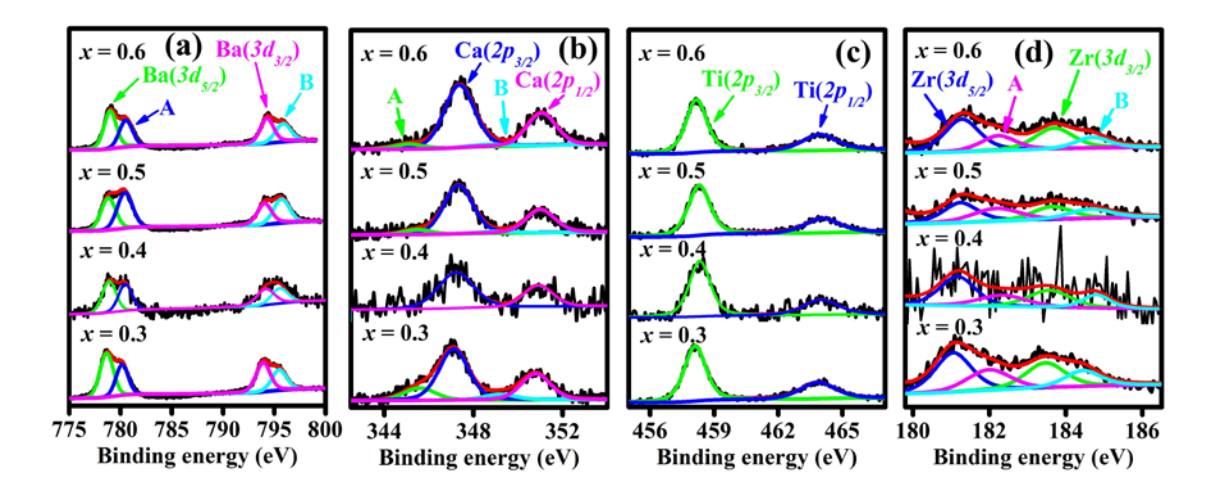


Figure 24 Piezoelectric coefficient of the selected ceramics

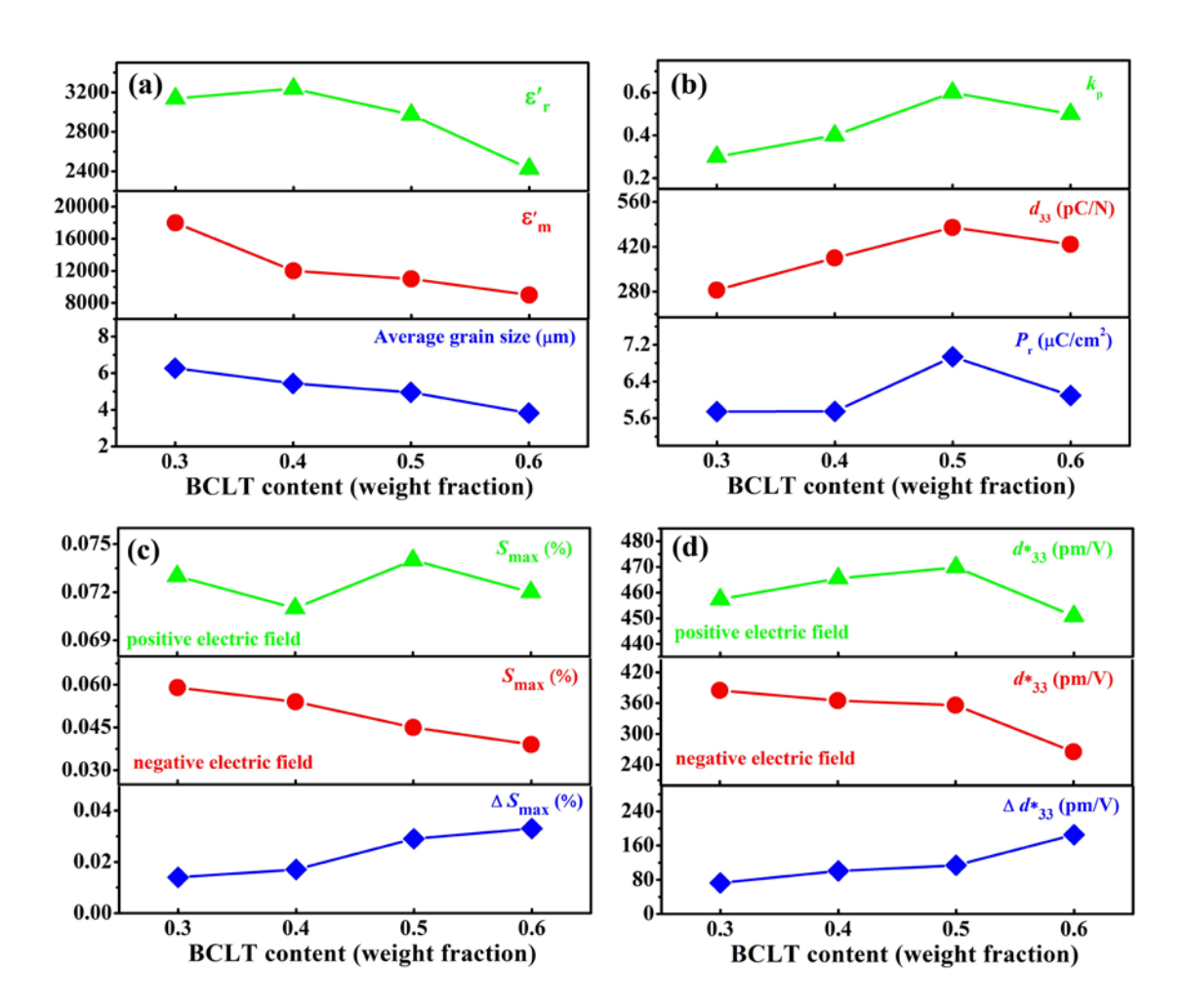


Figure 25 S-E hysteresis loop of the selected ceramics

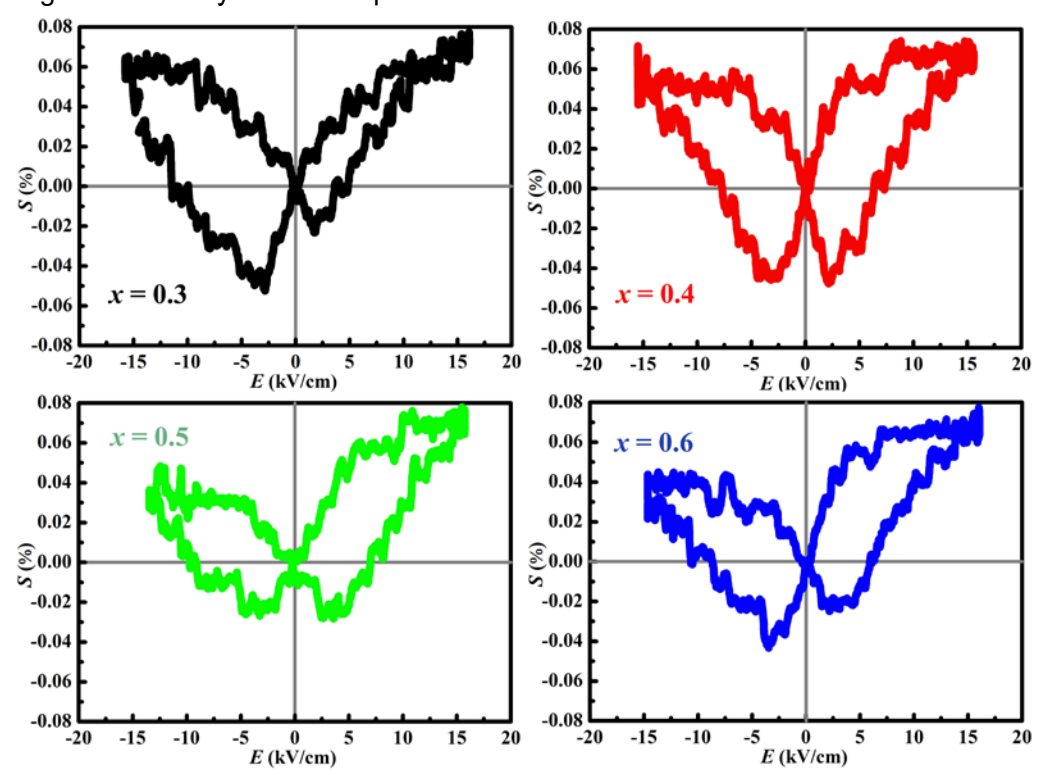
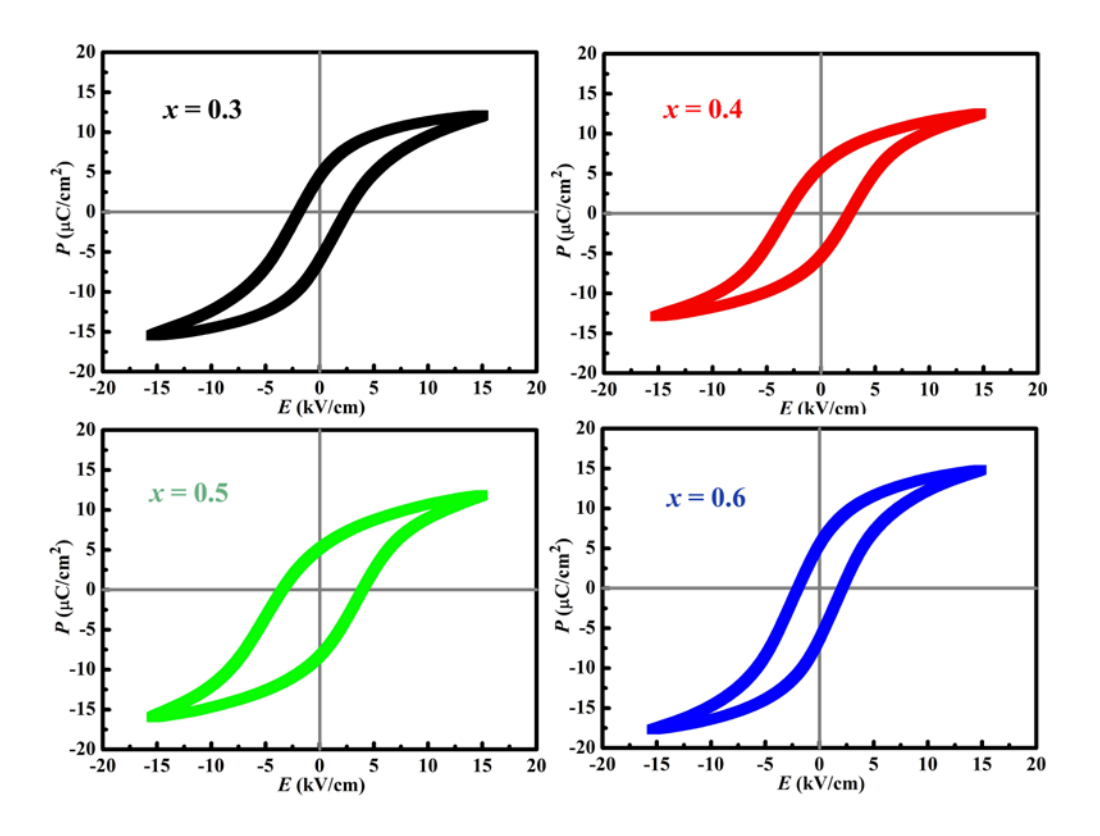


Figure 26 P-E hysteresis loop of the selected ceramics



Conclusion and Discussion

Fig. 20(a) shows XRD patterns of all ceramics. The result indicates a structure without a secondary phase of BCZT. Meanwhile, CaO and CaCO₃ exist in doped ceramics. The presence of both phases reflects the deficient content of Ca ions within the doped samples. Besides CaO and CaCO₃, a small intensity of CCO and ZnO peaks presents in BCZT-CCO and BCZT-ZAO, respectively. XRD patterns (44.5° - 46°) are plotted in Fig. 20(b). BCZT shows the splitting peaks of (002) and (200). Interestingly, both peaks become overlap when BCZT are doped. The possible reason is a substitution of dopant in perovskite lattice. In general, the ions having a similar ionic radius size can substitute in the crystal structure, which leads to the deformation of the lattice. With these ceramics, Ba²⁺ (1.61 Å), Ca²⁺ (1.34 Å), Zr⁴⁺ (0.72 Å), and Ti⁴⁺ (0.605 Å) host ions can be substituted by Co²⁺ (0.65 Å), Mn²⁺ (0.83 Å), and Zn²⁺ (0.74 Å) dopants [4].

Fig. 20(c) presents Ba-L₃ XAS spectra and BaCO₃ standard reference. The absorption peak at $E_{\rm o}$ ~5251 eV can be noticeable in all samples. This peak relates a resonant excitation from Ba $2p_{3/2}$ to Ba 5d unoccupied state, revealing Ba²⁺ in all ceramics. Interestingly, the width of the shoulder of $E_{\rm o}$ peak is different obviously. It should mention first that the width of the $E_{\rm o}$ peak indicates the average Ba-O interatomic distance [5]. The broad shoulder of $E_{\rm o}$ peak suggests the shorter average length of Ba and O atoms within the structure. Fig. 20(d) shows XAS spectra from 5243 to 5262 eV. BCZT shows the broad shoulder and small peak (i.e., peak A), suggesting more covalent bond in perovskite structure. Upon the doping, the different width of the shoulder is observed apparently for each dopant. This result reflects the deformation crystal structure in doped BCZT, which is agreement with their XRD patterns. Fig. 1(e) shows SEM images of all ceramics. The average grain sizes of BCZT, BCZT-CCO, BCZT-CMNO, and BCZT-ZAO are about 6.22, 1.35, 3.69, 5.47 μ m, respectively.

The capacitance and dielectric loss under UV light at different frequencies of all ceramics are shown in Fig. 19. The dielectric properties of BCZT do not change upon UV light, and the applied frequencies do not affect its UV light response. Interestingly, when the UV light incidents on BCZT-CCO ceramic at 1 kHz, the capacitance gradually increases from 415 pF to 435 pF. The maximum relative value is changed \sim 4.8% at 10 mins of exposure time which agrees with the photo-induced dielectric enhancement in STO-based ceramic [3]. However, its response decreases with higher frequency due to the polarization cannot follow to the applied external electric field at a higher frequency.

For CMNO- and ZAO-doped ceramics, the samples do not show the significant change in dielectric values after UV light exposure.

The changing value of dielectric properties and exposure time for 30 mins of all ceramics at 1 kHz is shown in Fig. 21 (a). BCZT, BCZT-CMNO, and BCZT-ZAO do not show a significant change in dielectric value. Interestingly, a rapid increase of capacitance occurs in a range from 15 to 20 mins in BCZT-CCO. Then, the value gradually becomes stable. The maximum dielectric response upon UV light of all ceramics is summarized in Fig. 21 (b). BCZT-CCO ceramic exhibit the maximum change of capacitance (~ 60 %) and dielectric loss (~ 15 %) whereas the dielectric response of other ceramics does not differ significantly. The dielectric enhancement of BCZT-CCO may be explained by the creation of a $(V_{Ca}^{"}-V_{O}^{\bullet\bullet})$ defect dipole between vacancies of Ca $(V_{Ca}^{"})$ and O $(V_{O}^{\bullet\bullet})$ ions. To describe the formation of defect dipole, it should be mentioned first that CaO and CaCO₃ secondary phases (Fig. 20 (a)) occur during the sintering process at a high temperature of the doped ceramics, which can be explained by Kröger-Vink notation in Eq. 1 and Eq. 2, respectively.

$$Ca_{Ca}^{x} + 1/2O_{2} + 2e' \rightarrow CaO + V_{Ca}''$$
 (1)

$$Ca_{Ca}^{x} + 1/2O_{2} + CO_{2} + 2e' \rightarrow CaCO_{3} + V_{Ca}''$$
 (2)

As seen the equations, $V_{Ca}^{"}$ is induced simultaneously in doped ceramics with the presence of CaO and CaCO₃ phases. When the ceramics is under UV light, $V_o^{\bullet\bullet}$ can be generated at the oxide surface, which given in Eq. 3. This phenomenon has been observed in other oxides such as CaCu₃TiO₄O₁₂ [6], and STO-based ceramics [3].

$$1/2O_2 \rightarrow O_O^x + V_O^{\bullet \bullet} + 2e' \tag{3}$$

Then, the negative charge of V''_{Ca} existing the ceramic can catch the positive charge of $V_O^{\bullet\bullet}$ immediately and induces $(V''_{Ca} - V_O^{\bullet\bullet})$ defect dipole as follow in Eq. 4

$$V_{Ca}'' + V_O^{\bullet \bullet} \rightarrow (V_{Ca}'' - V_O^{\bullet \bullet}) + 2e' + 2h^{\bullet}$$

$$\tag{4}$$

Nevertheless, the dielectric response of BCZT-CCO ceramic may not be similar to $CaCu_3TiO_4O_{12}$ [6], and STO-based ceramics [3]. In our case, V''_{Ca} has exhibited in the ceramic without UV light. When the ceramic is exposed by UV light, the dielectric variation is divided into three periods, including a range from 1 to 15 mins, 15 to 20

mins, and 20 to 30 mins as seen in Fig. 21 (c). For the first one, $V_0^{\bullet\bullet}$ are gradually produced and can catch $V_{\it Ca}''$ immediately, inducing $V_{\it Ca}'' - V_{\it O}^{\bullet \bullet}$ defect dipoles. The formation of defect dipoles increases dielectric properties of BCZT-CCO, which is agreement with the dielectric enhancement due to the creation of $V_{Ca}'' - V_O^{\bullet \bullet}$ defect dipole upon UV light in STO-based ceramics [3]. However, in the case of BCZT-CCO, the content of $V_0^{\bullet\bullet}$ in the first period may be smaller than V_{Ca}'' , resulting in the remaining content of $V_{{\it C}a}''$. For the second period, the $V_{\it O}^{\bullet \bullet}$ content increases much and may be sufficient to attract the remained $V_{\it Ca}''$. Defect dipoles $(V_{\it Ca}'' - V_{\it O}^{\bullet \bullet})$ are effectively formed, resulting in the rapid enhancement of the value. In the third period, the capacitance does not change much and becomes stable gradually. This result is possible that there are no V_{Ca}'' , which arrest $V_O^{\bullet \bullet}$, causing no more $V_{Ca}'' - V_O^{\bullet \bullet}$ defect dipoles. The capacitance value, therefore, becomes stable. After removing the UV light for 35 mins (see inset in Fig. 3(a)), the capacitance of BCZT-CCO decreases gradually and becomes rapidly after 20 mins, which related with its capacitance enhancement under UV light. This result is because that the re-enter of oxygen at the surface, causing the decrease in capacitance. This phenomenon has been observed in CaCu₃TiO₄O₁₂ [6], and STO-based ceramics [3]. In the case of the dielectric loss, the value decreases gradually but in slower rate as compared with the capacitance. Regarding BCZT-CMNO and BCZT-ZAO, the samples do not exhibit the enormous response of capacitance and dielectric loss similar to BCZT-CCO although CaO and CaCO3 phases present. It is because CCO is quite sensitive to O content or $V_0^{\bullet\bullet}$ [7]. Thus, upon UV light, $V_0^{\bullet\bullet}$ is therefore generated at BCZT-CCO surface easier than CMNO- and ZAO-doped samples, leading to the massive dielectric response in BCZT-CCO ceramic.

The Arrhenius plot of electrical conductivity (σ) of all ceramics is shown in Fig. 3(d). The temperature dependence of σ is fitted according to the Arrhenius equation,

$$\sigma = \sigma_o \exp(-E_a/kT) \tag{5}$$

Where σ_o , E_a , k, and T are the pre-exponential factor, the activation energy per charge carrier, Boltzmann's constant and the absolute temperature, respectively. The E_a value is extracted from the slope of linear fitting. The value indicates the energy required to move the defects, i.e., the thermally activated oxygen vacancies at high temperature [8]. Thus, the materials with low E_a value should have the more natural movement of $V_o^{\bullet\bullet}$. With these ceramics, BCZT shows the minimum value of E_a (~0.08 eV) meanwhile all doped ceramics show the higher E_a (~0.21 – 0.36 eV). Thus, the

 $V_o^{\bullet\bullet}$ defect can move in BCZT easily, which reflects a low E_a . In the case of the doped ceramics, the mobility of $V_o^{\bullet\bullet}$ is retarded by V_{Ca}'' , exhibiting in the doped ceramics. The E_a values of all doped ceramics are, therefore, higher than BCZT.

Conclusions

The presence of defect dipole between vacancies of Ca and O ions could enhance dielectric properties under UV light. BCZT-CCO showed maximum dielectric enhancement (~ 60 %) at 15 – 20 mins meanwhile other ceramics did not present a significant change. The results here suggested that the doping of CCO could be useful for tuning the UV light-induced dielectric response of BCZT which may find future application in UV light sensors, detector, and other optical devices.

Reference

- [1] W. Liu, X. Ren, Large piezoelectric effect in Pb-free ceramics, Phys. Rev. Lett. 103 (2009) 257602.
- Y. Zhang, H. Sun, W. Chen, A brief review of Ba(Ti_{0.8}Zr_{0.2})O₃-(Ba_{0.7}Ca_{0.3})TiO₃ based lead-free piezoelectric ceramics: Past, present and future perspectives, J. Phys. Chem. Solid 114 (2018) 207-219.
- [3] P. Jaiban, S. Buntham, A. Watcharapasorn, Dielectric properties of (1-x)Sr_{0.92}La_{0.08}TiO₃-(x)CaMn_{0.98}Nb_{0.02}O₃ ceramics under violet light irradiation Mater. Lett. 193 (2017) 133-137.
- [4] R.D. Shannon, Revised effective ionic radii and systematic studies of interatomic distance in halides and chalcogenides, Acta. Cryst. A32 (1976) 751-767.
- [5] K. Yoshii, I. Jarrige, C. Suzuki, D. Matsumura, Y. Nishihata, Y. Yoneda, T. Fukuda, K. Tamura, Y. Ito, T. Mukoyama, T. Tochio, H. Shinotsuka, S. Fukushima, Probing the Ba5d states in BaTiO₃ and BaSO₄: A resonant x-ray emission study at Ba-L₃ edge, J. Phys. Chem. Solid 73 (2012) 1106-1110.
- [6] C. Masingboon, T. Eknapakul, S. Suwanwong, P. Buaphet, H. Nakajima, S-K. Mo, P. Thongbai, P.D.C. King, S. Maensiri, W. Meevasana, Anomalous change in dielectric constant of CaCu3Ti4O12 under violet-to-ultraviolet irradiation, Appl. Phys. Lett. 102 (2013) 202903.
- [7] K.T. Jacab, P. Gupta, Oxygen potential sand phase equilibria in the system Ca–Co–O and thermodynamic properties of Ca₃Co₂O₆ and Ca₃Co₄O_{9.163}, J. Solid State Chem. 221 (2015) 57-65.

[8] S. Kumar, K.B.R. Varma, Influence of lanthanum doping on the dielectric, ferroelectric and relaxor behavior of barium titanate ceramics, J. Phys. D; Appl. Phys. 42 (2009) 075405.

Oxidation state and chemical environment

XPS was used to study the oxidation state and chemical environment at the surface of all ceramics only. Fig. 23(a-d) present the XPS profiles for Ba 3d, Ca 2p, Ti 2p, and Zr 3d core levels at the surface in all ceramics. As seen in Fig. 23(a), the Ba 3d peaks in all samples showed a good fit to four peaks, at binding energy (BE) values of approximately 778.6, 780.2, 794.0, and 795.5 eV. The green and pink peaks located at BEs of approximately 778.6 and 794.0 eV correspond to the spin-orbit doublet, i.e., Ba $3d_{5/2}$ and Ba $3d_{3/2}$ of the 3d core level of Ba ions, respectively. The spin-orbit energy separation (Δ E) between the Ba $3d_{5/2}$ and Ba $3d_{3/2}$ core levels was 15.4 eV, which accompanies bulk and nano BaTiO₃ [18]. This difference, therefore, confirmed the existence of Ba in the 2+ oxidation state (i.e., Ba2+ ions) in these ceramics. The shoulder peaks on the higher BE side at 780.2 and 795.5 eV, which were marked as A and B peaks, did not relate to the different oxidation state but indicated a relaxation phase formed at the ceramic surface to reduce surface strain [19]. Figure 23(b) illustrates the deconvoluted Ca 2p XPS profiles of all ceramics. The data showed a clear fit to two peaks, located at BE values of approximately 347.3 and 351.0 eV. Their BE values were associated with the Ca $2p_{3/2}$ and Ca $2p_{1/2}$ spin-orbit doublet core level of Ca. The ΔE value between the Ca $2p_{3/2}$ and Ca $2p_{1/2}$ core level was approximately 3.7 eV, indicating the presence of Ca2+ ions [19, 20] in these ceramics. Similarly, the two shoulder peaks on the higher BE side at 345.1 and 348.7 eV, marked as A and B peaks, respectively, were associated with the relaxation phase at the ceramic surface. The deconvolution of the Ti 2p XPS profiles of all ceramics is shown in Fig. 23(c). After fitting, the results indicated that two peaks are located at BEs of approximately 458.1 and 463.9 eV. These two peaks correspond to the Ti $2p_{3/2}$ and Ti $2p_{1/2}$ spin-orbit doublet, with ΔE of approximately 5.8 eV. This observation suggests the existence of Ti⁴⁺ ions in these ceramics, which is in good agreement with several previous reports [18-21]. Figure 23(d) shows the deconvoluted Zr 3d XPS profiles of all ceramics. As seen in the figure, the XPS profiles presented two-spin orbit peaks of Zr^{4+} , i.e., the $3d_{5/2}$ peak at a BE of 181.0 eV and the $3d_{3/2}$ peak at a BE of 183.5 eV, with Δ E \sim 2.5 eV, which is in good agreement with previous studies [22]. The shoulder peaks at 182.1 and

184.5 eV, marked as A and B peaks, were attributed to the reduction of surface strain [18].

Relationship between dielectric properties and phase transition

Figure 22 shows real (\mathcal{E}') and imaginary (\mathcal{E}'') parts of the relative permittivity as a function of temperature in the range from 25 °C to 200 °C and with frequencies ranging from 1 kHz to 100 kHz for all ceramics. The results indicated a sharp dielectric phase transition with increasing temperature. In addition to the sharp dielectric peak, the phase transition from the ferroelectric to cubic phase was observed at 65 °C, 80 °C, 90 °C, and 100 °C for the compositions x = 0.3, 0.4, 0.5, and 0.6, respectively. These phase transition temperatures were independent of the applied frequency, suggesting a normal ferroelectric behavior in these ceramics. Regarding the phase transition in these ceramics, it should be mentioned first that the 0.7BZT-0.3BCLT ceramic sample possessed a rhombohedral structure, as observed in its XRD pattern at room temperature. Thus, the phase transition at 65 °C should be a transformation from rhombohedral to cubic structure (T_{R-C}). On the contrary, (1-x)BZT-(x)BCLT compositions where $0.4 \le x \le 0.6$ indicated the presence of a tetragonal structure. Accordingly, the phase transitions, observed at 80 °C for x = 0.4, at 90 °C for x = 0.5, and at 100 °C for x = 0.6, should correspond to the transformation from the tetragonal to cubic phase (T_{T-1} _C). The T_{T-C} shifted to higher temperatures (i.e., from 80 °C to 100 °C) when the BCLT content increased. This was the fact that the phase transition temperatures of BZT and BCLT were -20 °C and 100 °C, respectively. Thus, when BCLT increased, the phase transition of BZT-BCLT system should increase. Besides, the increase in tetragonality of the ceramics listed in Table 1 could be the additional reason for the shift of T_{T-C} to higher temperatures. Since a result of the crystal structure with higher tetragonality, a higher temperature for the phase transformation from tetragonal to cubic structure would be required [14]. In addition to the shift in phase transition temperature, the results also suggest a change in dielectric permittivity at room temperature (\mathcal{E}'_{r}) and a maximum dielectric permittivity (ϵ'_{m}) at T_{R-C} for the composition x = 0.3 and at T_{T-C} for the others. This result will be discussed together with the grain size effect in the following section. With these dielectric results, interestingly, the sample with x = 0.4 showed a shoulder peak at 45 °C that was absent in the other ceramics. It is possible that this peak is related to the phase transformation from a rhombohedral to tetragonal structure (T_{R-T}). When considering the XRD results, the ceramic x = 0.4 exhibited coexistence of the rhombohedral and tetragonal phases at room temperature. Thus, with increasing

temperature for this composition, the rhombohedral phase was first transformed to a tetragonal structure, and the tetragonal phase was transformed to a cubic structure.

P-E and S-E hysteresis loops for all ceramics

The ferroelectric properties of the (1-x)BZT-(x)BCLT system with $0.3 \le x \le 0.6$ were determined using the relationship between polarisation and an applied external electric field (P-E hysteresis loop), as shown in Fig. 26. Figure 25 presents the electromechanical response of all ceramics, which was determined by a bipolar strain curve upon the applied external electric field (S-E or butterfly hysteresis loop). As seen in both figures, normal P-E and S-E hysteresis loops were observed for all ceramics. This result indicates that this ceramic is a normal ferroelectric material system.

Relationships among microstructure, crystal structure, and electrical properties Effects of average grain size on dielectric properties

Figure 24(a) summarises the influence of grain size on dielectric properties, including the dielectric permittivity at room temperature (\mathcal{E}'_r) and maximum dielectric permittivity (\mathcal{E}'_m), for these ceramics. As seen in the figure, both dielectric values decreased with increasing BCLT concentration. The change in these values was accompanied by a decreasing average grain size for (1-x)BZT-(x)BCLT ceramics. Thus, the reduction in grain size should play an important role in the decrease of the dielectric properties of this binary system. In general, the microstructure with smaller grains has larger grain boundaries, which slow domain wall movement, leading to a decrease in \mathcal{E}'_r , and \mathcal{E}'_m [27].

Effects of crystal structure and average grain size on ferroelectric properties

The P-E hysteresis loops of all ceramics are shown in Fig. 26. A slight offset of the P-E hysteresis loop could be observed in all ceramics. This was because of the contribution of their electrical conduction [28] and the presence of trapped space charges at the electrode-ferroelectric interface [29]. Thus, the ferroelectric parameters, including remanent polarisation (P_r), saturated polarisation (P_s), and coercive field (E_c), at the positive and negative electric fields were therefore extracted from their P-E hysteresis loop. From the table, there was no significant trend from the data extracted from the positive and negative electric fields. Thus, the average ferroelectric parameters (listed in Table 2 and Fig. 24(b)) could be used to explain the ferroelectric properties of these ceramics. From the average values, the P_r factors of BCLT compositions where $0.3 \le x \le 0.4$ did not differ significantly. Interestingly, the sample at 0.5BCLT concentration showed the maximum P_r value (i.e., ~ 7.2 μ C/cm²) and the value decreased with

increasing addition of BCLT. The presence of a single tetragonal phase induced an increase in P_r for the ceramics at compositions $x \ge 0.5$ because spontaneous polarisation was aligned with the [001] direction in the tetragonal phase. Therefore, the polarisation could lead to easier arrangement of the rhombohedral phase, which possessed [111] direction [29]. Regarding E_c , the value increased with increasing BCLT content up to x = 0.5. This could be attributed to the presence of a tetragonal phase. Strain could be induced during domain rotation in the tetragonal phase, which obstructs the switching of the domain. Meanwhile, the domain rotation in the rhombohedral phase was without induced strain [29]. Thus, the E_c value for the composition x = 0.5 was higher than it was for $x \le 0.4$. However, the reduction of P_r and E_c was observed in x = 0.6, even though the ceramic had a single tetragonal phase. The contribution of small grain size could be the additional reason for this decrease, as the ferroelectric domain would stabilize in large grains more readily than it would in smaller grains [30].

Effects of crystal structure and average grain size on small-signal piezoelectric properties

The small-signal piezoelectric properties were measured by application of pressure on the poled sample, via which the piezoelectric coefficient (d_{33}) and electromechanical coupling factor (k_n) were determined. From section, the presence of a tetragonal phase and decrease in the average grain size affected P_r for the ceramics. Thus, to explain the effects of crystal structure and grain size, the relationship between $P_{\rm r}$, d_{33} , and $k_{\rm p}$ as a function of BCLT content is plotted in Fig. 9(b). Regarding $P_{\rm r}$, for BCLT compositions where $0.3 \le x \le 0.4$, the ferroelectric factors did not differ significantly. Interestingly, the sample with 0.5BCLT concentration showed the maximum P_r value because of the presence of a tetragonal phase, which decreased at 0.6BCLT concentration because of the reduction in the average grain size. When compared with piezoelectric properties, the trend for the d_{33} and $k_{\rm p}$ values of these ceramics seemed to accompany a change in their P_r values. Thus, the small-signal piezoelectric response could be attributed to $P_{\rm r}$. It is worth mentioning first that the $d_{\rm 33}$ and $k_{\rm p}$ factors are related to a reversible contribution, i.e., rearrangement of spontaneous polarisation ($P_{\rm sp}$) [8]. Before the poling process, $P_{\rm sp}$ within the material is arranged randomly. When an external electric field is applied, $P_{\rm sp}$ will re-arrange in a direction similar to that of the applied electric field. After removing the external electric field, $P_{\rm sp}$ could either be maintained in the poled direction or revert back to the initial direction. A material with large $P_{\rm sp}$ in the poled direction shows better $d_{\rm 33}$ and $k_{\rm p}$ factors. With ferroelectric measurement, $P_{\rm r}$ can indicate the degree of rearrangement of $P_{\rm sp}$ after removing the

external electric field. Thus, in these ceramics, the sample with 0.5BCLT concentration possessed the maximum P_r ; therefore, it exhibited the maximum d_{33} and k_p factors. This result is in agreement with several previous reports [31, 32].

Effects of average grain size on large-signal piezoelectric properties

The decrease in grain size affected the strain response at high electric field for these ceramics. The maximum strain (S_{max}) and the ratio between the maximum strain and electric field (d^*_{33}) can be extracted from the S-E hysteresis curve (Fig. 25). Both factors are widely utilized to study this property. Figure 24(c) and (d) show respectively S_{max} and d_{33}^* values for these ceramics in the direction of a positive and negative electric field. In the positive direction, the results did not show any significant change in S_{max} and d^*_{33} . However, a decreasing trend for the S_{max} and d^*_{33} factors with increasing BCLT content was observed after the electric field was switched to the negative direction. This seemed to be associated with the decrease in the average grain size for these ceramics (Fig. 24(a)). It is well known that the increase in the strain of piezoelectric materials at high electric field is primarily due to irreversible contributions, i.e., the mobility of the domain wall [8]. Thus, a material with high domain wall motion should have better S_{max} and d_{33}^* factors. With these ceramics, the average grain size decreased with increasing BCLT content. The reduction in grain size led to larger grain boundaries. This result could prohibit movement of the domain wall and thus effectively reduce S_{max} and d^*_{33} as the BCLT content is increased. To further explain this phenomenon, the differences in these values in the positive and negative directions were therefore calculated and denoted ΔS_{max} and Δd_{33}^* in Fig. 24(c) and (d), respectively. ΔS_{max} and Δd_{33}^* indicate the prohibition of domain wall movement during switching of the applied electric field. In the figure, ΔS_{max} and Δd^*_{33} increased with increasing BCLT content. This result confirmed the further contribution of grain boundaries to domain wall switching in these ceramics.

Conclusions

(1-x)BZT-(x)BCLT ceramics, where x = 0.3, 0.4, 0.5, and 0.6, were fabricated using conventional solid-state sintering. Depending on BCLT content, the system showed three phase regions, including a single rhombohedral phase, a binary rhombohedral and tetragonal phase, and a single tetragonal structure. With increasing BCLT content, the grain size decreased and a single tetragonal phase existed, which significantly affected the dielectric, ferroelectric, and piezoelectric properties of these

ceramics. The addition of BCLT at x = 0.3 and 0.5 promoted the maximum dielectric properties and piezoelectric properties, respectively. The results here suggest a new phase diagram for the (1-x)BZT-(x)BCLT system, which can be tuned by the BCLT concentration and may be utilized as an alternative material in dielectric, ferroelectric, and piezoelectric devices.

Reference

- [1] T. Takenaka, K.I. Maruyama, K. Sakata, (Bi_{1/2}Na_{1/2})TiO₃-BaTiO₃ systems for lead-free piezoelectric ceramics. Jpn. J. Appl. Phys. 30 (1991) 2236-2239.
- [2] A.B. Haugen, J.S. Forrester, D. Damjanovic, B. Li, K.J. Bowman, J.L. Jones, Structure and phase transitions in 0.5(Ba0.7Ca0.3TiO3)-0.5(BaZr0.2Ti0.8O3) from -100 °C to 150 °C, J. Appl. Phys. 113 (2013) 014103.
- [3] P. Wannasut, P. Jaita, S. Jiansirisomboon, A. Watcharapasorn, Piezoelectric and ferroelectric properties of lead free Bi_{0.5}(Na_{0.80}K_{0.20})_{0.5}TiO₃-(Ba_{0.98}Nd_{0.20})TiO₃ binary system, Integr. Ferroelectr. 177 (2017) 10-16.
- [4] W. Liu, X. Ren, Large piezoelectric effect in Pb-free ceramics, Phys. Rev. Lett. 103 (2009) 257602.
- [5] Y. Zhang, H. Sun, W. Chen, A brief review of Ba(Ti_{0.8}Zr_{0.2})O₃-(Ba_{0.7}Ca_{0.3})TiO₃ based lead-free piezoelectric ceramics: Past, present and future perspectives, J. Phys. Chem. Solid 114 (2018) 207-219.
- [6] D.S. Keeble, F. Benabdallah, P.A. Thomas, M. Maglione, J. Kreisel, Revised structure phase diagram of (Ba_{0.7}Ca_{0.3}TiO₃)-(BaZr_{0.2}Ti_{0.8}O₃), Appl. Phys. Lett. 102 (2013) 092903.
- [7] J. Gao, X. Hu, L. Zhang, F. Li, L. Zhang, Y. Wang, Y. Hao, L. Zhong, X. Ren, Major contributor to the large piezoelectric response in $(1-x)Ba(Zr_{0.2}Ti_{0.8})O_3-x(Ba_{0.7}Ca_{0.3})TiO_3$ ceramics: Domain wall motion, Appl. Phys. Lett. 104 (2014) 252909.
- [8] M. Acosta, N. Novak, W. Jo, J. Rödel, Relationship between electromechanical properties and phase diagram in the Ba(Zr_{0.2}Ti_{0.8})O₃-x(Ba_{0.7}Ca_{0.3})TiO₃ lead-free piezoceramic, Acta Materialia 80 (2014) 48-55.
- [9] <u>S. Mahajan, D. Haridas, K. Sreenivas, O.P. Thakur, C. Prakash, Enhancement in electro-strain behavior by La³⁺ substitution in lead free BaZr_{0.05}Ti_{0.95}O₃ ceramics, Mater. Lett. 97 (2013) 40-43.</u>
- [10] M.L. Cheah, K.A. Razak, C.Y. Ng, Properties of lanthanum-doped bismuth sodium titanate (Bi_{0.5}Na_{0.5}TiO₃) prepared by soft combustion technique, Adv. Mat. Res. 858 (2014) 141-146.

- [11] R. Kumar, K. Asokan, S. Patnaik, B. Birajdar, Evolution of relaxor properties in lanthanum (La) doped barium zirconate titanate, Ferroelectrics 517 (2017) 8-13.
- [12] A. Mahmood, E. Mensur, A. Abdul, Naeem, Y. Iqbal, A. Ullah, S. Alkoy, Effect of La substitution on the microstructure and dielectric properties of the sol-gel derived BaZr_{0.2}Ti_{0.8}O₃ thin films, Thin Solid Films, 611 (2016) 68-73.
- [13] P. Jaiban, O. Namsar, S. Jiansirisomboon, A. Watcharapasorn, R. Yimnirun, Electrical properties of La-doped Ba_{0.7}Ca_{0.3}TiO₃ lead-free ceramics, Ferroelectrics 487 (2015) 86-93.
- [14] P. Jaiban, S. Suwanwong, O. Namsar, A. Watcharapasorn, W. Meevasana, Simultaneous tuning of the dielectric property and photo-induced conductivity in ferroelectric Ba_{0.7}Ca_{0.3}TiO₃ via La doping, Mater. Lett. 147 (2015) 29-33.
- [15] D. Gao, K.W. Kwok, D. Lin, H.L.W. Chan, Microstructure and electrical properties of La-modified K_{0.5}Na_{0.5}NbO₃ lead-free piezoelectric ceramics, J. Phys. D. 42 (2009) 035411.
- [16] B.H. Toby, R.B.V. Dreele, GSAS-II: the genesis of a modern open-source all purpose crystallography software package J. Appl. Cryst. 46 (2013) 544-549.
- [17] R.D. Shannon, Revised effective ionic radii and systematic studies of interatomic distance in halides and chalcogenides, Accta. Cryst. A32 (1976) 751-767.
- [18] M.F. Toomey, K. Gao, G.P. Medis, E.B. Slamovich, J.A. Howarter, Hydrothermal synthesis and processing of barium titanate nanoparticles embedded in polymer films, ACS Appl. Mater. Interfaces 7 (2015) 28640-28646.
- [19] M.D.C. Blanco López, G. Fourlaris, B. Rand, F.L. Riley, Characterization of barium titanate powders: barium carbonate identification, J. Am. Ceram. Soc. 82 (1999) 1777-1786.
- [20] H. Zou, D. Peng, G. Wu, X. Wang, D. Bao, J. Li, Y. Li, X. Yao, Polarization-induced enhancment of photoluminescence in Pr³⁺ doped ferroelectric diphase BaTiO₃-CaTiO₃ ceramics, J. Appl. Phys. 114 (2013) 73103.
- [21] J.F. Moulder, W.F. Stickle, P.E. Sobol, K.D. Bomben, Handbook of X-ray photoelectorn spectroscopy, vol. 8 Physical Electonics, Eden Prairie, MN, 1995.
- [22] I. Bespalov, M. Datler, S. Buhr, W. Drachsel, G. Ruppreshter, Y. Suchorski, Initial stages of oxide formation on the Zr surface at low oxygen pressure: an in situ FIM and XPS study, Ultamicroscopy 159 (Pt 2) (2015) 147-151.
- [23] W. Jinshu, Z. Meiling, N. Zuoren, Z. Jiuxing, Z. Tieyong, W. Yiman, A study of diffusion behavior of element lanthanum and oxygen in Mo-La₂O₃ cathode, J. Alloys Compd. 311 (2000) 82-85.

- [24] E. Nasi, D. Tillotson, The rate of diffusion of Ca²⁺ and Ba²⁺ in a nerve cell body, Biophys. J. Biophysical Soc. 47 (1985) 735-738.
- [25] D.L. Zhang, C.X. Qiu, W.J. Du, W.H. Wong, E.Y.B. Pun, Zr⁴⁺/Ti⁴⁺ codiffusion characteristics in lithium niobate, J. Am. Ceram. Soc. 98 (2015) 567-573.
- [26] P.D. Beattie, V.I. Basura, S. Holdcroft, Temperature and pressure dependence of O_2 reduction at Pt vertical bar Nafion((R)) 117 and Pt vertical bar BAM((R)) 407 interfaces, J. Electroanal. Chem. 468 (1999) 180-192.
- [27] P. Jaiban, A. Watcharapasorn, R. Yimnirun, R. Guo, A.S. Bhalla, Effects of donor and acceptor doping on dielectric and ferroelectric properties of Ba_{0.7}Ca_{0.3}TiO₃ lead-free ceramics, J. Alloys Compd. 695 (2017) 1329-1335.
- [28] L. Zheng, C. Lin, W.P. Xu, M. Okuyama, Vertical drift of P-E hysteresis loop in asymmetric ferroelectric capacitors, J. Appl. Phys. 79 (1996) 8634. http://dx.doi.org/10.1063/1.362485
- [29] M. Khodaei, D. Seol, S.A.S. Ebrahimi, Y.J. Park, H. Seo, Y. Kim, S. Baik, Ferroelectric and piezoelectric behavior of (111)-oriented Pb(Zr_xTi_{1-x})O₃ thin films on cobalt ferrite nano-seed layered Pt(111)/Si substrate, J. Mater Sci: Mater. Electron 25 (2014) 1696-1702.
- [30] N. Thongmee, R. Sumang, S. Pojprapai, T. Klaytae, Influence of BLT content on phase structure and electrical properties of (1-x)BT-(x)BLT ceramic, J. Metal Mater. Miner. 28 (2018) 109-115.
- [31] P. Jaiban, A. Watcharapasorn, Effects of Mg doping on electrical properties of Ba_{0.7}Ca_{0.3}TiO₃ ceramics, Mater. Today Comm. 11 (2017) 184-190.
- [32] P. Jaiban, A. Watcharapasorn, R. Yimnirun, R. Guo, A.S. Bhalla, Dielectric, ferroelectric and piezoelectric properties of (Ba_{0.7}Ca_{0.3})Ti_{1-x}Cu_xO_{3-x} ceramics, J. Alloys Compd. 759 (2018) 120-127.

Output and Appendix

- Jaiban P*, Tongtham M, Wannasut P, Pisitpipathsin N, Namsar O, Chanlek N, Pojprapai S, Yimnirun R, Guo R, Bhalla A, Watcharapasorn A, Phase characteristics, microstructure, and electrical properties of (1-x)BaZr_{0.2}Ti_{0.8}O₃-(x)(Ba_{0.7}Ca_{0.3})_{0.985}La_{0.01}TiO₃ ceramics. Ceram. Int. 45 (2019) 17502-17511.
- Jaiban P*, Tongtham M, Wannasut P, Watcharapasorn A, Dielectric response on ultraviolet light irradiation of Ba_{0.85}Ca_{0.15}Zr_{0.1}Ti_{0.9}O₃ based ceramics, Mater. Lett. 243 (2019) 169-172.
- Jaiban P*, Wannasut P, Yimnirun R, Watcharapasorn A, Influences of acceptor dopants (Cu, Mg, Fe) on electrical and optical properties of Ba_{0.7}Ca_{0.3}TiO₃ ceramics, Mater. Res. Bullet. 118 (2019) 110501.

ELSEVIER

Contents lists available at ScienceDirect

Ceramics International

journal homepage: www.elsevier.com/locate/ceramint



Phase characteristics, microstructure, and electrical properties of (1-x) BaZr_{0.2}Ti_{0.8}O₃-(x)(Ba_{0.7}Ca_{0.3})_{0.985}La_{0.01}TiO₃ ceramics



Panupong Jaiban^{a,*}, Maneeporn Tongtham^a, Pimpilai Wannasut^b, Nuttapon Pisitpipathsin^c, Orapim Namsar^d, Narong Chanlek^e, Soodkhet Pojprapai^d, Rattikorn Yimnirun^f, Ruyan Guo^g, Amar S. Bhalla^g, Anucha Watcharapasorn^{b,h}

- ^a Faculty of Science, Energy and Environment, King Mongkut's University of Technology North Bangkok, Rayong Campus, Rayong, 21120, Thailand
- b Department of Physics and Materials Science, Faculty of Science, Chiang Mai University, Chiang Mai, 50200, Thailand
- ^c Department of Applied Physics, Faculty of Sciences and Liberal Arts, Rajamangala University of Technology Isan, Nakhon Ratchasima, 30000, Thailand
- ^d School of Ceramic Engineering, Institute of Engineering, Suranaree University of Technology, Nakhon Ratchasima, 30000, Thailand
- e Synchrotron Light Research Institute, Nakhon Ratchasima, 30000, Thailand
- f School of Energy Science and Engineering, Vidyasirimedhi Institute of Science and Technology, Rayong, 21210, Thailand
- g Department of Electrical and Computer Engineering, College of Engineering, The University of Texas at San Antonio, San Antonio, TX, 78249, USA
- h Research Center in Physics and Astronomy, Faculty of Science, Chiang Mai University, Chiang Mai, 50200, Thailand

ARTICLE INFO

Keywords: Crystal structure Phase diagrams Piezoelectricity Phase transitions Oxide materials

ABSTRACT

In this study, $(1-x)\text{BaZr}_{0.2}\text{Ti}_{0.8}\text{O}_3$ - $(x)(\text{Ba}_{0.7}\text{Ca}_{0.3})_{0.985}\text{La}_{0.01}\text{TiO}_3$ ((1-x)BZT-(x)BCLT) ceramics, where x=0.3, 0.4, 0.5, and 0.6, were prepared employing a conventional solid-state sintering technique. X-ray diffraction patterns and dielectric measurements indicated three phase regions at room temperature, including a single rhombohedral (x=0.3), a phase coexistence of rhombohedral and tetragonal (x=0.4), and a single tetragonal structure ($x\ge0.5$). X-ray photoemission spectra at the surface of ceramics confirmed the oxidation state of Ba^{2+} , Ca^{2+} , Ti^{4+} , and Zr^{4+} ions. Upon BCLT addition, the reduction of the average grain size and the presence of the tetragonal structure significantly affected the dielectric, ferroelectric, and piezoelectric properties of these ceramics. With these results, the composition x=0.3 showed maximum ε_r and ε_m , whereas the composition x=0.5 showed maximum ε_r and ε_r whereas the composition ε_r and ε_r are results suggest a new phase diagram for the (1- ε_r) BZT-(ε_r)BCLT system, which could be tuneable by BCLT concentration and might be useful as an alternative material in dielectric, ferroelectric, and piezoelectric devices.

1. Introduction

In recent years, focus on the development of a binary lead-free ceramic system has rapidly increased because binary materials have shown attractive piezoelectric properties that are equivalent to or better than a commercial lead-based piezoelectric material, e.g., lead zirconate titanate (PZT) compound [1–8]. Among the binary lead-free ceramics, the (1-x)BaZr_{0.2}Ti_{0.8}O₃-(x)Ba_{0.7}Ca_{0.3}TiO₃ (BZT-BCT) solid solution, where x = 0.3–0.6, is being particularly investigated because of its potential to replace PZT in several electronic devices, such as sensors, actuators, and capacitors [4–8]. In previous studies, most of the development of BZT-BCT has focused on the relationship between the crystal structure dependence of the BCT concentration and the dielectric and piezoelectric properties [4–8]. However, the effects of the substitution of dopants on the properties of BZT-BCT binary ceramics

have received relatively little attention. Therefore, we are interested in studying the effects of dopants on the properties of this binary system.

It is well known that the electrical properties of perovskite materials can be tuned by aliovalent doping with, for example, ${\rm La^{3+}}$, ${\rm Fe^{3+}}$, ${\rm Nb^{5+}}$, ${\rm Ta^{5+}}$, ${\rm Cu^{2+}}$, and ${\rm Mg^{2+}}$ ions. Among these dopants, ${\rm La^{3+}}$ substitution induces a significant change in the ferroelectric, dielectric, and piezoelectric properties of well-known perovskite materials, such as BaTiO₃-based [9], ${\rm Bi_{0.5}Na_{0.5}TiO_3}$ -based [10], ${\rm Ba(Zr_xTi_{1-x})O_3}$ -based [11,12], ${\rm Ba_{0.7}Ca_{0.3}TiO_3}$ -based [13,14], and ${\rm K_{0.5}Na_{0.5}NbO_3}$ -based ceramics [15]. With these La-doped ceramics, a composition with the formula (${\rm Ba_{0.7}Ca_{0.3}}$)_{0.985}La_{0.01}TiO₃ (BCLT) has promoted significant enhancement (~50%) of the dielectric constant of BCT ceramics [13,14]. However, the dielectric, ferroelectric, and piezoelectric responses of the BZT-BCLT system have not yet been studied. Therefore, we are interested in investigating the BZT-BCLT system to search for a new binary

E-mail address: p.jaiban@gmail.com (P. Jaiban).

^{*} Corresponding author.

ceramic that can be employed as an alternative material for dielectric and piezoelectric devices. In this work, $(1-x)BaZr_{0.2}Ti_{0.8}O_3-(x)$ $(Ba_{0.7}Ca_{0.3})_{0.985}La_{0.01}TiO_3$ ((1-x)BZT-(x)BCLT) ceramics, where $x=0.3,\ 0.4,\ 0.5,\$ and $0.6,\$ were fabricated. The crystal structure and chemical composition were investigated by X-ray diffraction (XRD) measurements and X-ray photoelectron spectroscopy (XPS), respectively. Scanning electron microscopy (SEM) was used to observe the microstructure. With these results, the effects of the relationship between the phase formation and microstructural features on changes in the dielectric, piezoelectric, and ferroelectric properties of a novel (1-x) BZT-(x)BCLT ceramic system were examined and discussed.

2. Materials and methods

2.1. Materials

The starting materials were $BaCO_3$ (98.5%, Sigma-Aldrich), TiO_2 (99.9%, Riedel-de Haën), and ZrO_2 (98.5%, Sigma-Aldrich) for BZT and $BaCO_3$ (98.5%, Sigma-Aldrich), $CaCO_3$ (99.95%, Sigma-Aldrich), La_2O_3 (99.9%, Riedel-de Haën), and TiO_2 (99.9%, Riedel-de Haën) for BCLT.

2.2. Preparation of barium zirconate titanate - barium calcium lanthanum titanate ((1-x)BZT-(x)BCLT) powders

The starting oxides were weighed following the chemical formulae of $BaZr_{0.2}Ti_{0.8}O_3$ (BZT) and $(Ba_{0.7}Ca_{0.3})_{0.985}La_{0.01}TiO_3$ (BCLT). The oxide mixtures were ball-milled in ethanol (> 99.5%, Merck) for 24 h using a conventional mixed-oxide method. The mixed powders were dried at 120 °C for 24 h and calcined in a closed alumina crucible at 1100 °C for 3 h. After sieving, (1-x)BZT-(x)BCLT binary powders, where $x=0.3,\ 0.4,\ 0.5,\$ and $0.6,\$ were mixed again in ethanol (> 99.5%, Merck) for 6 h and dried at 120 °C for 24 h.

2.3. Preparation of barium zirconate titanate - barium calcium lanthanum titanate ((1-x)BZT-(x)BCLT) ceramics

A conventional solid-state sintering technique was used to fabricate all samples. After obtaining BZT-BCLT binary powders, one drop of 3 wt % PVA (polyvinyl alcohol, Merck) binder was added to the BZT-BCLT powders ($\sim 1\,\mathrm{g}$), which were subsequently pressed into pellets with a diameter of 10 mm and thickness of 2 mm using a uniaxial press with a pressure of 187.3 MPa. Binder removal was carried out by heating the pellets at 500 °C for 1 h in an air atmosphere with a heating/cooling rate of 5 °C/min. These pellets were then sintered at 1400 °C for 4 h in an air atmosphere with a heating/cooling rate of 5 °C/min on an alumina plate.

2.4. Characterisation

The bulk densities of all ceramics were determined using Archimedes' method. Then, the relative densities of the ceramics were calculated from the relationship between the theoretical and bulk densities. Phase identification of the sintered samples was performed in a 2θ range of $20-80^\circ$ using an X-ray diffractometer (Miniflex, Rigaku). Subsequently, the lattice parameters of all ceramics were obtained by the Rietveld refinement method using GSAS software [16]. The reference data for the BaTiO₃ phase, with a tetragonal structure (*P4mm*) and rhombohedral structure (*R3m*), were used as the initial data for the refinement of the XRD patterns of all samples.

The chemical composition at the surface of all ceramics was studied by XPS using a PHI 5000 Versa Probe II (ULVAC-PHI, Japan) at the SUT-NANOTEC-SLRI joint research facility, Beamline 5.3:SUT-NANOTEC-SLRI XPS, Synchrotron Light Research Institute (SLRI), Thailand. Monochromatic Al K α X-rays (1486.6 eV) were used as an excitation source. All binding energies of the samples were calibrated with the C1s (C–C bond) peak, with a binding energy at of 284.8 eV.

Microstructural observation of the as-sintered surface of the samples was carried out by SEM (JEOL JSM 6335F).

2.5. Electrical properties

2.5.1. Dielectric measurement

The sintered ceramics, with a diameter of 10 mm, were polished to decrease the thickness of the samples to ~ 1 mm. After obtaining the desired thickness, silver electrodes (PCC11889, Heraeus) were coated on both surfaces of the polished ceramics by brush painting. Subsequently, the painted samples were treated at 500 °C for 15 min in an air atmosphere with a heating/cooling rate of 5 °C/min. An LCR-meter (B4262 Agilent) was used to measure the dielectric properties, i.e., the capacitance and dielectric loss ($tan\,\delta$), as a function of the temperature of the samples in a frequency range of 1 to 100 kHz. Then, the real (ϵ') and imaginary (ϵ') parts of the obtained values were calculated.

2.5.2. P-E and S-E hysteresis loop measurements

The silver electrodes were coated on both surfaces of the polished ceramics with a similar process of dielectric measurement. The ceramic samples were then subjected to a bipolar electric field of $15\,\mathrm{kV/cm}$ at a frequency of 50 Hz using a custom-built electrical fatigue testing machine equipped with a Sawyer-Tower circuit to determine the P-E hysteresis loops. In addition, the strain-electric field (S-E) hysteresis loops of the ceramics were also measured using an inductive position sensor (LVDT) under a bipolar electric field of $15\,\mathrm{kV/cm}$ at a frequency of $50\,\mathrm{mHz}$. It should be noted that the measuring frequencies for P-E and S-E hysteresis loops were different because we used LVDT for S-E loop measurement. Thus, it was quite difficult to obtain the apparent data of S-E hysteresis loop at $50\,\mathrm{Hz}$.

2.5.3. Piezoelectric measurements

For piezoelectric measurement, all ceramics were poled in a silicone oil bath under a DC electric field of $3.5\,\mathrm{kV/cm}$ for $30\,\mathrm{min}$. The piezoelectric coefficient was then measured using a quasi-static $d_{33}\,\mathrm{m}$ (90–2030, ACPI) by applying a mechanical force to the electrode surfaces of the sample, where the generated voltage across the sample was recorded. The planar electromechanical coupling coefficient was determined by measuring the resonant and anti-resonant frequencies from the first minimum and maximum admittance peaks using a 4284A LCR-meter.

3. Results and discussion

3.1. Crystal structure and phase characteristics

XRD patterns of all ceramics are illustrated in Fig. 1(a). The sintered samples showed a perovskite structure without a secondary phase, suggesting a substantial state reaction during the sintering process. In addition to the absence of other phases, a shift in XRD peaks to a higher diffraction angle with increasing BCLT content was observed in Fig. 1(b). This change was due to a decrease in the lattice parameters and unit cell volume (Fig. 1(e)) attributed to larger Ba²⁺ ions (1.61 Å) at the A-site being substituted by smaller Ca²⁺ (1.34 Å) and La³⁺ (1.36 Å) ions [17]. To explain further the phase formation of this binary system, X-ray peak fitting at selected diffraction angles (i.e., ~22° and 45°) was carried out (Fig. 1(c) and (d), respectively). The reference data corresponding to a tetragonal structure (P4mm; CODID: 1507756) and rhombohedral structure (R3m; CODID: 9014179) was used as the starting phases for BCLT and BZT, respectively. Refined parameters included the lattice parameters, atomic positions, isotropic atomic displacement parameters (Uiso), site occupancy, 20 zero offsets, intensity scale factor, profile shape parameters, and background. The quality of fit (R_{wp}) was 10.2% for x = 0.3, 10.7% for x = 0.4, 9.3% for x = 0.5, and 9.8% for x = 0.6. After fitting analysis, the composition

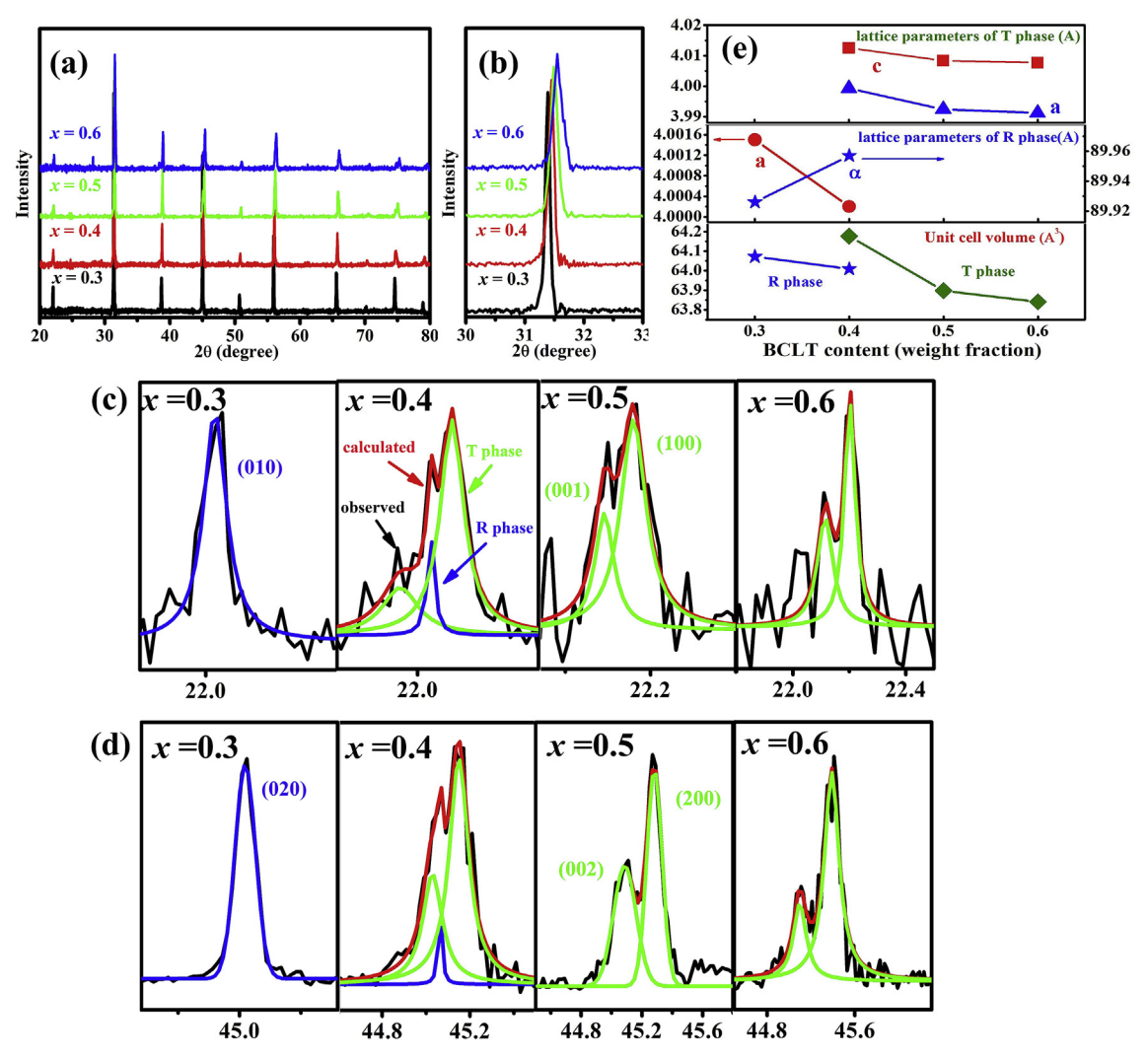


Fig. 1. Phase identification for all ceramics: (a) and (b) are XRD patterns in the 2-theta range of 20°-80° and 30°-33°, respectively. (c) and (d) are peak fitting for all ceramics. (e) shows lattice parameters and cell volume for all ceramics.

x=0.3 showed a single rhombohedral phase (BZT) with (010) and (020) blue peaks, and the composition $x \ge 0.5$ showed a single tetragonal phase (BCLT) with (001) and (100) green peaks. Meanwhile, the composition x=0.4 showed the coexistence of rhombohedral and tetragonal phases. This result suggests that the solid solubility limit of BCLT in BZT occurs at x=0.4, which has been suggested for the (1-x) BZT-(x)BCT system in several previous works [4,5,7]. The influence of these phase regions will be discussed, together with their dielectric results, in a later section.

3.2. Oxidation state and chemical environment

XPS was used to study the oxidation state and chemical environment at the surface of all ceramics only. Fig. 2(a–d) present the XPS profiles for Ba 3d, Ca 2p, Ti 2p, and Zr 3d core levels at the surface in all ceramics. As seen in Fig. 2(a), the Ba 3d peaks in all samples showed a good fit to four peaks, at binding energy (BE) values of approximately 778.6, 780.2, 794.0, and 795.5 eV. The green and pink peaks located at BEs of approximately 778.6 and 794.0 eV correspond to the spin-orbit doublet, i.e., Ba $3d_{5/2}$ and Ba $3d_{3/2}$ of the 3d core level of Ba ions, respectively. The spin-orbit energy separation (Δ E) between the Ba $3d_{5/2}$ and Ba $3d_{3/2}$ core levels was 15.4 eV, which accompanies bulk and nano BaTiO₃ [18]. This difference, therefore, confirmed the existence of Ba in the 2 + oxidation state (i.e., Ba²⁺ ions) in these ceramics. The

shoulder peaks on the higher BE side at 780.2 and 795.5 eV, which were marked as A and B peaks, did not relate to the different oxidation state but indicated a relaxation phase formed at the ceramic surface to reduce surface strain [19]. Fig. 2(b) illustrates the deconvoluted Ca 2p XPS profiles of all ceramics. The data showed a clear fit to two peaks, located at BE values of approximately 347.3 and 351.0 eV. Their BE values were associated with the Ca $2p_{3/2}$ and Ca $2p_{1/2}$ spin-orbit doublet core level of Ca. The ΔE value between the Ca $2p_{3/2}$ and Ca $2p_{1/2}$ ₂ core level was approximately 3.7 eV, indicating the presence of Ca²⁺ ions [19,20] in these ceramics. Similarly, the two shoulder peaks on the higher BE side at 345.1 and 348.7 eV, marked as A and B peaks, respectively, were associated with the relaxation phase at the ceramic surface. The deconvolution of the Ti 2p XPS profiles of all ceramics is shown in Fig. 2(c). After fitting, the results indicated that two peaks are located at BEs of approximately 458.1 and 463.9 eV. These two peaks correspond to the Ti $2p_{3/2}$ and Ti $2p_{1/2}$ spin-orbit doublet, with ΔE of approximately 5.8 eV. This observation suggests the existence of Ti⁴⁺ ions in these ceramics, which is in good agreement with several previous reports [18-21]. Fig. 2(d) shows the deconvoluted Zr 3d XPS profiles of all ceramics. As seen in the figure, the XPS profiles presented two-spin orbit peaks of Zr^{4+} , i.e., the $3d_{5/2}$ peak at a BE of 181.0 eV and the $3d_{3/2}$ peak at a BE of 183.5 eV, with $\Delta E \sim 2.5$ eV, which is in good agreement with previous studies [22]. The shoulder peaks at 182.1 and 184.5 eV, marked as A and B peaks, were attributed to the reduction of

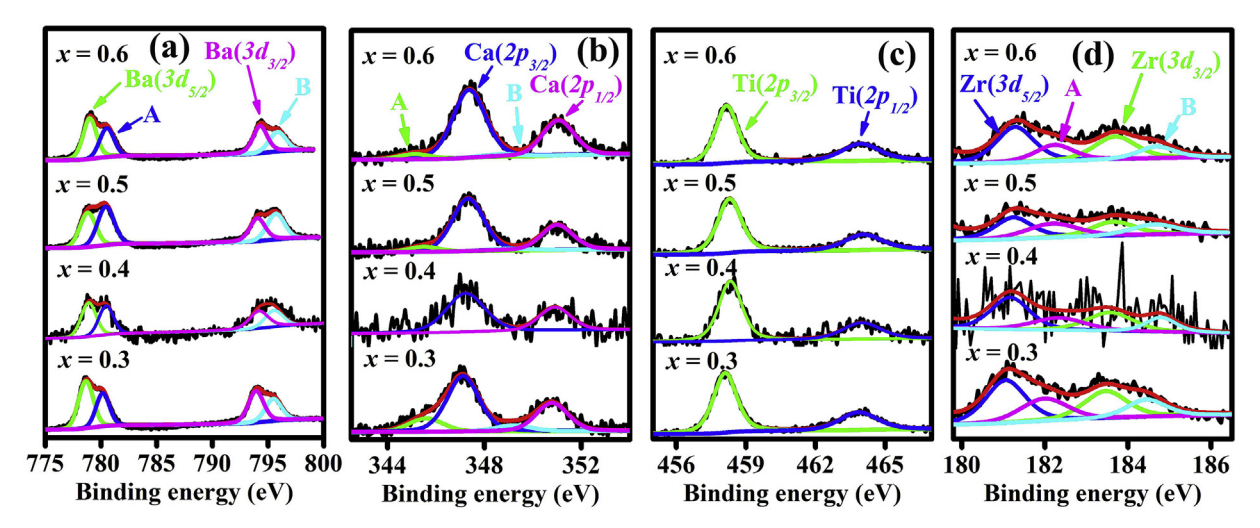


Fig. 2. XPS profiles of all ceramics; (a)-(d) are Ba3d, Ca2p, Ti2p, and Zr3d, respectively.

surface strain [18].

3.3. Microstructural observation

Microstructural images of the as-sintered surface of BZT-BCLT ceramics are illustrated in Fig. 3. All samples showed a dense microstructure with high relative densities (i.e., \geq 95% as listed in Table 1). Thus, the substitution of BCLT to BZT did not significantly affect the physical properties of this ceramic system. Fig. 4 shows the grain size distribution of all ceramics. As seen in the figure, the distribution of

grain size for all ceramics was quite wide, with grains varying in size from 2 to $12\,\mu m$. This result indicates that the increase in BCLT did not have a dominant effect on the grain size distribution of all ceramics. However, the effects of the increase in BCLT content on the microstructural evolution of these ceramics were noticeable. As the BCLT content increased, the number of small grains increased, particularly for the composition x=0.6. This led to a decrease in the average grain size of all ceramics (see the average grain size data in Table 1). The reduction in grain size is possibly due to an overall decrease in the diffusion rate during the initial sintering process. Generally, ions with a

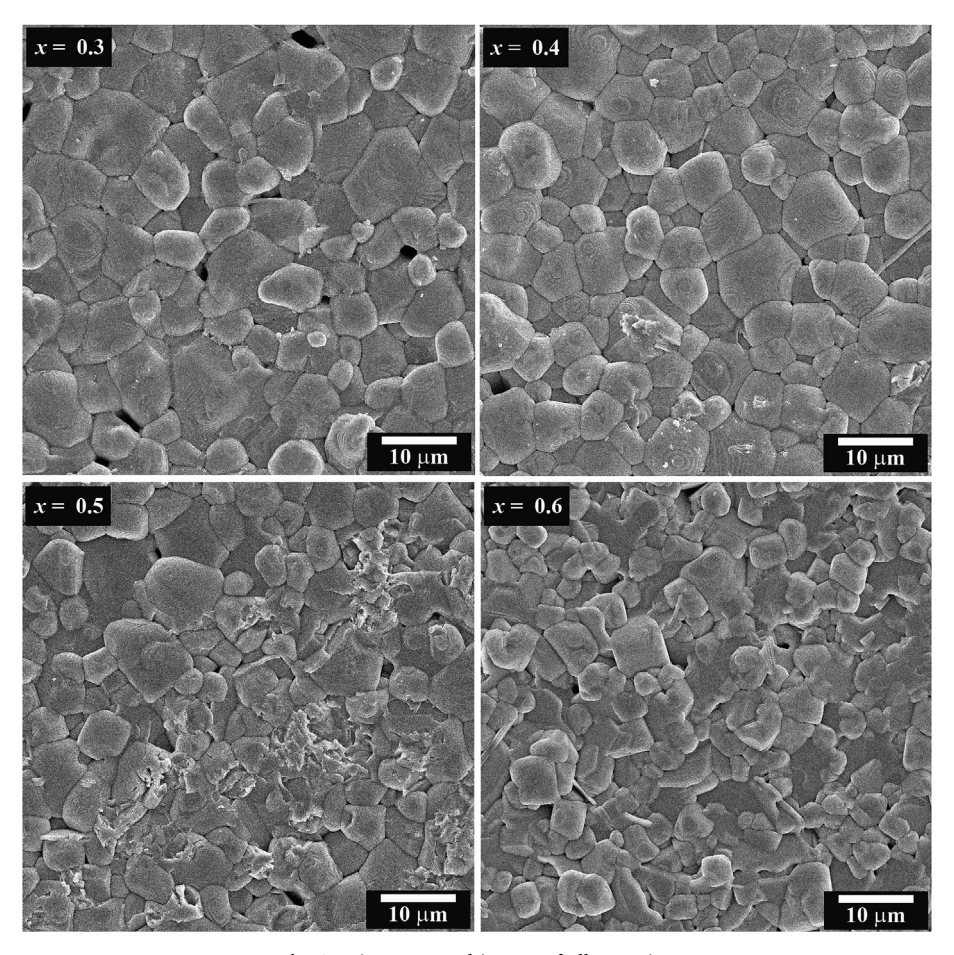


Fig. 3. Microstructural images of all ceramics.

Table 1
Density, grain size, and dielectric phase transition for all ceramics.

BCLT content	Bulk density (g/cm³)	Relative density (%)	Average grain size	T_{R-C}	T_{R-T}	T _{T-C}	Tetragonality
	(g/cili)	(70)	(µm)	(°C)	(°C)	(°C)	
0.3	5.96	98.43	6.51	65	_	_	_
0.4	5.86	97.89	6.24	-	45	80	1.0033
0.5	5.76	97.61	5.43	-	8	90	1.0040
0.6	5.67	98.68	4.54	-	-	100	1.0041

small diffusion coefficient (*D*) are the slowest-diffusing species. Hence, a material with a low *D* value should have decreased the sintering diffusion rate, leading to a reduction in grain growth. For the (1-*x*)BZT-(*x*)BCLT ceramic, La was likely the slowest-diffusing species because its diffusion coefficient ($D = 7.72 \times 10^{-20} \,\mathrm{m}^2/\mathrm{s}$ [23]) is smaller than those of Ba ($D = 5.4 \times 10^{-10} \,\mathrm{m}^2/\mathrm{s}$ [24]), Ca ($D = 5.2 \times 10^{-10} \,\mathrm{m}^2/\mathrm{s}$ [24]), Ti ($D = 3.4 \times 10^{-16} \,\mathrm{m}^2/\mathrm{s}$ [25]), Zr ($D = 1.3 \times 10^{-16} \,\mathrm{m}^2/\mathrm{s}$ [25]), and O ($D = 5.2 \times 10^{-10} \,\mathrm{m}^2/\mathrm{s}$ [26]). Thus, with an increase in BCLT concentration, the amount of the slowest-diffusing species, i.e., La ions, increased, resulting in grain growth reduction, which led to a decrease in the final grain size.

3.4. Relationship between dielectric properties and phase transition

Fig. 5 shows real (ϵ') and imaginary (ϵ'') parts of the relative permittivity as a function of temperature in the range from 25 °C to 200 °C and with frequencies ranging from 1 kHz to 100 kHz for all ceramics. The results indicated a sharp dielectric phase transition with increasing temperature. In addition to the sharp dielectric peak, the phase transition from the ferroelectric to cubic phase was observed at 65 °C, 80 °C,

90 °C, and 100 °C for the compositions x = 0.3, 0.4, 0.5, and 0.6, respectively. These phase transition temperatures were independent of the applied frequency, suggesting a normal ferroelectric behavior in these ceramics. Regarding the phase transition in these ceramics, it should be mentioned first that the 0.7BZT-0.3BCLT ceramic sample possessed a rhombohedral structure, as observed in its XRD pattern at room temperature (Fig. 1(c) and (d)). Thus, the phase transition at 65 °C should be a transformation from rhombohedral to cubic structure (T_R- $_{\rm C}$). On the contrary, (1-x)BZT-(x)BCLT compositions where $0.4 \le x \le 0.6$ indicated the presence of a tetragonal structure. Accoordingly, the phase transitions, observed at 80 °C for x = 0.4, at 90 °C for x = 0.5, and at 100 °C for x = 0.6, should correspond to the transformation from the tetragonal to cubic phase $(T_{T,C})$. The $T_{T,C}$ shifted to higher temperatures (i.e., from 80 °C to 100 °C) when the BCLT content increased. This was the fact that the phase transition temperatures of BZT and BCLT were -20 °C and 100 °C, respectively. Thus, when BCLT increased, the phase transition of BZT-BCLT system should increase. Besides, the increase in tetragonality of the ceramics listed in Table 1 could be the additional reason for the shift of T_{T-C} to higher temperatures. Since a result of the crystal structure with higher tetragonality, a higher temperature for the phase transformation from tetragonal to cubic structure would be required [14]. In addition to the shift in phase transition temperature, the results also suggest a change in dielectric permittivity at room temperature (ϵ'_r) and a maximum dielectric permittivity (ε'_{m}) at T_{R-C} for the composition x = 0.3 and at T_{T-C} for the others. This result will be discussed together with the grain size effect in the following section. With these dielectric results, interestingly, the sample with x = 0.4 showed a shoulder peak at 45 °C that was absent in the other ceramics. It is possible that this peak is related to the phase transformation from a rhombohedral to tetragonal structure (T_{R-T}). When considering the XRD results seen in Fig. 1(c) and (d), the ceramic

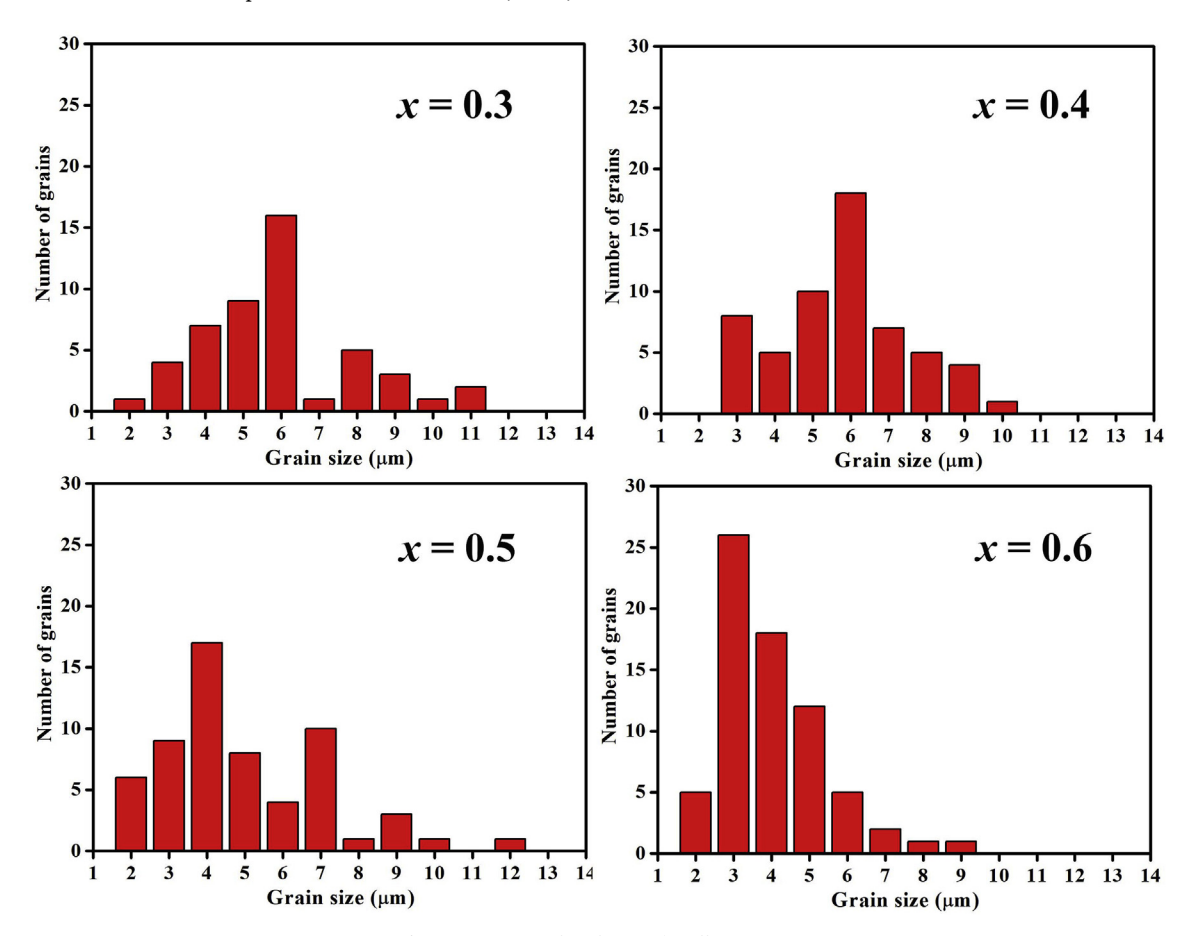


Fig. 4. Grain size distribution for all ceramics.

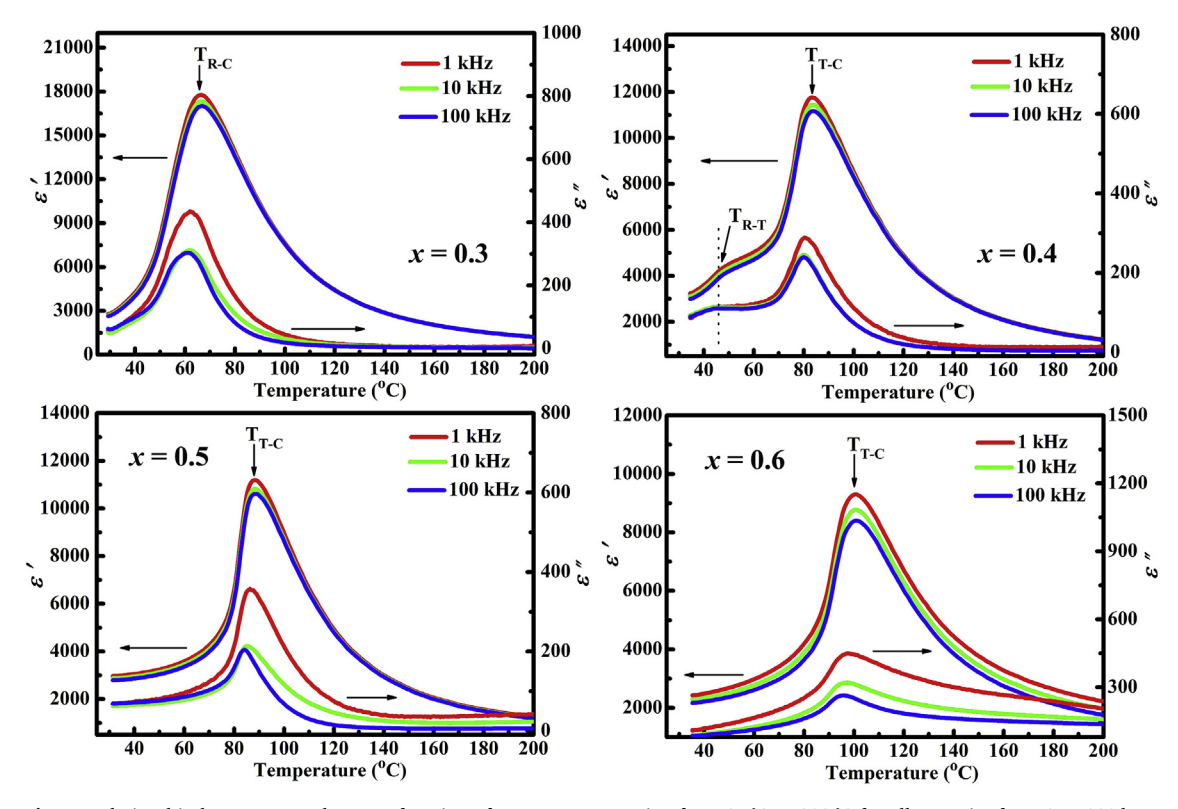


Fig. 5. Relationship between ε and ε as a function of temperature ranging from 25 °C to 200 °C for all ceramics from 1 to 100 kHz.

x=0.4 exhibited coexistence of the rhombohedral and tetragonal phases at room temperature. Thus, with increasing temperature for this composition, the rhombohedral phase was first transformed to a tetragonal structure, and the tetragonal phase was transformed to a cubic structure.

To further explain the phase transition temperature of the (1-x)BZT-(x)BCLT binary system, dielectric measurement in a temperature range from $-40\,^{\circ}\text{C}$ to 25 $^{\circ}\text{C}$ was carried out. The plots of ϵ' and ϵ'' as a function of temperature with measured frequencies from 1 kHz to 100 kHz for selected ceramics are illustrated in Fig. 6. For the compositions x = 0.3 and 0.6, the ceramics did not indicate an apparent change in this temperature range. This result could confirm that only T_{R-C} occurred for the composition x = 0.3 and T_{T-C} for the composition x = 0.6. Interestingly, the ceramic with x = 0.5 showed a shoulder peak at 8 °C. This peak is believed to be the phase transformation point from a rhombohedral to tetragonal structure (T_{R-T}) in this ceramic because its XRD results (Fig. 1(c) and (d)) clearly confirmed the existence of a single tetragonal structure at room temperatures (i.e., ~ 25 °C). The decrement of T_{R-T} from 45 °C to 8 °C at the composition x = 0.5 might be attributed to the decreasing trend of unit cell volume of rhombohedral phase as seen in Fig. 1(e). This result accompanied by the reduction of T_{R-T} to lower temperature when the unit cell volume of $0.5BaZr_{0.2}Ti_{0.8}O_3\text{-}0.5Ba_{0.7}Ca_{0.3}TiO_3 \ ceramic \ decreased \ \textbf{[2]}.$

3.5. P-E and S-E hysteresis loops for all ceramics

The ferroelectric properties of the (1-x)BZT-(x)BCLT system with $0.3 \le x \le 0.6$ were determined using the relationship between polarisation and an applied external electric field (*P-E* hysteresis loop), as shown in Fig. 7. Fig. 8 presents the electromechanical response of all ceramics, which was determined by a bipolar strain curve upon the applied external electric field (*S-E* or butterfly hysteresis loop). As seen in both figures, normal *P-E* and *S-E* hysteresis loops were observed for all ceramics. This result indicates that this ceramic is a normal ferroelectric material system.

3.6. Relationships among microstructure, crystal structure, and electrical properties

3.6.1. Effects of average grain size on dielectric properties

Fig. 9(a) summarises the influence of grain size on dielectric properties, including the dielectric permittivity at room temperature (ε_r) and maximum dielectric permittivity (ε_m), for these ceramics. As seen in the figure, both dielectric values decreased with increasing BCLT concentration. The change in these values was accompanied by a decreasing average grain size for (1-x)BZT-(x)BCLT ceramics. Thus, the reduction in grain size should play an important role in the decrease of the dielectric properties of this binary system. In general, the microstructure with smaller grains has larger grain boundaries, which slow domain wall movement, leading to a decrease in ε_r , and ε_m [27].

3.6.2. Effects of crystal structure and average grain size on ferroelectric properties

The *P-E* hysteresis loops of all ceramics are shown in Fig. 7. A slight offset of the P-E hysteresis loop could be observed in all ceramics. This was because of the contribution of their electrical conduction [28] and the presence of trapped space charges at the electrode-ferroelectric interface [29]. Thus, the ferroelectric parameters, including remanent polarisation (P_r) , saturated polarisation (P_s) , and coercive field (E_s) , at the positive and negative electric fields were therefore extracted from their *P-E* hysteresis loop. The extracted parameters are listed in Table 2. From the table, there was no significant trend from the data extracted from the positive and negative electric fields. Thus, the average ferroelectric parameters (listed in Table 2 and Fig. 9(b)) could be used to explain the ferroelectric properties of these ceramics. From the average values, the P_r factors of BCLT compositions where $0.3 \le x \le 0.4$ did not differ significantly. Interestingly, the sample at 0.5BCLT concentration showed the maximum P_r value (i.e., $\sim 7.2 \,\mu\text{C/cm}^2$) and the value decreased with increasing addition of BCLT. The presence of a single tetragonal phase induced an increase in $P_{\rm r}$ for the ceramics at compositions $x \ge 0.5$ because spontaneous polarisation was aligned with the

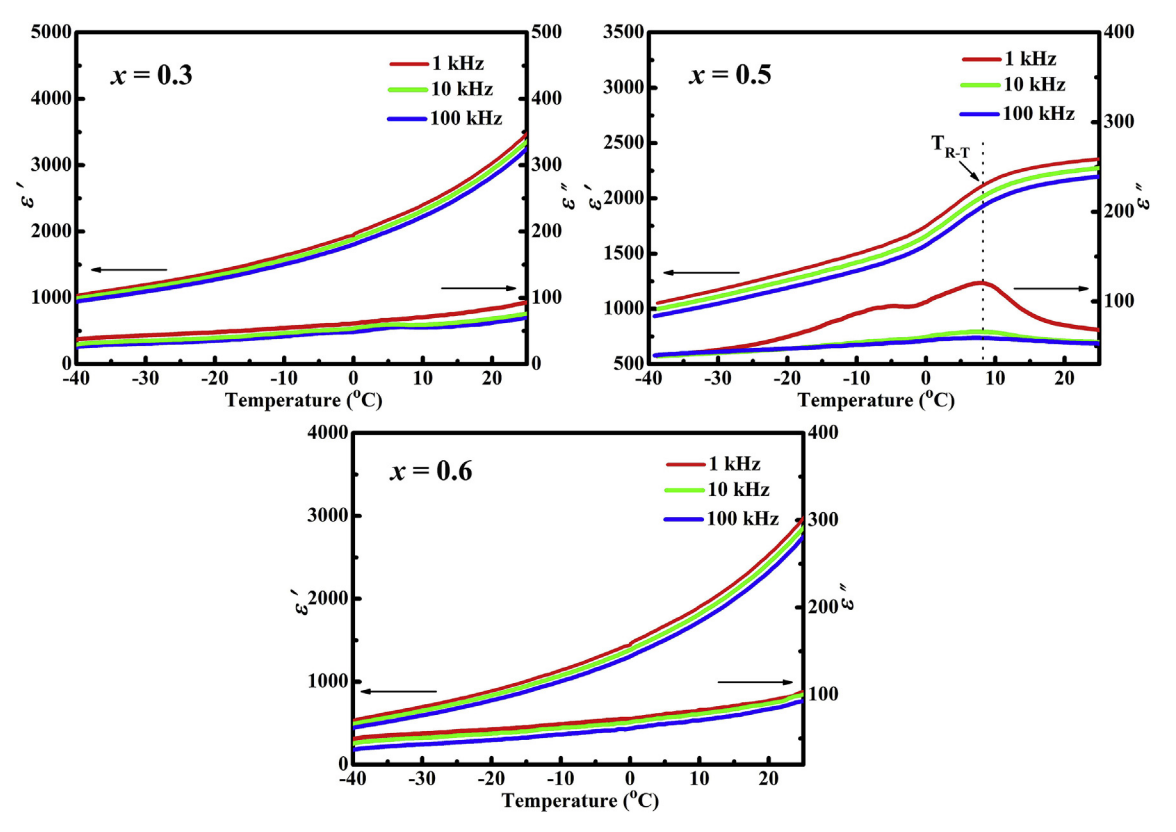


Fig. 6. Relationship between ε and ε as a function of temperature ranging from - 40 °C to 25 °C for selected ceramics from 1 to 100 kHz.

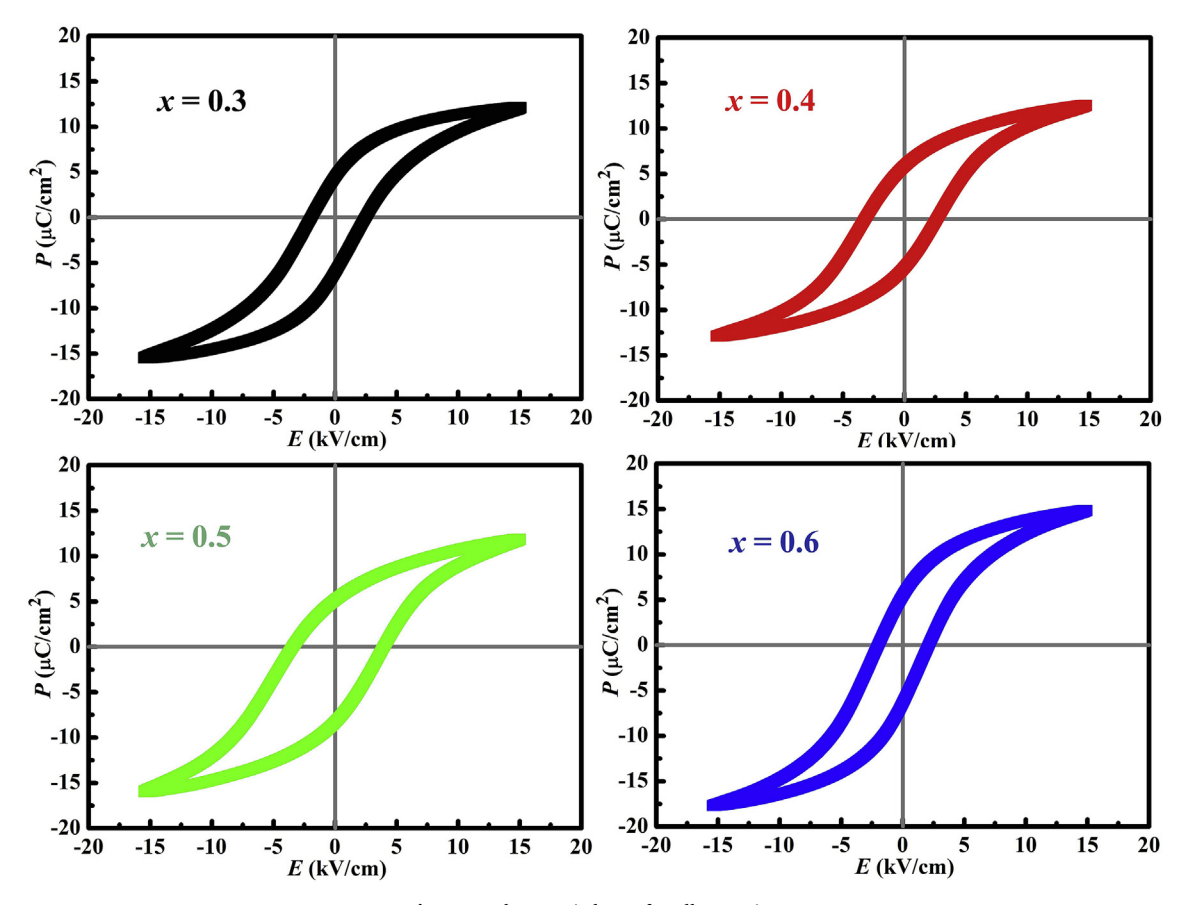


Fig. 7. P-E hysteresis loops for all ceramics.

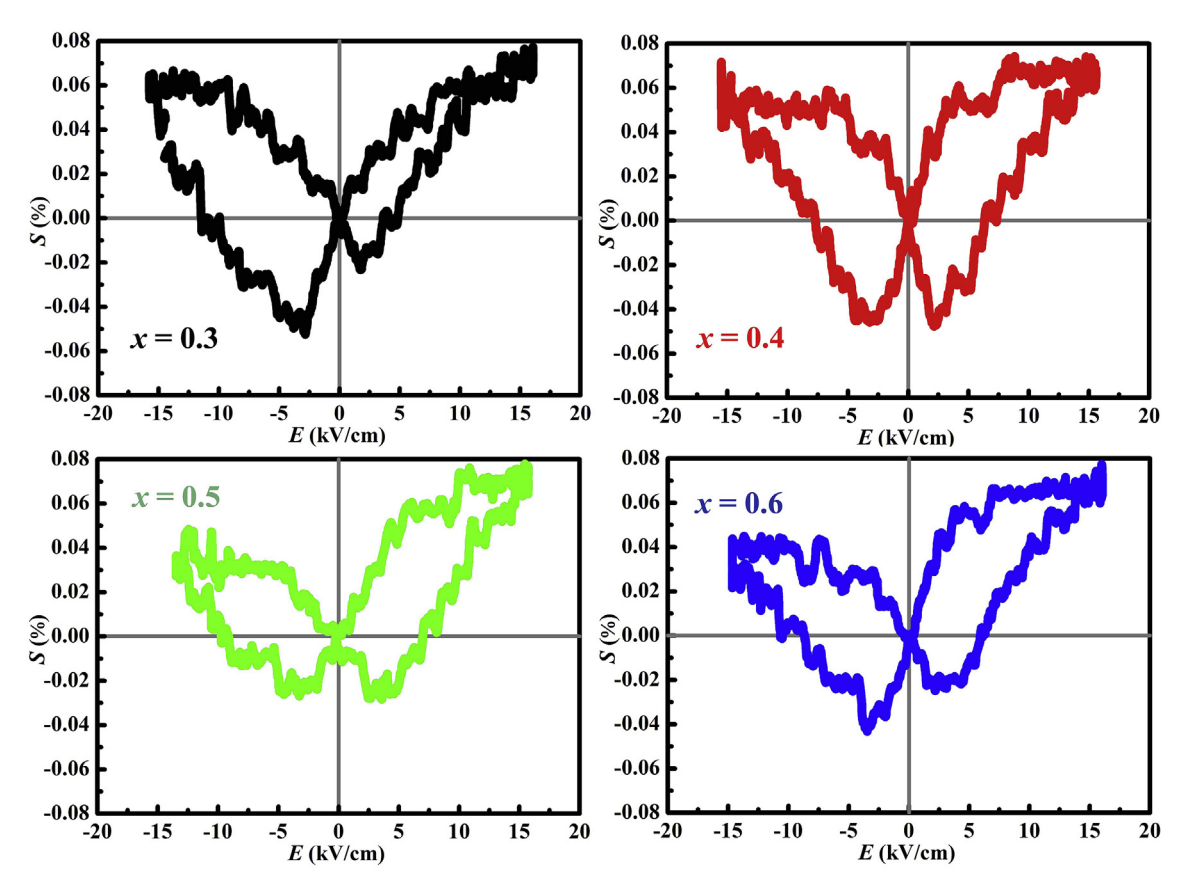


Fig. 8. S-E hysteresis loops for all ceramics.

[001] direction in the tetragonal phase. Therefore, the polarisation could lead to easier arrangement of the rhombohedral phase, which possessed [111] direction [29]. Regarding $E_{\rm c}$, the value increased with increasing BCLT content up to x=0.5. This could be attributed to the presence of a tetragonal phase. Strain could be induced during domain rotation in the tetragonal phase, which obstructs the switching of the domain. Meanwhile, the domain rotation in the rhombohedral phase was without induced strain [29]. Thus, the $E_{\rm c}$ value for the composition x=0.5 was higher than it was for $x\leq0.4$. However, the reduction of $P_{\rm r}$ and $E_{\rm c}$ was observed in x=0.6, even though the ceramic had a single tetragonal phase. The contribution of small grain size could be the additional reason for this decrease, as the ferroelectric domain would stabilize in large grains more readily than it would in smaller grains [30].

3.6.3. Effects of crystal structure and average grain size on small-signal piezoelectric properties

The small-signal piezoelectric properties were measured by application of pressure on the poled sample, via which the piezoelectric coefficient (d_{33}) and electromechanical coupling factor (k_p) were determined. From section 3.6.2, the presence of a tetragonal phase and decrease in the average grain size affected P_r for the ceramics. Thus, to explain the effects of crystal structure and grain size, the relationship between $P_{\rm r}$, d_{33} , and $k_{\rm p}$ as a function of BCLT content is plotted in Fig. 9(b). Regarding P_r , for BCLT compositions where $0.3 \le x \le 0.4$, the ferroelectric factors did not differ significantly. Interestingly, the sample with 0.5BCLT concentration showed the maximum P_r value because of the presence of a tetragonal phase, which decreased at 0.6BCLT concentration because of the reduction in the average grain size. When compared with piezoelectric properties, the trend for the d_{33} and $k_{\rm p}$ values of these ceramics seemed to accompany a change in their $P_{\rm r}$ values. Thus, the small-signal piezoelectric response could be attributed to P_r . It is worth mentioning first that the d_{33} and k_p factors are

related to a reversible contribution, i.e., rearrangement of spontaneous polarisation ($P_{\rm sp}$) [8]. Before the poling process, $P_{\rm sp}$ within the material is arranged randomly. When an external electric field is applied, $P_{\rm sp}$ will re-arrange in a direction similar to that of the applied electric field. After removing the external electric field, $P_{\rm sp}$ could either be maintained in the poled direction or revert back to the initial direction. A material with large $P_{\rm sp}$ in the poled direction shows better d_{33} and $k_{\rm p}$ factors. With ferroelectric measurement, $P_{\rm r}$ can indicate the degree of rearrangement of $P_{\rm sp}$ after removing the external electric field. Thus, in these ceramics, the sample with 0.5BCLT concentration possessed the maximum $P_{\rm r}$; therefore, it exhibited the maximum d_{33} and $k_{\rm p}$ factors. This result is in agreement with several previous reports [31,32].

3.6.4. Effects of average grain size on large-signal piezoelectric properties

The decrease in grain size affected the strain response at high electric field for these ceramics. The maximum strain (S_{max}) and the ratio between the maximum strain and electric field (d_{33}^*) can be extracted from the S-E hysteresis curve (Fig. 8). Both factors are widely utilized to study this property. Fig. 9(c) and (d) show respectively S_{max} and d_{33}^* values for these ceramics in the direction of a positive and negative electric field. In the positive direction, the results did not show any significant change in S_{max} and d_{33}^* . However, a decreasing trend for the S_{max} and d_{33}^* factors with increasing BCLT content was observed after the electric field was switched to the negative direction. This seemed to be associated with the decrease in the average grain size for these ceramics (Fig. 9(a)). It is well known that the increase in the strain of piezoelectric materials at high electric field is primarily due to irreversible contributions, i.e., the mobility of the domain wall [8]. Thus, a material with high domain wall motion should have better S_{max} and d_{33}^* factors. With these ceramics, the average grain size decreased with increasing BCLT content. The reduction in grain size led to larger grain boundaries. This result could prohibit movement of the domain wall and thus effectively reduce $S_{\rm max}$ and d_{33}^* as the BCLT content is

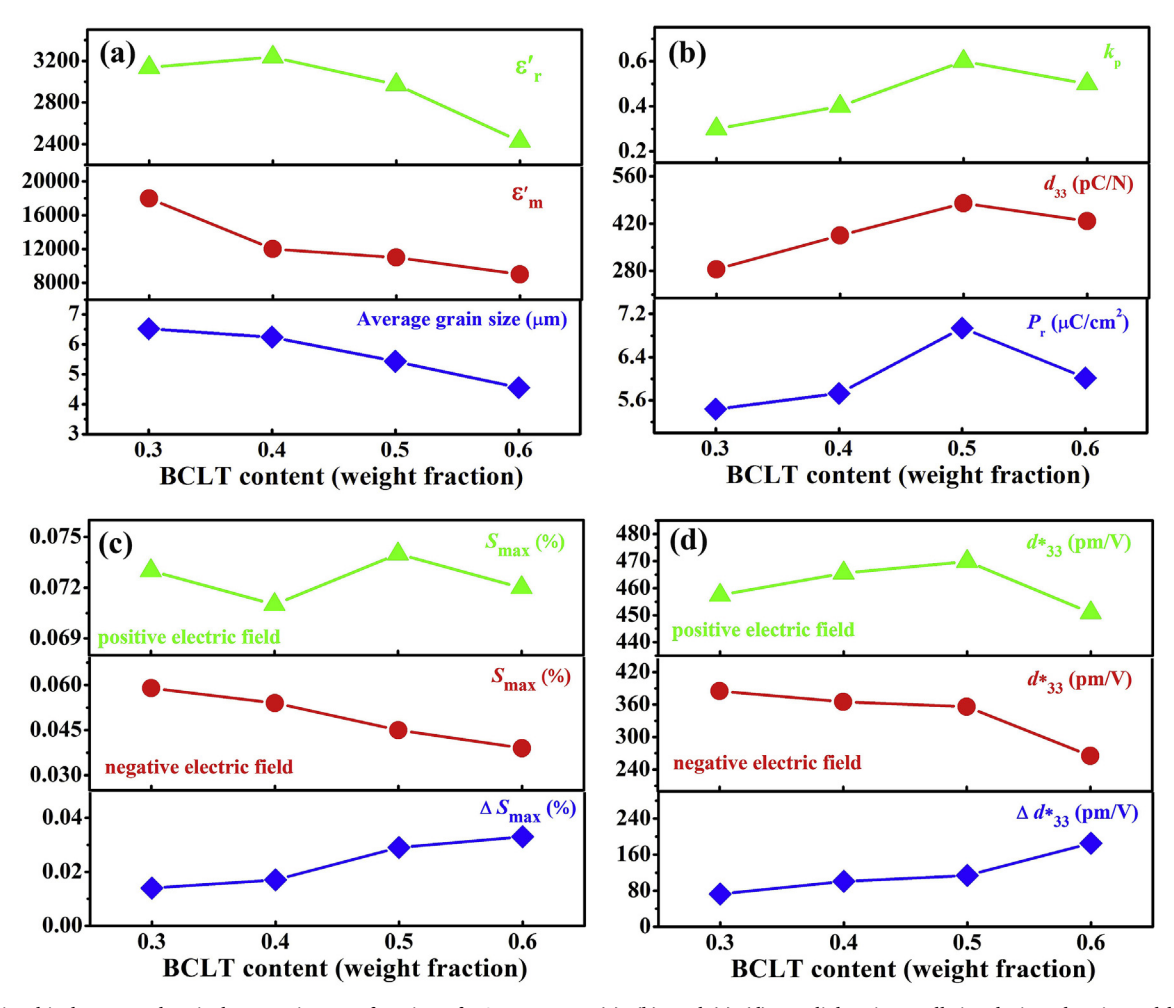


Fig. 9. Relationship between electrical properties as a function of BCLT content. (a), (b), and (c)–(d) are dielectric, small-signal piezoelectric, and large electromechanical response, respectively.

increased. To further explain this phenomenon, the differences in these values in the positive and negative directions were therefore calculated and denoted $\Delta S_{\rm max}$ and Δd_{33}^* in Fig. 9(c) and (d), respectively. $\Delta S_{\rm max}$ and Δd_{33}^* indicate the prohibition of domain wall movement during switching of the applied electric field. In the figure, $\Delta S_{\rm max}$ and Δd_{33}^* increased with increasing BCLT content. This result confirmed the further contribution of grain boundaries to domain wall switching in these ceramics.

3.7. Relationship between phase region and (1-x)BZT-(x)BCLT content

Using these results, we found that the dielectric, ferroelectric, and piezoelectric properties of these ceramics were dependent on the BCLT content. Hence, a new phase diagram for the (1-x)BZT-(x)BCLT system can be illustrated, as shown in Fig. 10. The compositions x = 0.3 and 0.5 showed the maximum dielectric and piezoelectric properties, respectively. In addition to the properties of the (1-x)BZT-(x)BCLT binary

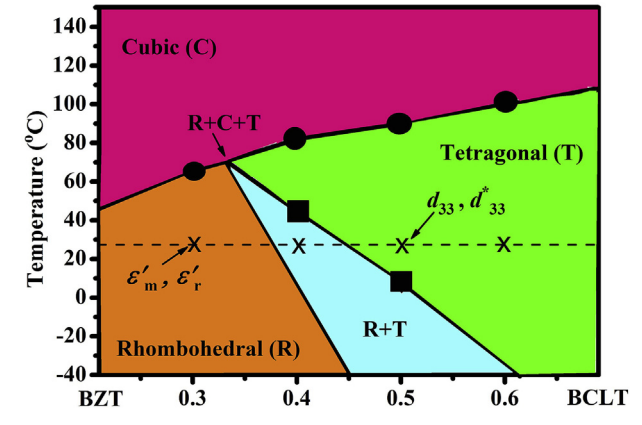


Fig. 10. Phase diagram for (1-x)BZT-(x)BCLT ceramics, where x = 0.3 to 0.6.

Table 2Ferroelectric parameters for all ceramics.

BCLT content	Positive elect	Positive electric field			Negative electric field			Average values		
	$P_{\rm r~(\mu C/cm)}^{3}$	$P_{\rm s~(\mu C/cm)}^{3}$	E _{c (kV/cm)}	$P_{\rm r~(\mu C/cm)}^{3}$	P _{s (µC/cm)} ³	E _{c (kV/cm)}	$P_{\rm r} {}_{(\mu {\rm C/cm})}^{3}$	P _{s (µC/cm)} ³	E _{c (kV/cm)}	
0.3	4.52	15.44	2.45	6.36	15.37	1.92	5.44	15.41	2.18	
0.4	5.97	12.58	2.61	5.49	12.91	3.15	5.73	12.74	2.88	
0.5	5.76	11.85	3.84	8.69	15.87	3.37	7.22	13.86	3.61	
0.6	5.45	14.90	2.13	6.58	17.69	1.98	6.02	16.29	2.05	

system, a triple phase point (TPP), where rhombohedral, cubic, and tetragonal phases exist together, can be estimated. The illustrated phase diagram implies that the TPP point for this binary system can be found at a composition of x=0.33 at 70 °C. However, further investigation is needed to support this hypothesis. The results here suggest that the dielectric, ferroelectric, and piezoelectric properties of the (1-x)BZT-(x) BCLT binary system are dependent on the crystal structure and microstructure, which can be tuned using the BCLT concentration.

4. Conclusions

(1-x)BZT-(x)BCLT ceramics, where x=0.3, 0.4, 0.5, and 0.6, were fabricated using conventional solid-state sintering. Depending on BCLT content, the system showed three phase regions, including a single rhombohedral phase, a binary rhombohedral and tetragonal phase, and a single tetragonal structure. With increasing BCLT content, the grain size decreased and a single tetragonal phase existed, which significantly affected the dielectric, ferroelectric, and piezoelectric properties of these ceramics. The addition of BCLT at x=0.3 and 0.5 promoted the maximum dielectric properties and piezoelectric properties, respectively. The results here suggest a new phase diagram for the (1-x)BZT-(x)BCLT system, which can be tuned by the BCLT concentration and may be utilized as an alternative material in dielectric, ferroelectric, and piezoelectric devices.

Acknowledgments

This research was funded by the Thailand Research Fund (TRF) and Office of the Higher Education Commission (OHEC), Ministry of Education through the TRF-OHEC Grant for New Researcher. Contract no. MRG6180109. P. Jaiban also would like to thank partial funding support from King Mongkut's University of Technology North Bangkok. Contract no. KMUTNB-62-KNOW-04. A. Watcharapasorn would like to acknowledge partial funding support from Chiang Mai University.

References

- T. Takenaka, K.I. Maruyama, K. Sakata, (Bi_{1/2}Na_{1/2})TiO₃-BaTiO₃ systems for lead-free piezoelectric ceramics, Jpn. J. Appl. Phys. 30 (1991) 2236–2239 https://doi.org/10.1143/JJAP.30.2236.
- [2] A.B. Haugen, J.S. Forrester, D. Damjanovic, B. Li, K.J. Bowman, J.L. Jones, Structure and phase transitions in 0.5(Ba0.7Ca0.3TiO3)-0.5(BaZr0.2Ti0.8O3) from -100 °C to 150 °C, J. Appl. Phys. 113 (2013) 014103https://dx.doi.org/10.1063/1. 4772741
- [3] P. Wannasut, P. Jaita, S. Jiansirisomboon, A. Watcharapasorn, Piezoelectric and ferroelectric properties of lead free Bi_{0.5}(Na_{0.80}K_{0.20})_{0.5}TiO₃-(Ba_{0.98}Nd_{0.20})TiO₃ binary system, Integr. Ferroelectr. 177 (2017) 10–16 https://doi.org/10.1080/ 10584587.2017.1284536.
- [4] W. Liu, X. Ren, Large piezoelectric effect in Pb-free ceramics, Phys. Rev. Lett. 103 (2009) 257602 https://doi.org/10.1103/PhysRevLett.103.257602.
- [5] Y. Zhang, H. Sun, W. Chen, A brief review of Ba(Ti_{0.8}Zr_{0.2})O₃-(Ba_{0.7}Ca_{0.3})TiO₃ based lead-free piezoelectric ceramics: past, present and future perspectives, J. Phys. Chem. Solids 114 (2018) 207–219 https://doi.org/10.1016/j.jpcs.2017.10. 041
- [6] D.S. Keeble, F. Benabdallah, P.A. Thomas, M. Maglione, J. Kreisel, Revised structure phase diagram of (Ba_{0.7}Ca_{0.3}TiO₃)-(BaZr_{0.2}Ti_{0.8}O₃), Appl. Phys. Lett. 102 (2013) 092903https://doi.org/10.1063/1.4793400.
- [7] J. Gao, X. Hu, L. Zhang, F. Li, L. Zhang, Y. Wang, Y. Hao, L. Zhong, X. Ren, Major contributor to the large piezoelectric response in (1-x)Ba(Zr_{0.2}Ti_{0.8})O₃-x (Ba_{0.7}Ca_{0.3})TiO₃ ceramics: domain wall motion, Appl. Phys. Lett. 104 (2014) 252909 https://doi.org/10.1063/1.48856751.
- [8] M. Acosta, N. Novak, W. Jo, J. Rödel, Relationship between electromechanical properties and phase diagram in the Ba(Zr_{0.2}Ti_{0.8})O₃-x(Ba_{0.7}Ca_{0.3})TiO₃ lead-free piezoceramic, Acta Mater. 80 (2014) 48–55 https://doi.org/10.1016/j.actamat. 2014.07.058.

- [9] S. Mahajan, D. Haridas, K. Sreenivas, O.P. Thakur, C. Prakash, Enhancement in electro-strain behavior by La³⁺ substitution in lead free BaZr_{0.05}Ti_{0.95}O₃ ceramics, Mater. Lett. 97 (2013) 40–43 https://doi.org/10.1016/j.matlet.2013.01.057.
- [10] M.L. Cheah, K.A. Razak, C.Y. Ng, Properties of lanthanum-doped bismuth sodium titanate (Bi_{0.5}Na_{0.5}TiO₃) prepared by soft combustion technique, Adv. Mater. Res. 858 (2014) 141–146 https://doi.org/10.4028/www.scientific.net/AMR.858.141.
- [11] R. Kumar, K. Asokan, S. Patnaik, B. Birajdar, Evolution of relaxor properties in lanthanum (La) doped barium zirconate titanate, Ferroelectrics 517 (2017) 8–13 https://doi.org/10.1080/00150193.2017.1369820.
- [12] A. Mahmood, E. Mensur, A. Abdul, Naeem, Y. Iqbal, A. Ullah, S. Alkoy, Effect of La substitution on the microstructure and dielectric properties of the sol-gel derived BaZr_{0.2}Ti_{0.8}O₃ thin films, Thin Solid Films 611 (2016) 68–73 https://doi.org/10. 1016/i.tsf.2016.05.008.
- [13] P. Jaiban, O. Namsar, S. Jiansirisomboon, A. Watcharapasorn, R. Yimnirun, Electrical properties of La-doped Ba_{0.7}Ca_{0.3}TiO₃ lead-free ceramics, Ferroelectrics 487 (2015) 86–93 https://doi.org/10.1080/00150193.2015.1070642.
- [14] P. Jaiban, S. Suwanwong, O. Namsar, A. Watcharapasorn, W. Meevasana, Simultaneous tuning of the dielectric property and photo-induced conductivity in ferroelectric Ba_{0.7}Ca_{0.3}TiO₃ via La doping, Mater. Lett. 147 (2015) 29–33 https://doi.org/10.1016/j.matlet.2015.01.114.
- [15] D. Gao, K.W. Kwok, D. Lin, H.L.W. Chan, Microstructure and electrical properties of La-modified K_{0.5}Na_{0.5}NbO₃ lead-free piezoelectric ceramics, J. Phys. D. 42 (2009) 035411https://doi.org/10.1088/0022-3727/42/3/035411.
- [16] B.H. Toby, R.B.V. Dreele, GSAS-II: the genesis of a modern open-source all purpose crystallography software package, J. Appl. Crystallogr. 46 (2013) 544–549.
- [17] R.D. Shannon, Revised effective ionic radii and systematic studies of interatomic distance in halides and chalcogenides, Accta. Cryst. A32 (1976) 751–767 https:// doi.org/10.1107/S0567739476001551.
- [18] M.F. Toomey, K. Gao, G.P. Medis, E.B. Slamovich, J.A. Howarter, Hydrothermal synthesis and processing of barium titanate nanoparticles embedded in polymer films, ACS Appl. Mater. Interfaces 7 (2015) 28640–28646 https://doi.org/10.1021/ acsami.5b10282.
- [19] M.D.C. Blanco López, G. Fourlaris, B. Rand, F.L. Riley, Characterization of barium titanate powders: barium carbonate identification, J. Am. Ceram. Soc. 82 (1999) 1777–1786 https://doi.org/10.1111/j.1151-2916.1999.tb01999.x.
- [20] H. Zou, D. Peng, G. Wu, X. Wang, D. Bao, J. Li, Y. Li, X. Yao, Polarization-induced enhancment of photoluminescence in Pr³⁺ doped ferroelectric diphase BaTiO₃-CaTiO₃ ceramics, J. Appl. Phys. 114 (2013) 73103 https://doi.org/10.1063/1. 4818793.
- [21] J.F. Moulder, W.F. Stickle, P.E. Sobol, K.D. Bomben, Handbook of X-Ray Photoelectorn Spectroscopy vol. 8, Physical Electonics, Eden Prairie, MN, 1995.
- [22] I. Bespalov, M. Datler, S. Buhr, W. Drachsel, G. Ruppreshter, Y. Suchorski, Initial stages of oxide formation on the Zr surface at low oxygen pressure: an in situ FIM and XPS study, Ultamicroscopy 159 (Pt 2) (2015) 147–151 https://doi.org/10. 1016/j.ultramic.2015.02.016.
- [23] W. Jinshu, Z. Meiling, N. Zuoren, Z. Jiuxing, Z. Tieyong, W. Yiman, A study of diffusion behavior of element lanthanum and oxygen in Mo-La₂O₃ cathode, J. Alloy. Comp. 311 (2000) 82–85.
- [24] E. Nasi, D. Tillotson, The rate of diffusion of Ca²⁺ and Ba²⁺ in a nerve cell body, Biophys. J. Biophys. Soc. 47 (1985) 735–738.
- [25] D.L. Zhang, C.X. Qiu, W.J. Du, W.H. Wong, E.Y.B. Pun, Zr⁴⁺/Ti⁴⁺ codiffusion characteristics in lithium niobate, J. Am. Ceram. Soc. 98 (2015) 567–573.
- [26] P.D. Beattie, V.I. Basura, S. Holdcroft, Temperature and pressure dependence of O₂ reduction at Pt vertical bar Nafion((R)) 117 and Pt vertical bar BAM((R)) 407 interfaces. J. Electroanal. Chem. 468 (1999) 180–192.
- [27] P. Jaiban, A. Watcharapasorn, R. Yimnirun, R. Guo, A.S. Bhalla, Effects of donor and acceptor doping on dielectric and ferroelectric properties of Ba_{0.7}Ca_{0.3}TiO₃ lead-free ceramics, J. Alloy. Comp. 695 (2017) 1329–1335 https://doi.org/10. 1016/j.jallcom.2016.10.274.
- [28] L. Zheng, C. Lin, W.P. Xu, M. Okuyama, Vertical drift of P-E hysteresis loop in asymmetric ferroelectric capacitors, J. Appl. Phys. 79 (1996) 8634 https://doi.org/ 10.1063/1.362485.
- [29] M. Khodaei, D. Seol, S.A.S. Ebrahimi, Y.J. Park, H. Seo, Y. Kim, S. Baik, Ferroelectric and piezoelectric behavior of (111)-oriented Pb(Zr_xTi_{1-x})O₃ thin films on cobalt ferrite nano-seed layered Pt(111)/Si substrate, J. Mater. Sci. Mater. Electron. 25 (2014) 1696–1702 https://doi.org/10.1007/s10854-014-1785-6.
- [30] N. Thongmee, R. Sumang, S. Pojprapai, T. Klaytae, Influence of BLT content on phase structure and electrical properties of (1-x)BT-(x)BLT ceramic, J. Metal Mater. Miner. 28 (2018) 109–115.
- [31] P. Jaiban, A. Watcharapasorn, Effects of Mg doping on electrical properties of Ba_{0.7}Ca_{0.3}TiO₃ ceramics, Mater. Today Comm. 11 (2017) 184–190 https://doi.org/ 10.1016/j.mtcomm.2017.05.001.
- [32] P. Jaiban, A. Watcharapasorn, R. Yimnirun, R. Guo, A.S. Bhalla, Dielectric, ferro-electric and piezoelectric properties of (Ba_{0.7}Ca_{0.3})Ti_{1.x}Cu_xO_{3.x} ceramics, J. Alloy. Comp. 759 (2018) 120–127 https://doi.org/10.1016/j.jallcom.2018.05.093.

ELSEVIER

Contents lists available at ScienceDirect

Materials Letters

journal homepage: www.elsevier.com/locate/mlblue



Dielectric response on ultraviolet light irradiation of Ba_{0.85}Ca_{0.15}Zr_{0.1}Ti_{0.9}O₃ based ceramics



Panupong Jaiban ^{a,*}, Maneeporn Tongtham ^a, Pimpilai Wannasut ^b, Anucha Watcharapasorn ^{b,c}

- ^a Faculty of Science, Energy and Environment, King Mongkut's University of Technology North Bangkok, Rayong Campus, Rayong 21120, Thailand
- ^b Department of Physics and Materials Science, Faculty of Science, Chiang Mai University, Chiang Mai 50200, Thailand
- ^c Center of Excellence in Materials Science and Technology, Materials Science Research Center, Faculty of Science, Chiang Mai University, Chiang Mai 50200, Thailand

ARTICLE INFO

Article history:
Received 12 December 2018
Received in revised form 23 January 2019
Accepted 4 February 2019
Available online 12 February 2019

Keywords:
Photo-induced dielectrics
Electrical properties
Defect dipole

ABSTRACT

 $Ba_{0.85}Ca_{0.15}Zr_{0.1}Ti_{0.9}O_3$ -based ceramics with doping of $Ca_3Co_4O_9$, $CaMn_{0.98}Nb_{0.02}O_3$, and $Zn_{0.98}Al_{0.02}O$ were fabricated. CaO and $CaCO_3$ secondary phase were observed in all doped ceramics. These phases caused vacancies of Ca ions, which became associated with oxygen vacancies induced by ultraviolet light, leading to the formation of a defect dipole. The defect dipoles enhanced the photo-induced dielectric properties. The maximum enhancement was about 60% with $Ca_3Co_4O_9$ doping while other ceramics did not show significant change. The results here suggested that the ultraviolet light-induced dielectric properties of $Ba_{0.85}Ca_{0.15}Zr_{0.1}Ti_{0.9}O_3$ ceramic may be largely tunable by $Ca_3Co_4O_9$ addition and could be an alternative material for light sensors.

© 2019 Elsevier B.V. All rights reserved.

1. Introduction

Ba_{0.85}Ca_{0.15}Zr_{0.1}Ti_{0.9}O₃ (BCZT) lead-free ceramic has shown large piezoelectricity [1], which can be compared with a commercial lead zirconate titanate (PZT). This makes BCZT a promising lead-free piezoelectric material to replace PZT for application in several electronic devices such as sensor, actuator, and a capacitor [2]. Unfortunately, the optical property of BCZT is focused scarcely.

Recently, SrTiO₃ (STO)-based ceramic has promoted the ultraviolet (UV) light-induced dielectric enhancement [3]. STO is thermoelectric material, which a few variations in charge carrier and another defect, resulting to its electrical and thermoelectric properties. From the case of STO, other well-known thermoelectric materials such as Ca₃Co₄O₉ (CCO), CaMn_{0.98}Nb_{0.02}O₃ (CMNO), and Zn_{0.98}Al_{0.02}O (ZAO), therefore, are hypothesized to respond the stimulus of UV light. However, it is quite difficult to measure the dielectric properties of these compounds through the pure sample due to their high electrical conductivity. Thus, it may be possible to dope these materials in other ceramics to seek UV light-induced dielectric properties. When regarding together with BCZT, it is found that its dielectric properties under UV light have not been reported yet. Hence, we are, therefore, interested in dope CCO, CMNO, and ZAO into BCZT. In this work, BCZT ceramics with

doping of CCO, CMNO, and ZAO were fabricated. A role of a defect dipole on UV light-induced dielectric properties was discussed in detail.

2. Material and methods

The starting materials were BaCO₃ (99.95%), CaCO₃ (99.95%), ZrO_2 (99.9%), TiO_2 (99.9%), Co_3O_4 (99.95%), MnO (99.99%), Nb_2O_5 (99.99%), ZnO (99.99%), and Al_2O_3 (99.9%). The oxide mixtures were calcined at 1100 °C for 3 h for BCZT, 750 °C for 24 h for CCO, and 900 °C for 6 h for CMNO. For ZAO, the powder was weighed and mixed for 6 hrs due to the compound did not need the calcination process. After calcination, (1-x)BCZT-(x)CCO(BCZT-CCO), (1-x)BCZT-(x)CMNO(BCZT-CMNO), and (1-x)BCZT-(x)ZAO(BCZT-ZAO) powders where x=0 and 1 wt% of dopants were mixed in ethanol for 6 h. After drying, the pellets were sintered at 1350 °C for 4 h.

Phase characteristic was studied by an X-ray diffractometer (XRD). The local structure was analyzed by Synchrotron X-ray Absorption Spectroscopy (XAS) at the BL-5.2 of the Siam Photon Laboratory, Synchrotron Light Research Institute (SLRI), Thailand. A scanning electron microscopy (SEM) was used to observe microstructure. For dielectric properties under UV light, the sample was connected by Cu back electrode while the front electrode was made of transparent and conductive indium tin oxide which was mechanically compressed against the sample layer (see in Fig. 2).

^{*} Corresponding author. E-mail address: p.jaiban@gmail.com (P. Jaiban).

The samples were exposed to UV light from 405 nm laser through the front electrode. LCR meter was used to measure the dielectric properties.

3. Results and discussion

Fig. 1(a) shows XRD patterns of all ceramics. The result indicates a structure without a secondary phase of BCZT. Meanwhile, CaO and CaCO₃ exist in doped ceramics. The presence of both phases reflects the deficient content of Ca ions within the doped samples. Besides CaO and CaCO₃, a small intensity of CCO and ZnO peaks presents in BCZT-CCO and BCZT-ZAO, respectively. XRD patterns ($44.5^{\circ}-46^{\circ}$) are plotted in Fig. 1(b). BCZT shows the splitting peaks of (002) and (200). Interestingly, both peaks become overlap when BCZT are doped. The possible reason is a substitution of dopant in perovskite lattice. In general, the ions having a similar ionic radius size can substitute in the crystal structure, which leads to the deformation of the lattice. With these ceramics, Ba²⁺ (1.61 Å), Ca²⁺ (1.34 Å), Zr⁴⁺ (1.72 Å), and Ti⁴⁺ (1.84 Å) host ions can be substituted by Co²⁺ (1.84 Å), Mn²⁺ (1.84 Å), and Zn²⁺ (1.84 Å) dopants [4].

Fig. 1(c) presents Ba-L₃ XAS spectra and BaCO₃ standard reference. The absorption peak at $E_o \sim 5251 \, \text{eV}$ can be noticeable in all samples. This peak relates to a resonant excitation from Ba $2p_{3/2}$ to Ba 5d unoccupied state, revealing Ba²⁺ in all ceramics. Interestingly, the width of the shoulder of E_0 peak is different obviously. It should mention first that the width of the E_0 peak indicates the average Ba-O interatomic distance [5]. The broad shoulder of E_0 peak suggests the shorter average length of Ba and O atoms within the structure. Fig. 1(d) shows XAS spectra from 5243 to 5262 eV. BCZT shows the broad shoulder and small peak (i.e., peak A), suggesting more covalent bond in perovskite structure. Upon the doping, the different width of the shoulder is observed apparently for each dopant. This result reflects the deformed crystal structure in doped BCZT, which is in agreement with their XRD patterns. Fig. 1(e) shows SEM images of all ceramics. The average grain sizes of BCZT, BCZT-CCO, BCZT-CMNO, and BCZT-ZAO are about 6.22, 1.35, 3.69, and 5.47 µm, respectively.

The capacitance and dielectric loss under UV light at different frequencies of all ceramics are shown in Fig. 2. The dielectric

properties of BCZT do not change upon UV light, and the applied frequencies do not affect its UV light response. Interestingly, when the UV light is incident on BCZT-CCO ceramic at 1 kHz, the capacitance gradually increases from 415 pF to 435 pF. The maximum relative value is changed ~4.8% at 10 mins of exposure time which agrees with the photo-induced dielectric enhancement in STO-based ceramic [3]. However, its response decreases with higher frequency since the polarization cannot follow to the applied external electric field at a higher frequency. For CMNO- and ZAO-doped ceramics, the samples do not show the significant change in dielectric values after UV light exposure.

The changing value of dielectric properties and exposure time for 30 mins of all ceramics at 1 kHz is shown in Fig. 3(a). BCZT, BCZT-CMNO, and BCZT-ZAO do not show a significant change in dielectric value. Interestingly, a rapid increase of capacitance occurs in a range from 15 to 20 min in BCZT-CCO. Then, the value gradually becomes stable. The maximum dielectric response upon UV light of all ceramics is summarized in Fig. 3(b). BCZT-CCO ceramic exhibits the maximum change of capacitance (\sim 60%) and dielectric loss (~15%) whereas the dielectric response of other ceramics does not differ significantly. The dielectric enhancement of BCZT-CCO may be explained by the creation of a $(V_{\it Ca}'' - V_{\it O}^{"})$ defect dipole between vacancies of Ca $(V_{Ca}^{"})$ and O $(V_{O}^{"})$ ions. To describe the formation of defect dipole, it should be mentioned first that CaO and CaCO₃ secondary phases (Fig. 1(a)) occur during the sintering process at a high temperature of the doped ceramics, which can be explained by Kröger-Vink notation in Eqs. (1) and (2), respectively.

$$Ca_{Ca}^{x} + 1/2O_{2} + 2e' \rightarrow CaO + V_{Ca}''$$
 (1)

$$Ca_{Ca}^{x} + 1/2O_{2} + CO_{2} + 2e' \rightarrow CaCO_{3} + V_{Ca}''$$
 (2)

As seen the equations, $V_{Ca}^{"}$ is induced simultaneously in doped ceramics with the presence of CaO and CaCO₃ phases. When the ceramics are under UV light, $V_{O}^{"}$ can be generated at the oxide surface, according to the formation mechanism given in Eq. (3). This phenomenon has been observed in other oxides such as CaCu₃-TiO₄O₁₂ [6], and STO-based ceramics [3].

$$1/2O_2 \to O_0^x + V_0^{"} + 2e' \tag{3}$$

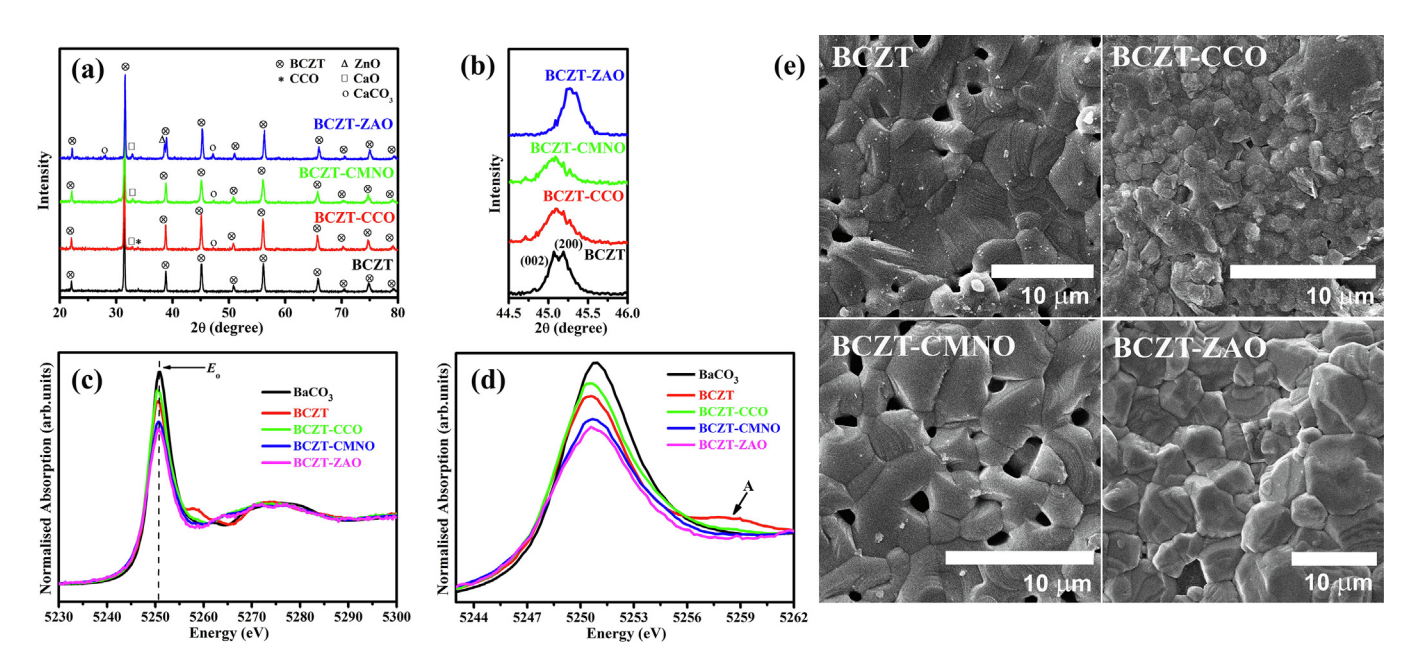


Fig. 1. (a) and (b) are XRD patterns in the 2θ range of 20°-80° and 44.5°-46°, respectively, (c) and (d) are XAS spectra and (e) is SEM images of all ceramics.

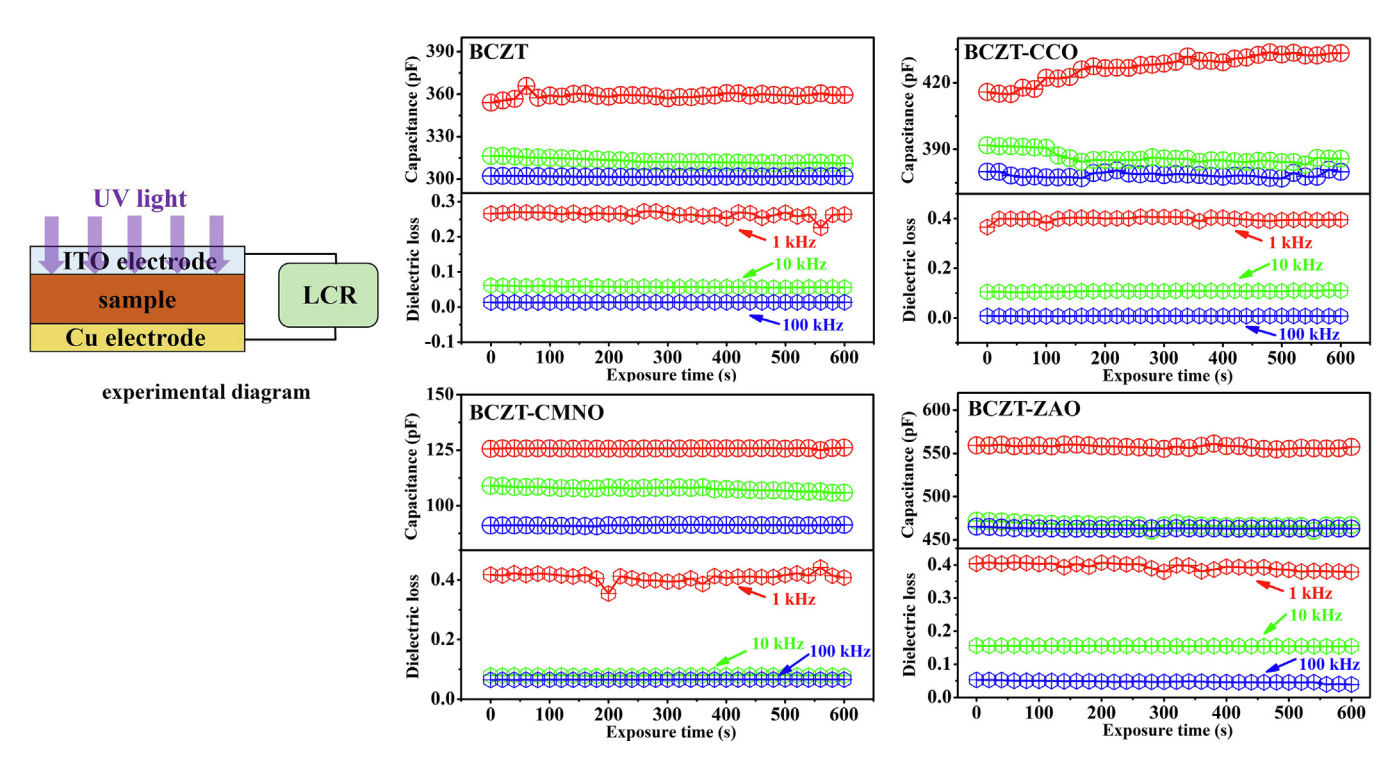


Fig. 2. Experimental diagram and dielectric properties upon UV light for 10 min at 1, 10, and 100 kHz.

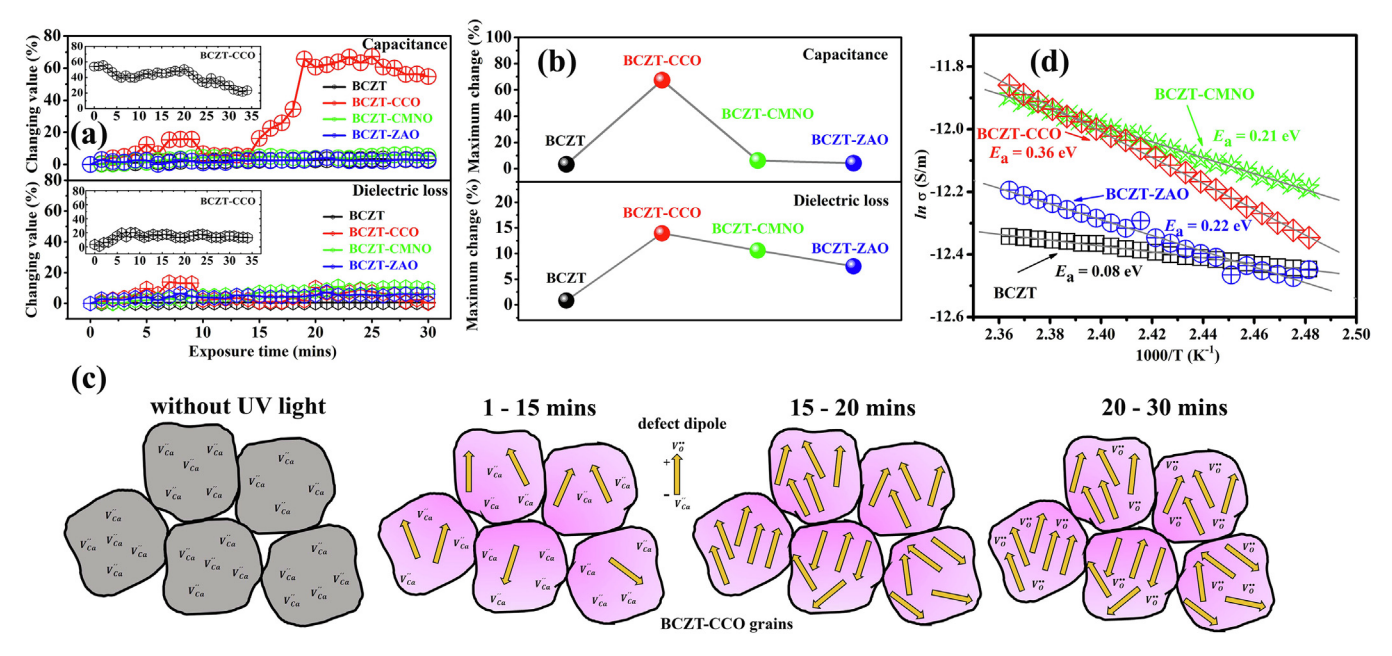


Fig. 3. (a) Is the dielectric properties upon UV light for 30 mins at 1 kHz, (b) is the maximum change in dielectric properties, (c) is the formation of defect dipole in BCZT-CCO ceramic, and (d) is Arrhenius plot of electrical conductivity of all ceramics. An inset in (a) is dielectric properties of BCZT-CCO after removing UV light.

Then, the negative charge of $V_{Ca}^{"}$ existing in the ceramic can attract the positive charge of $V_{O}^{"}$ immediately and induces $(V_{Ca}^{"}-V_{O}^{"})$ defect dipole following Eq. (4)

$$V_{Ca}'' + V_O^{..} \rightarrow (V_{Ca}'' - V_O^{..}) + 2e' + 2h'$$
 (4)

Nevertheless, the dielectric response of BCZT-CCO ceramic may not be similar to $CaCu_3TiO_4O_{12}$ [6], and STO-based ceramics [3]. In our case, $V_{Ca}^{"}$ has exhibited in the ceramic without UV light. When the ceramic is exposed by UV light, the dielectric variation is divided into three periods, including a range from 1 to 15 min,

15 to 20 min, and 20 to 30 min as seen in Fig. 3(c). For the first one, $V_O^{"}$ are gradually produced and can catch $V_{Ca}^{"}$ immediately, inducing $V_{Ca}^{"} - V_O^{"}$ defect dipoles. The formation of defect dipoles increases dielectric properties of BCZT-CCO, which is in agreement with the dielectric enhancement due to the creation of $V_{Ca}^{"} - V_O^{"}$ defect dipole upon UV light in STO-based ceramics [3]. However, in the case of BCZT-CCO, the content of $V_O^{"}$ in the first period may be smaller than $V_{Ca}^{"}$, resulting in the remaining content of unpaired $V_{Ca}^{"}$. For the second period, the $V_O^{"}$ content increases much and may be sufficient to attract the remaining $V_{Ca}^{"}$. Defect dipoles

 $(V_{Ca}^{"}-V_{O}^{"})$ are effectively formed, resulting in the rapid enhancement of the value. In the third period, the capacitance does not change much and becomes stable gradually. It is possible that there are no V''_{ca} , which can arrest V''_{0} , causing no more $V''_{ca} - V''_{0}$ defect dipoles. The capacitance value, therefore, becomes stable. After removing the UV light for 35 min (see inset in Fig. 3(a)), the capacitance of BCZT-CCO decreases gradually and becomes rapidly after 20 min, which related with its capacitance enhancement under UV light. This result is because that the re-entrance of oxygen at the surface, causing the decrease in capacitance. This phenomenon has been observed in CaCu₃TiO₄O₁₂ [6], and STO-based ceramics [3]. In the case of the dielectric loss, the value decreases gradually but at a slower rate as compared with the capacitance. Regarding BCZT-CMNO and BCZT-ZAO, the samples do not exhibit the enormous response of capacitance and dielectric loss similar to BCZT-CCO although CaO and CaCO₃ phases are present. It is because CCO is quite sensitive to O content or $V_0^{\cdot \cdot}$ [7]. Thus, upon UV light exposure, $V_0^{"}$ is therefore generated at BCZT-CCO surface easier than CMNO- and ZAO-doped samples, leading to the massive dielectric response in BCZT-CCO ceramic.

The Arrhenius plot of electrical conductivity (σ) of all ceramics is shown in Fig. 3(d). The temperature dependence of σ is fitted according to the Arrhenius equation,

$$\sigma = \sigma_0 \exp(-E_a/kT) \tag{5}$$

where σ_o , E_a , k, and T are the pre-exponential factor, the activation energy per charge carrier, Boltzmann's constant and the absolute temperature, respectively. The E_a value is extracted from the slope of linear fitting. The value indicates the energy required to move the defects, i.e., the thermally activated oxygen vacancies at high temperature [8]. Thus, the materials with low E_a value should have the more natural movement of V_o . For these ceramics, BCZT shows the minimum value of E_a (\sim 0.08 eV) meanwhile all doped ceramics show the higher E_a (\sim 0.21–0.36 eV). Thus, the V_o defect can move in BCZT easily, which reflects a low E_a . In the case of the doped ceramics, the mobility of V_o is retarded by V_{Ca} , as observed in the doped ceramics. The E_a values of all doped ceramics are, therefore, higher than BCZT.

4. Conclusions

The presence of defect dipole between vacancies of Ca and O ions could enhance dielectric properties under UV light.

BCZT-CCO showed maximum dielectric enhancement (\sim 60%) at 15–20 min mean while other ceramics did not present a significant change. The results here suggested that the doping of CCO could be useful for tuning the UV light-induced dielectric response of BCZT which may find future application in UV light sensors, detector, and other optical devices.

Acknowledgments

This research was funded by the Thailand Research Fund (TRF) and Office of the Higher Education Commission (OHEC), Ministry of Education through the TRF-OHEC Grant for New Researcher. Contract no. MRG6180109. P. Jaiban also would like to thank partial funding support from King Mongkut's University of Technology North Bangkok. Contract no. KMUTNB-62-KNOW-04. A. Watcharapasorn would like to acknowledge partial supports from the Center of Excellence in Materials Science and Technology, Faculty of Science and Chiang Mai University.

Conflicts of interest

None.

References

- [1] W. Liu, X. Ren, Large piezoelectric effect in Pb-free ceramics, Phys. Rev. Lett. 103 (2009) 257602.
- [2] Y. Zhang, H. Sun, W. Chen, A brief review of Ba(Ti_{0.8}Zr_{0.2})O₃-(Ba_{0.7}Ca_{0.3})TiO₃ based lead-free piezoelectric ceramics: past, present and future perspectives, J. Phys. Chem. Solid 114 (2018) 207–219.
- [3] P. Jaiban, S. Buntham, A. Watcharapasorn, Dielectric properties of (1-x) Sr_{0.92}La_{0.08}TiO₃-(x)CaMn_{0.98}Nb_{0.02}O₃ ceramics under violet light irradiation, Mater. Lett. 193 (2017) 133–137.
- [4] R.D. Shannon, Revised effective ionic radii and systematic studies of interatomic distance in halides and chalcogenides, Acta Cryst. A 32 (1976) 751–767.
- [5] K. Yoshii, I. Jarrige, C. Suzuki, D. Matsumura, Y. Nishihata, Y. Yoneda, T. Fukuda, K. Tamura, Y. Ito, T. Mukoyama, T. Tochio, H. Shinotsuka, S. Fukushima, Probing the Ba5d states in BaTiO₃ and BaSO₄: a resonant x-ray emission study at Ba-L₃ edge, J. Phys. Chem. Solids 73 (2012) 1106–1110.
- [6] C. Masingboon, T. Eknapakul, S. Suwanwong, P. Buaphet, H. Nakajima, S.-K. Mo, P. Thongbai, P.D.C. King, S. Maensiri, W. Meevasana, Anomalous change in dielectric constant of CaCu3Ti4O12 under violet-to-ultraviolet irradiation, Appl. Phys. Lett. 102 (2013) 202903.
- [7] K.T. Jacab, P. Gupta, Oxygen potential sand phase equilibria in the system Ca-Co-O and thermodynamic properties of Ca₃Co₂O₆ and Ca₃Co₄O_{9.163}, J. Solid State Chem. 221 (2015) 57–65.
- [8] S. Kumar, K.B.R. Varma, Influence of lanthanum doping on the dielectric, ferroelectric and relaxor behavior of barium titanate ceramics, J. Phys. D: Appl. Phys. 42 (2009) 075405.

ELSEVIER

Contents lists available at ScienceDirect

Materials Research Bulletin

journal homepage: www.elsevier.com/locate/matresbu



Influences of acceptor dopants (Cu, Mg, Fe) on electrical and optical properties of Ba_{0.7}Ca_{0.3}TiO₃ ceramics



Panupong Jaiban^{a,*}, Pimpilai Wannasut^b, Rattikorn Yimnirun^c, Anucha Watcharapasorn^{b,e}

- ^a Faculty of Science, Energy and Environment, King Mongkut's University of Technology North Bangkok, Rayong Campus, Rayong 21120, Thailand
- b Department of Physics and Materials Science, Faculty of Science, Chiang Mai University, Chiang Mai 50200, Thailand
- ^c School of Energy Science and Engineering, Vidyasirimedhi Institute of Science and Technology, Rayong 21210, Thailand
- e Center of Excellence in Materials Science and Technology, Materials Science Research Center, Faculty of Science, Chiang Mai University, Chiang Mai 50200, Thailand

ARTICLE INFO

Keywords: Photo-induced conductivity enhancement Curie temperature Acceptor doping Structural distortion

ABSTRACT

 $Ba_{0.7}Ca_{0.3}TiO_3$ (BCT) ceramics with different dopants, including Fe^{3+} , Mg^{2+} , and Cu^{2+} ions, were prepared by a solid-state sintering method. All doping elements induced a change in the crystal structure and microstructure of BCT ceramics. The dielectric, ferroelectric and piezoelectric properties of the doped ceramics were observed in a correlation between the phase fraction and difference in grain size. The decrease of grain size indicated a surface enhancement in an ultraviolet light response of doped ceramics. The recovering rate of resistivity of all ceramics after removing the light depended on dopants. The results here suggested that microstructural variation could be useful for tuning both the electrical properties and ultraviolet light-induced conductivity of perovskite materials which may find future application in optoelectronic and electronic devices.

1. Introduction

Perovskite material has a long history and plays an essential role in several electronic and optical devices, such as sensors, piezoelectric actuators, capacitors, and light detectors. It is well-known that an atomic arrangement in this material is ABO3 structure, in which positive ions occupy A and B sites and O is oxygen ions. Perovskite material can be synthesized using several methods such as solid-state reaction, gas phase preparation, and wet chemical method. For the solid-state reaction, the starting and final materials are solid such as nitrates, carbonates, and oxides, which were mixed by the desired composition through the milling media. Then, the powder and ceramics can be obtained by the calcination and conventional sintering techniques at high temperature, respectively. Perovskite films are widely prepared by gas phase preparation, where the starting material with gas-state is deposited on the substrate under different temperature and atmosphere. In the case of the wet chemical method, its principle is co-precipitation of metal ions through precipitating agents such as the oxalate, hydroxide, acetate, citrate, cyanide, and thermal treatment such as freezedrying, plasma spray-drying, combustion, and microwave synthesis [1–4]. Regarding the perovskite material synthesized from these methods, the chemical method can produce the material with large surface and high homogeneity at a lower temperature compared with solid-state reaction. However, it is found that the perovskite ceramicbased piezoelectric devices are often fabricated from the solid-state reaction.

Lead zirconate titanate (PZT) compound is a widely used perovskite material. However, the material has an environmental limitation although its electrical properties are quite attractive. According to the drawback of PZT, some lead-free compounds, therefore, are focused in order to replace PZT, including barium titanate (BT), bismuth sodium titanate (BNT), and potassium sodium niobate (KNN). The enhancement in electrical and optical properties of these lead-free materials has been extensively studied using a substitution of host ions by different dopants (e.g., Sr²⁺, Bi³⁺, and Ca²⁺ ions at A-site and Fe³⁺, Mg²⁺, Nb^{5+} , Co^{2+} , Ta^{5+} , Zr^{4+} , and Cu^{2+} ions at B-site [5–7]). Among these modifications, Ba(Ti_{0.8}Zr_{0.2})O₃-(Ba_{0.7}Ca_{0.3})TiO₃ (BTZ-BCT) ceramic has promoted promising electrical properties, such as excellent piezoelectric and dielectric performance [8]. Moreover, (Ba_{0.7}Ca_{0.3})TiO₃ (BCT) ceramic has also shown an attractive response on ultraviolet light (UV) irradiation with suitable doping of La³⁺ ions (i.e., 0.01 to 0.03) [9], which makes it an alternative material for UV sensors and detectors. When compared with its electrical properties, a focus on the optical properties of BCT ceramic, particularly UV light response, is still scarce. Thus, this work focuses on a simultaneous investigation of the electrical and optical properties of BCT material.

As the results from ref. [9] show, the critical enhancement in UV light-induced properties was observed in a relationship with the

E-mail address: p.jaiban@gmail.com (P. Jaiban).

^{*} Corresponding author.

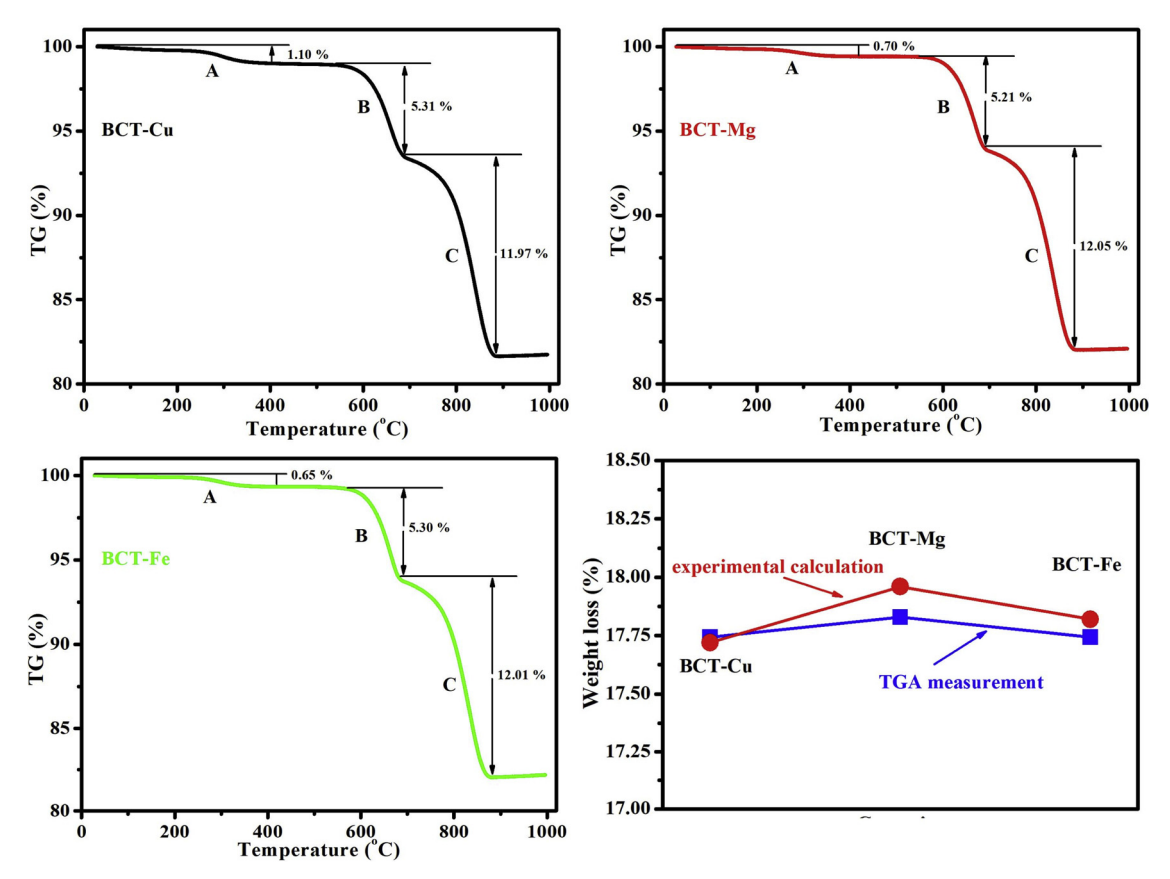


Fig. 1. TGA curves and the weight loss measured from TGA and experiment of all powders.

creation of oxygen vacancies at the surface. Thus, in order to enhance photoresponse of BCT ceramic, we synthesized BCT ceramic with an introduction of oxygen vacancies by substitution of acceptor dopants, including ${\rm Fe^{2+}}$, ${\rm Mg^{2+}}$, and ${\rm Cu^{2+}}$ ions at the B-site because the optical properties of BCT doped by these ions have not been reported thus far. BCT ceramics with the addition of ${\rm Fe^{2+}}$, ${\rm Mg^{2+}}$, and ${\rm Cu^{2+}}$ dopants were prepared in this work. The effects of crystal structure and microstructural features on their dielectricity, piezoelectricity, ferroelectricity, and UV light response have been discussed in detail.

2. Experimental

The specimens were fabricated according to the chemical formula $(Ba_{0.7}Ca_{0.3})_{0.99}Ti_{0.98}Fe_{0.02}O_{2.98}$ (BCT-Fe), $(Ba_{0.7}Ca_{0.3})Ti_{0.98}Mg_{0.02}O_{2.98}$ (BCT-Mg) and $(Ba_{0.7}Ca_{0.3})Ti_{0.98}Cu_{0.02}O_{2.98}$ (BCT-Cu). The powders were prepared using the conventional mixed-oxide method. The starting materials used in this study were $CaCO_3$ (Sigma-Aldrich), BaCO_3 (Sigma-Aldrich), CuO (Sigma-Aldrich), MgO (Sigma-Aldrich), Fe_2O_3 (Sigma-Aldrich), and TiO_2 (Riedel-de Haën). The mixtures of oxides were ball milled in ethanol for 24 h, dried at 120 °C for 24 h and calcined in a closed alumina crucible at 1000 °C for 2 h. After sieving, a few drops of 3 wt% PVA (polyvinyl alcohol) binders were added to the mixed powders, which were subsequently pressed into pellets with a diameter of 15 mm using a uniaxial press with 1.5-ton weight. Binder removal was carried out by heating the pellets at 500 °C for 1 h. These pellets were then sintered at 1350 °C for 4 h of dwell time with a heating/cooling rate of 5 °C/min on a covered alumina plate.

Thermogravimetry (TGA) was used to study the thermal evolution of the calcined powders from room temperature to 1000°C. The morphology and crystallinity of calcined powders were observed using a transmission electron microscopy (TEM). Phase identification of the sintered specimens was investigated in a 2-theta range of 10 to 80° using an X-ray diffractometer (Mimiflex, Regaku). After that, the phase

and lattice parameters of all calcined powders and ceramics were obtained by the Rietveld refinement method using GSAS software [10]. The scanning electron microscopy (SEM) was used to investigate the microstructure of the ceramics. The chemical composition was studied by X-ray photoelectron spectroscopy (XPS) using a PHI 5000 Versa Probe II (ULVAC-PHI, Japan) at the SUT-NANOTEC-SLRI joint research facility, Beamline 5.3: SUT-NANOTEC-SLRI XPS, Synchrotron Light Research Institute (SLRI), Thailand. The monochromatic Al K α X-ray (1486.6 eV) was used as an excitation source. All binding energies of the samples were calibrated with the C1s (C–C bond) peak with binding energy at of 284.8 eV.

For electrical property measurements, the sintered ceramics with a diameter of 15 mm were polished using sandpaper to decrease the thickness of the sample. After obtaining the desired thickness (1 mm), two parallel silver square electrodes were coated on the surface of the polished ceramics. Then, an Agilent B4262 LCR-meter was used to measure the dielectric properties of the samples at a frequency of 1 to 100 kHz upon the increase of the temperature. A ferroelectric hysteresis loop of each sample was obtained using a computer-controlled modified Sawyer-Tower circuit. The electric field was applied to the samples by a high voltage AC amplifier at 20 kV/cm. A digital oscilloscope then recorded the polarization electric field (P-E) loop. For piezoelectric measurement, the samples were poled in a silicone oil bath under a DC electric field of 3-12 kV/cm for 30 min. Then, the piezoelectric coefficient was measured using a quasi-static d_{33} meter by applying a mechanical force to the electrode surfaces of the sample, and the generated voltage across the sample was recorded. The planar electromechanical coupling coefficient was determined by a measurement of the resonant and anti-resonant frequencies from the first minimum and maximum admittance peaks using a 4284A LCR meter.

To study the effects of UV light on resistance, we used the samples with a similar dielectric measurement size as a function of temperature. After this, we fabricated two platinum electrodes with a 2-mm-wide

exposed surface region in smaller spacing between two electrodes (50 $\mu m)$ using plasma sputtering (GSL-1100X-SPC-12) for 1 min. The samples were exposed to the incident UV light. The UV light intensity was set to $1.7\,W/cm^2$ as measured by a THORLABS detector (S120VC). The resistance was measured by a source meter (Agilent B29014).

3. Results and discussion

Fig. 1 shows the TGA curve of all powders from room temperature up to 1000 °C. From the figure, it could be divided into three parts for the thermal evolution of these powders. The first one (marked as A) was about room temperature to 300 °C, which could be ascribed to the evaporation of the residual non-structural water (weight loss ~0.65 -1.1%). The second one (weight loss ~5.2-5.3%) was attributed to the combustion reactions and preliminary synthesis of BCT, which was observed in the temperature range from 600 to 700 °C as marked B part. When the temperature increased from 700 °C to 900 °C (part C), the weight loss of BCT-based powders was about 12%, which related to the decomposition of CO2 and the reaction of BCT-based formation. The feature of the weight loss upon increase of the temperature of BCT was in agreement with BTZ-BCT synthesis [11]. The comparison between the total weight loss of the TGA curve and the preliminary calculation (i.e., the powder weight before and after the calcination process) of all powders are summarized in Fig. 1. The values are similar for each powder (~17 to 18%), which confirmed the complete reaction formation of these powders.

TEM images of all calcined powders are shown in Fig. 2. As seen in the figure, the particle shape was a sphere and polyhedral. The average size of particles estimated from the TEM image was about 50–100 nm. The selected area diffraction (SAD) patterns are given in an inset together with high-resolution TEM image of the selected particles (marked by the green arrow for each composition). These results could confirm the crystallinity of BCT-Cu, BCT-Mg, and BCT-Fe powders. With these calcined powders, the lattice fringes were observed clearly and were about 0.39 nm for the selected area A and F, -0.28 nm for the selected area B, C, and D, and -0.23 nm for the selected area E. This observation would be discussed together with their XRD diffraction

patterns in a later section.

The Rietveld refinement of X-ray diffraction patterns of all calcined powders and ceramics was carried out using GSAS software [10]. The reference data of BaTiO₃ phase with tetragonal structure (P4mm), orthorhombic structure (Amm2), rhombohedral structure (R3 m), cubic structure (Pm-3 m), and CaTiO₃ phase with orthorhombic structure (Pbnm) was used as the starting phases for the refinement of XRD patterns of all samples. The refinement results are shown in Fig. 3 and the extracted parameters are listed in Table 1. Regarding the calcined powders, it was found that all powders were composed of rhombohedral, orthorhombic, and CaTiO₃ phases. Interestingly, the amount for each phase was dependent on the dopants, particularly the rhombohedral and orthorhombic phases. The difference of phase fraction would be discussed together with their electrical properties. When comparing the interplanar spacing (d_{hkl}) values obtained from XRD refinement and the spacing values measured from TEM images, it was found that the spacing of 0.39 nm correlated well with the (100) plane of both orthorhombic and rhombohedral structures (d_{110} -0.39 nm). The (002) plane of orthorhombic and (101) plane of rhombohedral structure accompanied with 0.28 nm (d_{002} , d_{101} 0.28 nm). For the spacing value of 0.23 nm, the value related to the (102) plane of orthorhombic and (111) plane of rhombohedral structure (d_{102} , d_{111} 0.23 nm). These results could confirm the coexistence between orthorhombic and rhombohedral phases in these powders. In the case of CaTiO₃ phase, there was no significant difference of phase fraction between these powders. However, the presence of CaTiO₃ phase had been reported by several previous works [12-14], which was attributed to a maximum solubility limit of Ca^{2+} to Ba^{2+} ions (x = 0.23) in the $Ba_{1-x}Ca_xTiO_3$ binary system [12,15,16]. The X-ray diffraction patterns of all ceramics were also refined in this study as shown in Fig. 3. As seen in the figure and table, it was found that the phase fraction of orthorhombic, rhombohedral, and CaTiO3 phases was not different from their powders, suggesting that the ceramic process did not affect significantly phase fraction and the crystal structure of all sintered samples.

Fig. 4(a) illustrates the microstructural observation of all ceramics. As seen in the figure, all samples showed dense microstructure with relative density values greater than 95%. This indicated that these

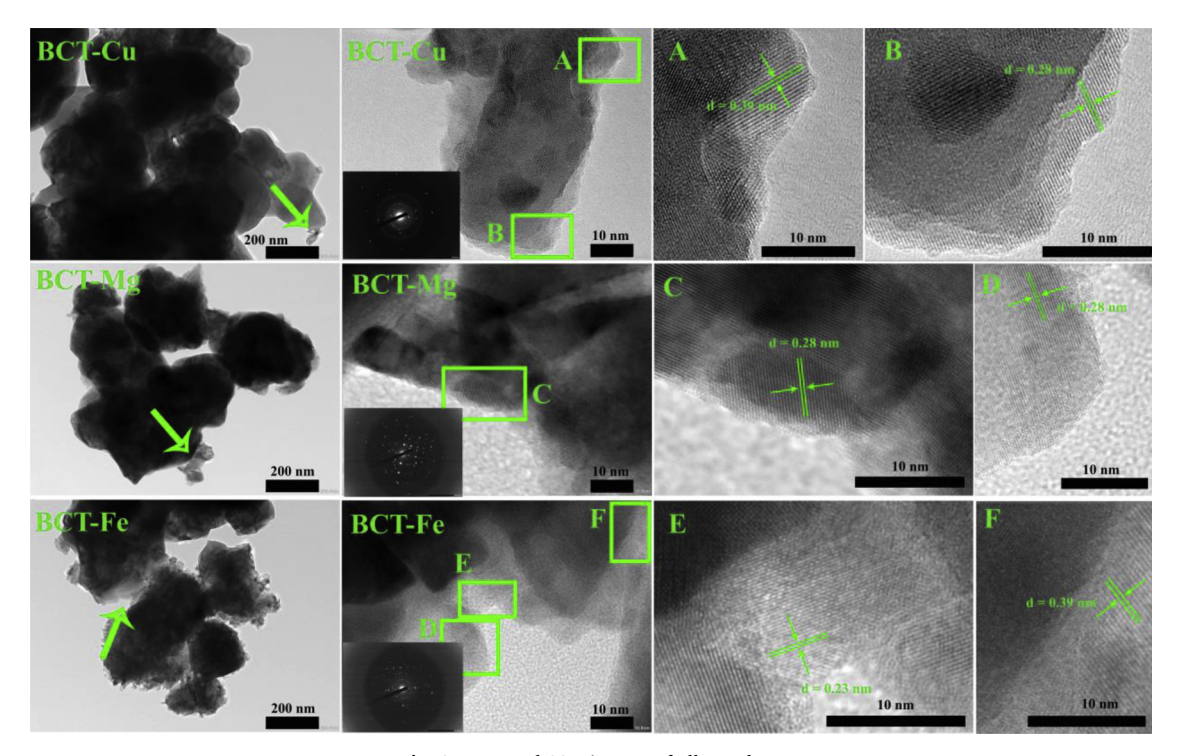


Fig. 2. TEM and SAD images of all powders.

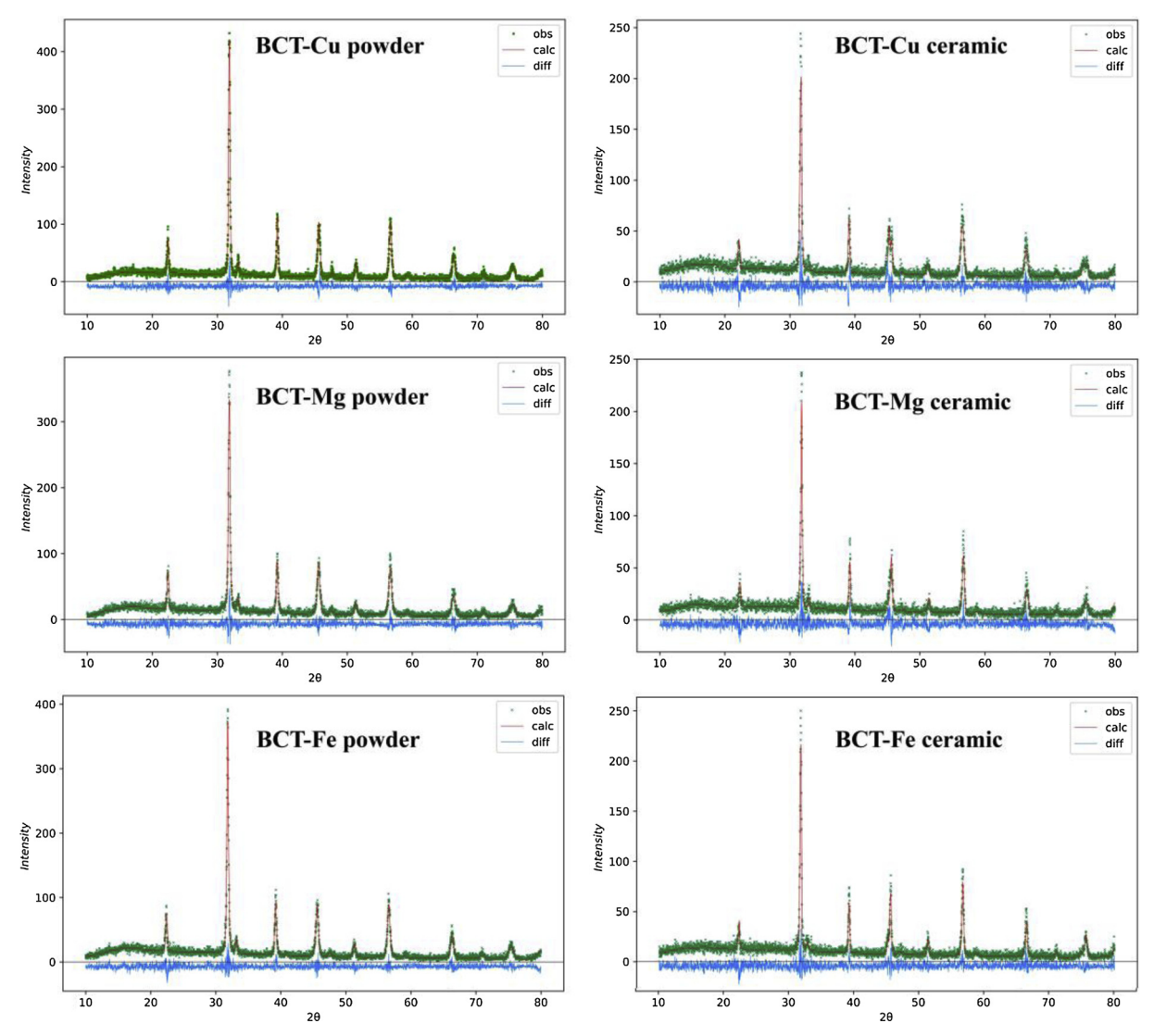


Fig. 3. Rietveld refinement of all powders and ceramics.

 Table 1

 Phase fraction and lattice parameters of all powders and ceramics.

Samples	Phase	Fraction (wt%)	Lattice parameters (Å)	Volume (ų)	
BCT-Cu powder	orthorhombic	0.68	a = 3.9765, b = 5.6403, c = 5.6787, α = 90	127.360	
	rhombohedral	0.12	$a = 3.9893, \alpha = 90.014$	63.490	
	CaTiO ₃	0.20	$a = 5.3999$, $b = 5.4197$, $c = 7.6580$, $\alpha = 90$	224.118	
BCT-Cu ceramic	orthorhombic	0.72	$a = 3.9661$, $b = 5.6504$, $c = 5.6677$, $\alpha = 90$	127.013	
	rhombohedral	0.16	$a = 3.9799, \alpha = 90.135$	63.040	
	CaTiO ₃	0.12	$a = 5.3340$, $b = 5.5662$, $c = 7.6761$, $\alpha = 90$	227.908	
BCT-Mg powder	orthorhombic	0.35	$a = 3.9845$, $b = 5.6652$, $c = 5.6643$, $\alpha = 90$	127.860	
	rhombohedral	0.46	$a = 3.9905, \alpha = 89.949$	63.546	
	CaTiO ₃	0.19	$a = 5.4063$, $b = 5.4614$, $c = 7.6476$, $\alpha = 90$	225.814	
BCT-Mg ceramic	orthorhombic	0.31	$a = 3.9485$, $b = 5.6682$, $c = 5.7077$, $\alpha = 90$	127.745	
	rhombohedral	0.50	$a = 3.9881, \alpha = 89.794$	63.430	
	CaTiO ₃	0.19	$a = 5.4113$, $b = 5.5532$, $c = 7.6924$, $\alpha = 90$	231.156	
BCT-Fe powder	orthorhombic	0.48	$a = 3.9851$, $b = 5.6691$, $c = 5.6848$, $\alpha = 90$	128.432	
	rhombohedral	0.36	$a = 3.9976, \alpha = 90.052$	63.888	
	CaTiO ₃	0.16	$a = 5.4277$, $b = 5.4477$, $c = 7.6492$, $\alpha = 90$	226.179	
BCT-Fe ceramic	orthorhombic	0.46	$a = 3.9623, b = 5.6421, c = 5.6939, \alpha = 90$	127.296	
	rhombohedral	0.38	$a = 3.9823, \alpha = 90.027$	63.154	
	CaTiO ₃	0.16	$a = 5.3931$, $b = 5.4549$, $c = 7.7316$, $\alpha = 90$	227.460	

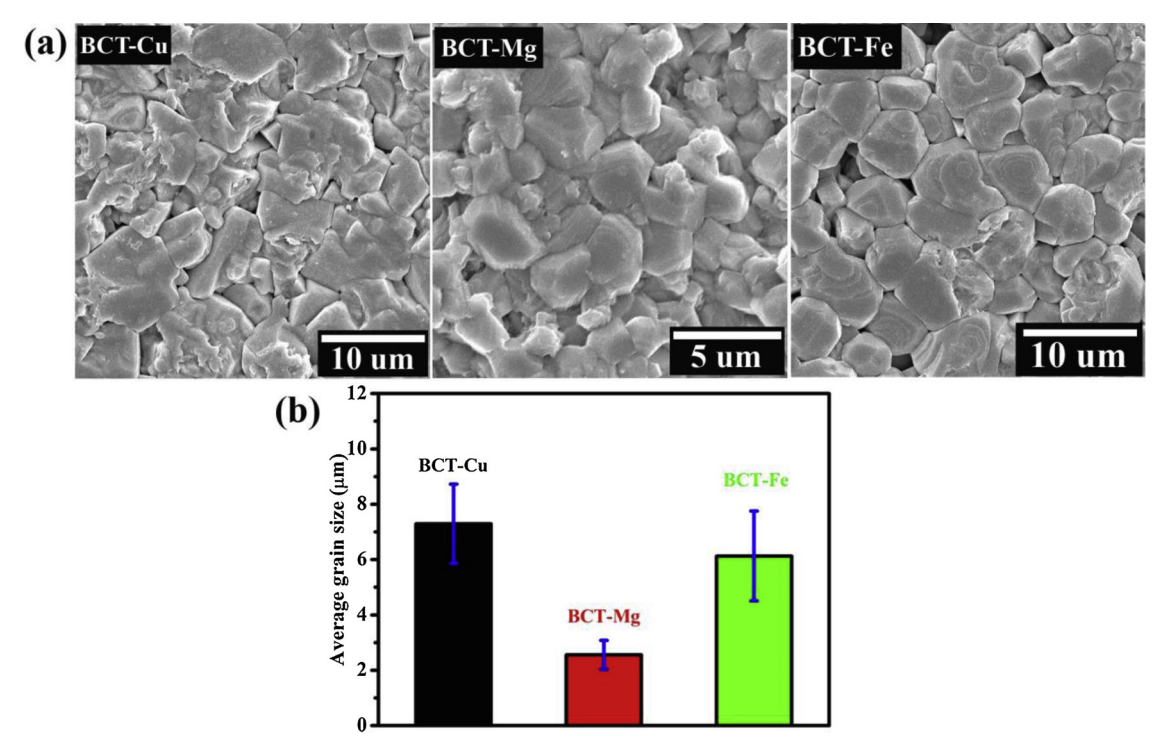


Fig. 4. (a) and (b) are microstructural images and average grain sizes of all ceramics, respectively.

dopants did not affect the physical properties of BCT ceramics. However, the addition of these dopants caused a significant difference in the grain size of the ceramics. The average grain sizes of all samples are presented in Fig. 4(b). The ceramics with Cu and Fe doping possessed similarly large grain sizes of approximately 6-7.5 µm, while the Mgdoped sample showed the microstructure, including smaller grains (i.e., 2.5 µm). In general, the decrease in the average grain size of the perovskite ceramic may be mainly due to the creation of oxygen vacancies produced by acceptor doping. The defects preferred to exhibit at the grain boundaries, leading to inhibition of grain growth during a conventional sintering process. However, in this study, all dopants (i.e., Cu²⁺, Mg²⁺, and Fe³⁺ ions) were acceptor doping. Thus, this reason might not be applicable to our case. For other possible factors, it was because the doping of MgO tended to segregate at boundaries more than other dopants, leading to the suppression of grain growth rate at high temperatures. This result was accompanied with several reports that Mg2+ ions had been substituted into well-known perovskite ceramics, such as $BaTiO_3$ [17], $(Ba_{0.95}Ca_{0.05})(Ti_{0.85}Zr_{0.15})O_3$ [18], and $Bi_{0.5}Na_{0.5}TiO_3 - Ba_{0.85}Ca_{0.15}Ti_{0.85}Zr_{0.1}Sn_{0.05}O_3 \ [19].$

XPS spectra for Ba 3d, Ca 2p, and Ti 2p core levels of all ceramics are shown in Fig. 5. As seen in the figure, the Ba 3d peaks in all samples showed a good fit to four peaks, locating at binding energy (BE) values about 778.5, 780.2, 793.8 and 795.5 eV. The peaks locating at BE of about 780.2 and 795.5 eV corresponded to the spin-orbit doublet, i.e., Ba $3d_{5/2}$ and Ba $3d_{3/2}$, 3d core level of Ba ions, respectively. The spinorbit energy separation (ΔE) between both peaks was 15.3 eV. This result confirmed that the existence of Ba in the 2+ oxidation state in the perovskite structure of these ceramics, which had been observed in bulk and nano BaTiO₃ [20,21]. The shoulder peaks (marked as A and B peaks) at lower BE side were not related to the different oxidation state but indicated the surface defect and relaxation phase formed at the ceramic surface [21]. The deconvoluted Ca 2p XPS spectra of all ceramics showed a precise fit to two peaks located at BE values-347.0 and 350.5 eV, which were associated with Ca $2p_{3/2}$ and Ca $2p_{1/2}$ spin-orbit doublet core level of Ca, respectively. The ΔE value between Ca $2p_{3/2}$ and Ca $2p_{1/2}$ core level was ~3.5 eV, indicating the presence of Ca²⁺ ions in these ceramics. For the deconvolution of Ti 2p XPS spectra of all ceramics, the fitting indicated two peaks, which were located at BE of about 458.1 and 464.0 eV. These two peaks corresponded to Ti $2p_{3/2}$ and Ti $2p_{1/2}$ spin-orbit doublet with ΔE -5.9 eV. This observation suggested the existence of Ti⁴⁺ ions in these ceramics, which was in good agreement with several reports [20,21].

Fig. 6 shows the real (ε') and imaginary (ε'') parts as a function of temperature of all ceramics at a frequency range of 1, 10, and 100 kHz. As seen in the figure, it was found that all ceramics showed the frequency independence of dielectric properties, suggesting normal ferroelectric behavior. Interestingly, the diffuseness of these dielectric peaks was dependent on each dopant, particularly BCT-Mg ceramic. The possible factor was from their microstructure in which the microstructure composing of smaller grains showed broader dielectric phase transition attributed to the dominance of the space charge effect, weakening of long-range ferroelectric interaction, and higher internal stress in fine-grained ceramics [22]. Regarding the dielectric properties for each dopant at 1 kHz (see in Fig. 7(a) and (b)), it was seen that the temperatures at maximum $\varepsilon^{'}$ and $\varepsilon^{''}$ values exhibited were -105 °C for BCT-Cu, 10 °C for BCT-Mg and 70 °C for BCT-Fe. The observed temperature was dependent on each dopant. The different amount of orthorhombic and rhombohedral phase was believed to affect their phase transition temperature significantly. In general, this temperature indicates transformation from the ferroelectric phase to a paraelectric phase (i.e., cubic structure). Thus, the material with the structure close to cubic structure such as rhombohedral structure should have lower phase transition temperature. With these results, the ceramic with Cu addition had a maximum phase transition temperature because this sample clearly showed the smallest fraction of the rhombohedral phase as compared with others (see in Table 1). In the case of Mg and Fe doping, it was quite apparent that the presence of rhombohedral caused the abrupt decrease in their phase transition temperatures. BCT-Mg ceramic had the most substantial fraction of rhombohedral phase (~0.50). This feature induced the phase transition temperature near the ambient temperature of the ceramic.

P-E hysteresis loops at room temperature of all ceramics are illustrated in Fig. 7(c). The change in crystal structure may be an important factor causing a different P-E hysteresis loop. It should be mentioned

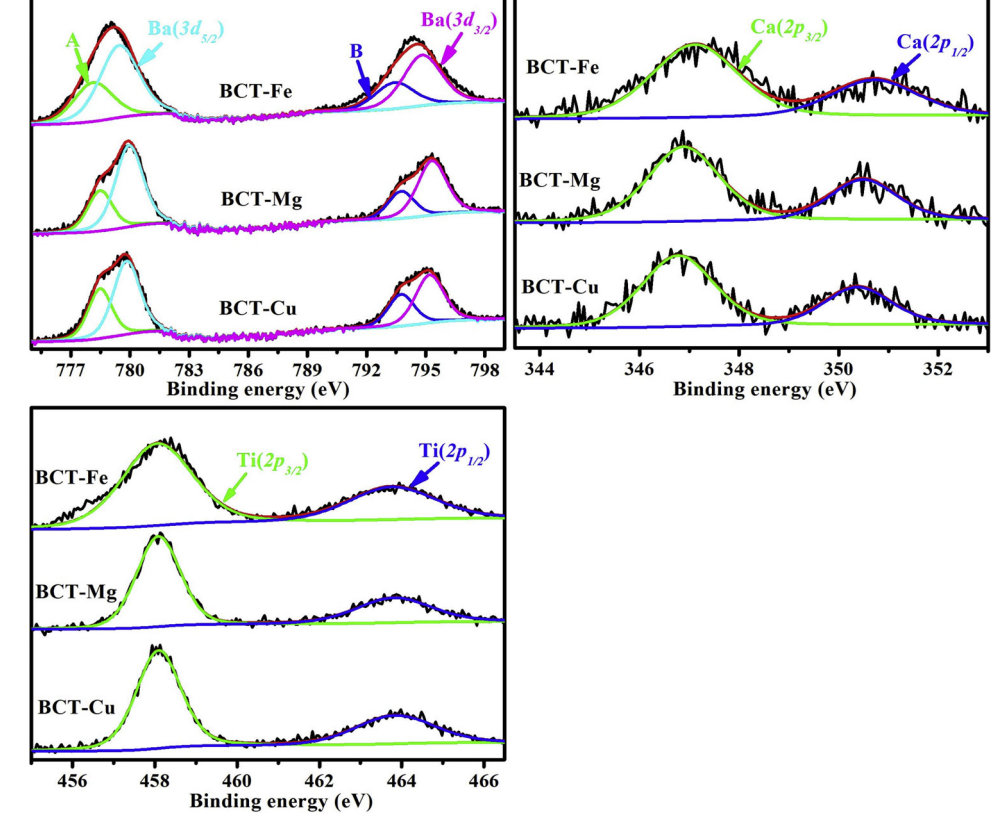


Fig. 5. XPS spectra of Ba3d, Ca2p, and Ti2p of all ceramics.

first that the material with higher ferroelectricity (particularly a tetragonal or orthorhombic structure) often promoted regular *P-E* hysteresis loops, while the material with lower ferroelectricity or the structure close to cubic or rhombohedral phase showed slimmer *P-E* hysteresis loops. Regarding these ceramics, it was seen that BCT-Cu possessed a standard hysteresis loop. In the case of BCT-Mg and BCT-Fe, both ceramics exhibited a slim-like hysteresis loop, which associated well

with their crystal structure. The ferroelectric parameters, including remanent polarization (P_r) and coercive field (E_c), extracted from their P-E loops are given as inset in Fig. 7(c). BCT-Cu showed higher P_r and E_c values, when compared with those of BCT-Mg and BCT-Cu. These parameters confirmed the significant influence of crystal structure on the ferroelectric properties of these ceramics. In addition to the dominance of crystal structure, a trend of ferroelectric parameters was

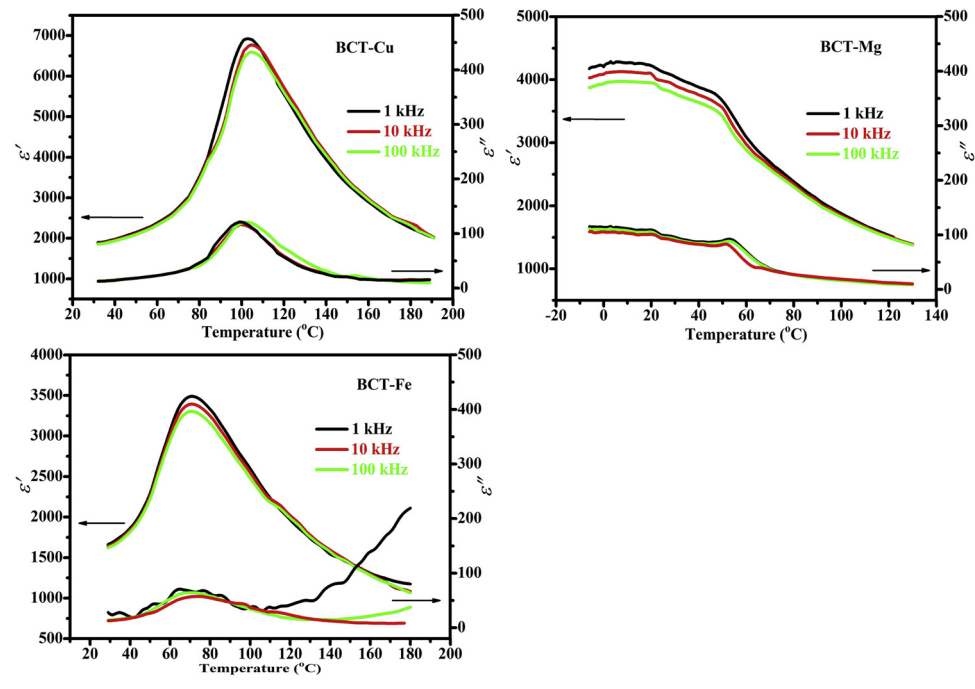


Fig. 6. $\varepsilon^{'}$ and $\varepsilon^{''}$ as a function of temperature at a frequency of 1 kHz, 10 kHz, and 100 kHz.

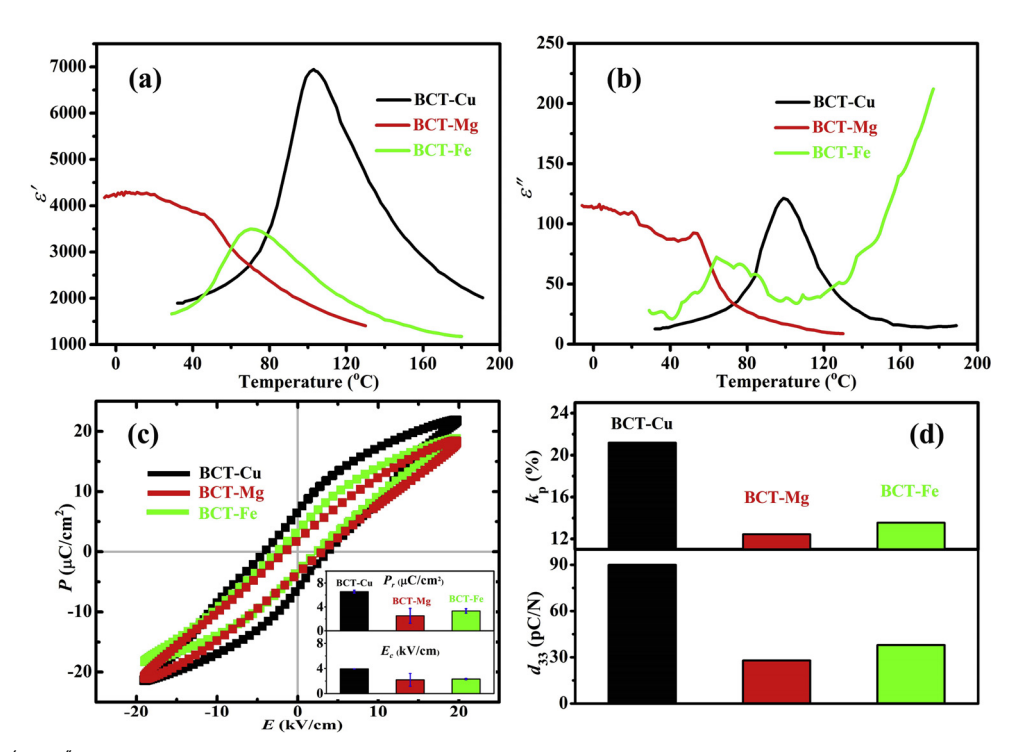


Fig. 7. (a) and (b) are ε' and ε'' as a function of temperature at 1 kHz, (c) is ferroelectric properties, an inset is remanent polarization, and coercive field of all ceramics and (d) is piezoelectric properties of all ceramics.

accompanied by a decrement of grain size. This result could be an additional reason for the change in their ferroelectricity. Because the long-range ferroelectric interaction was obstructed by grain boundaries leading to a decrease of ferroelectricity, a short-range ferroelectric order and weak polarizations existed in fined grains. The BCT-Cu and BCT-Mg ceramics, therefore, had maximum and minimum ferroelectric parameters, respectively.

Piezoelectric properties, including the piezoelectric coefficient (d_{33}) and electromechanical coupling factor (k_p) , of all ceramics, are given in Fig. 7(d). As seen in the figure, BCT-Cu ceramic showed maximum values of both d_{33} (90 pC/N) and k_p (21%)while the values became much lower in BCT-Fe and BCT-Mg ceramics. In general, piezoelectricity is related directly to a remanent polarization of the material. Thus, the material having large remanent polarization should offer high piezoelectricity. Regarding all ceramics, the feature of piezoelectric properties was associated with their remanent polarizations observed in Fig. 7(c). Hence, it could be mentioned that the piezoelectric response of these ceramics was attributed to their ferroelectricity. With these results, it was seen that crystal structure and microstructural characteristics were found to significantly affect the dielectric, ferroelectric, and piezoelectric response of all ceramics. However, these electrical features were only regarded as the bulk properties of the materials. To provide a surface aspect of these perovskite ceramics, we were also interested in the effects of ultraviolet (UV) light exposure on the electrical resistance of all samples. Therefore, a set-up diagram of resistivity measurement is illustrated as an inset in Fig. 8.

The electrical resistances upon UV light irradiation of all ceramics are shown in Fig. 8. Before UV light was turned on, the resistance value of BCT-Cu was quite stable, while the values of the ceramics with the addition of Mg and Fe dopants increased abruptly in exposure time ranging from 10 to 20 s, and became stable. This feature might be due to an initial state of measurement. After UV light was first turned on, the resistance dropped immediately and decreased gradually during continuous irradiation. When UV illumination was removed, the values increased suddenly and returned to their initial state at a slower rate. The resistance response of all samples still was maintained upon stimulus and without UV light. With the results, variation in resistivity of

all ceramics upon light exposure was attributed to the creation of oxygen vacancy: $O_0^x \leftrightarrow 1/2O_2 + V_0^x + 2e'$ [23] which effectively doped free electrons to the system and induced a better conduction in the sample. When the UV light was switched off, the oxygen would re-combine with free electrons at the surface, leading to the recovery in resistivity of the ceramics. Such an oxygen vacancy effect had been observed previously in other metal oxides (e.g., SrTiO₃ [24], KTaO₃ [25], TiO, ZnO [26], and CaCu3Ti4O12 [27]. In addition to UV light-induced conductivity, it was seen that the photoresponse was dependent on each dopant. We summarized the responsive ability on UV light of all ceramics in Fig. 8. From the figure, BCT-Mg ceramic showed the largest photoresponse (i.e., 35%), and the minimum value (i.e., 15%) was observed in BCT-Cu. The photoresponse of these ceramics seemed to involve their grain sizes (see Fig. 4(b)). The observed relationship between photoresponse and grain size could be explained by a trapping process of the oxygen vacancies at grain boundaries. During UV light illumination on the surface, oxygen vacancies were induced and entrapped immediately into grain boundaries. Hence, there were non-equilibrium electrons inside the grains, causing the change in electrical resistivity at the surface of the materials. From this mechanism, the fine grain microstructure (i.e., large grain boundaries) should trap oxygen vacancies more than the microstructure with larger grains, leading to better enhancement of conductivity in the material possessing small grains. Thus, the BCT-Mg sample with smaller grains had larger response as compared to the others. The improvement in photoresponse of BCT-Mg ceramic due to the influence of small grains was in agreement with another oxide (i.e., In₂O₃ reported by E.A. Forsh et al. [28]).

In addition to the microstructural dependence of UV light response, the difference in recovering time of the resistance to its original value after the UV light was turned off was observed further. To explain this phenomenon, we exposed UV light to the samples until obtaining the saturating value as shown in Fig. 9. As seen in the figure, when the light was switched on, the response of the resistance value of all ceramics was still similar in previous cases (Fig. 8). However, after the light was removed, the resistance of BCT-Mg and BCT-Cu increased suddenly in a few seconds and gradually returned to the initial state. By contrast, BCT-Fe ceramic exhibited a gradual increase of resistivity to the

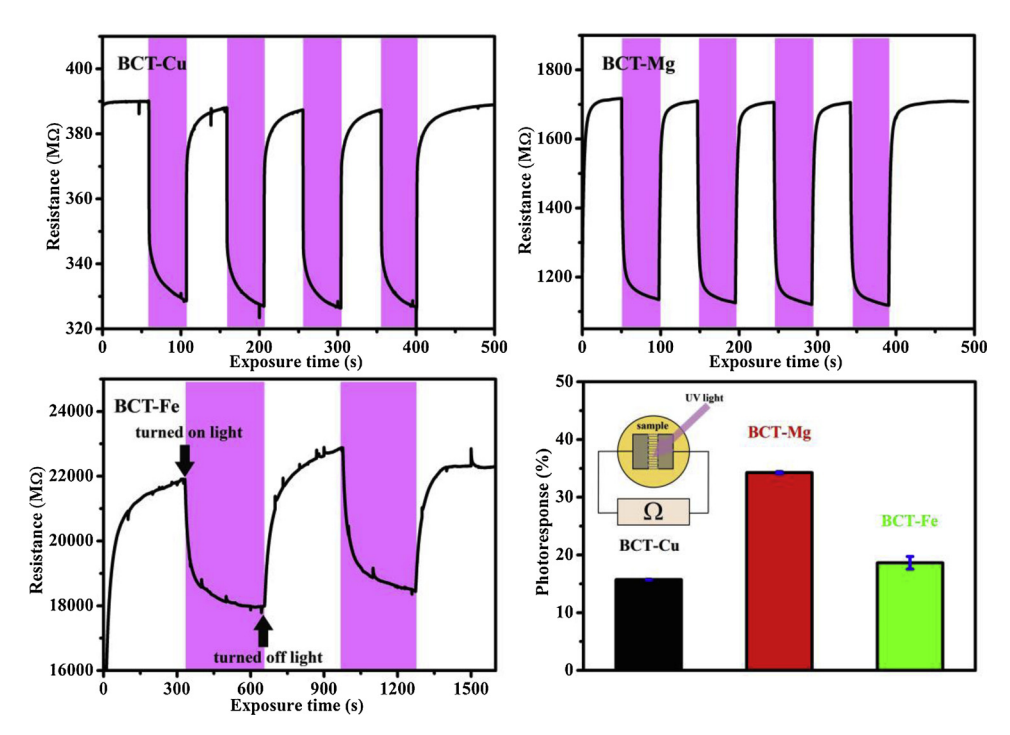


Fig. 8. The relationship between resistance and exposure time under UV light of all ceramics and a photoresponse of all ceramics.

original state. The relative recovering values as a function of the waiting time of all ceramics are plotted in Fig. 9. BCT-Fe ceramics showed longer recovering time compared with BCT-Cu and BCT-Mg. The waiting time of all ceramics is given as inset in Fig. 9. In the figure, the longest time (i.e., 120 s) was found in BCT-Fe, while there was no significant difference for BCT-Cu and BCT-Mg ceramics. BCT ceramic substituted by only Fe dopants took longer for recovery of resistance, although all dopants were acceptor-type doping. With this result, the variation in the oxidation state of these dopants might be a possible factor. In the case of the BCT-Mg sample, Mg ions had oxidation states

of only 2+; therefore, its recovering time was rapid (-15 s). Interestingly, BCT-Cu and BCT-Fe showed the apparent difference in recovering times (-15 s for BCT-Cu and -120 s for BCT-Fe) although Cu and Fe ions were transition metal. This result might be attributed to the more active response of Cu ions than Fe ions, as suggested by O.P. Taran et al. [29]. Thus, the recovering value of BCT-Cu, therefore, was similar to BCT-Mg. In the case of BCT-Fe, after the UV light was switched off, oxygen vacancies would not re-combine immediately with electron inside the grains due to the slower response. A longer time was needed to return to the original state as compared with regular cases of BCT-Cu and BCT-

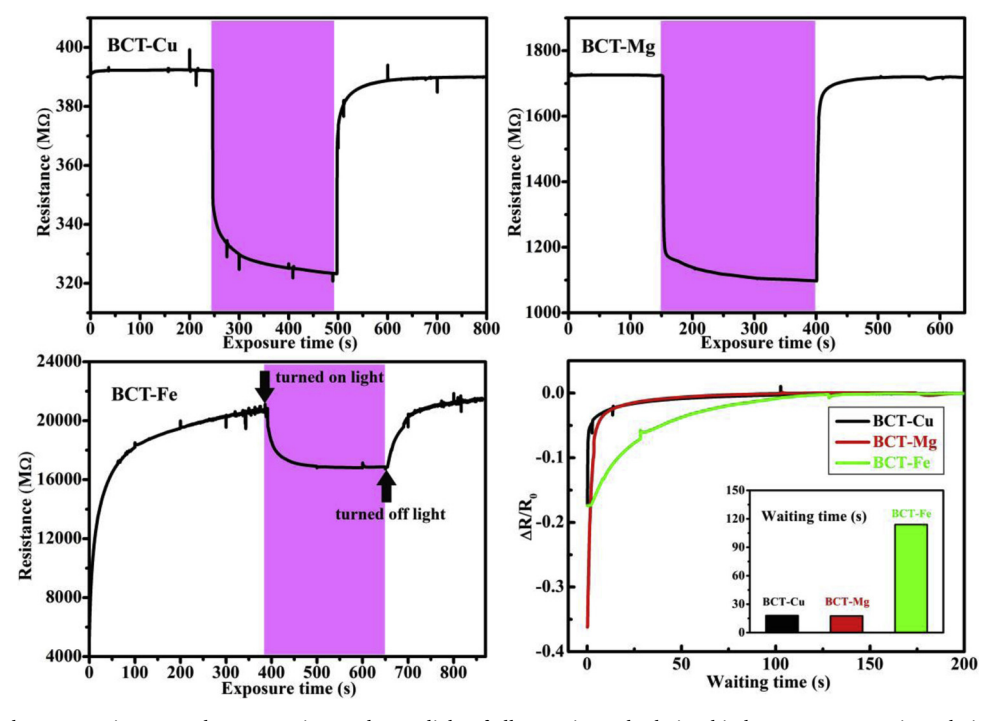


Fig. 9. The relationship between resistance and exposure time under UV light of all ceramics and relationship between a recovering relative resistance and waiting time of all ceramics after removing UV exposure. An inset is waiting time of all ceramics.

Mg. As a result here, it suggested that the photosensitivity of BCT-based materials may be tunable by microstructural engineering and different dopants, which could be an alternative material for such devices.

4. Conclusion

In this work, BCT-Cu, BCT-Mg, and BCT-Fe ceramics were fabricated using solid-state sintering process. All dopants induced the change in crystal structure and microstructure of BCT ceramics. The dielectric, ferroelectric, and piezoelectric properties were observed in correlation with the variation of crystal structure and grain size. The decrease in grain size caused a better UV light response. The dopants significantly affected the recovery rate of resistivity. These results suggested that microstructural variation and difference of dopants could be useful for tuning both the electrical properties and ultraviolet-induced conductivity of perovskite materials, which may find future applications in optoelectronic and electronic devices.

Acknowledgments

We acknowledge W. Meevasana and S. Nathabumroong for assistance with the experiment and would like to thank Narong Chanlek and the BL5.3:SUT-NANOTEC-SLRI XPS, Synchrotron Light Research Insititute (SLRI), Thailand for XPS measurement. This research was funded by King Mongkut's University of Technology North Bangkok. Contract no. KMUTNB-61-GOV-03-71 and KMUTNB-61-GOV-B-45. P. Jaiban also would like to thank partial funding support from the Thailand Research Fund (TRF) and Office of the Higher Education Commission (OHEC), Ministry of Education through the TRF-OHEC Grant for New Researcher. Contract no. MRG6180109. A. Watcharapasorn would like to acknowledge partial funding support from Chiang Mai University.

References

- [1] E.H. El-Ads, N.F. Atta, A. Galal, A.R.M. El-Gohary, Nano-perovskite decorated carbon nanotubes composite for ultrasensitive determination of a cardio-stimulator drug, J. Elec. Chem. 816 (2018) 149–159.
- [2] A. Galal, H.K. Hassan, N.F. Atta, T. Jacob, Energy and cost-efficient nano-Ru-based perovskite/RGO composites for application in high performance supercapacitors, J. Colloid Interface Sci. 538 (2019) 578–586.
- [3] N.F. Atta, S.M. Ali, E.H. El-Ads, A. Galal, Nano-perovskite carbon paste composite electrode for the simultaneous determination of dopamine, ascorbic acid and uric acid. Electrochim. Acta 128 (2014) 16–24.
- [4] A. Galal, N.F. Atta, S.M. Ali, Investigation of the catalytic activity of LaBO₃ (B = Ni, Co, Fe or Mn) prepared by the microwave-assisted for hydrogen evolution in acidic medium, Electrochim. Acta 56 (2011) 5722–5730.
- [5] T.R. Shrout, S.J. Zhang, Lead-free piezoelectric ceramics: Alternatives for PZT? J. Flectroceram, 19 (2007) 111–124
- [6] J. Rödel, W. Jo, K.T.P. Seifert, E.M. Anton, T. Granzow, D. Damjanovic, Perspective on the development of lead-free piezoceramics, J. Am. Ceram. Soc. 92 (2009) 1153–1177.
- [7] J. Wu, D. Xiao, J. Zhu, Potassium-sodium niobate lead-free piezoelectric materials: past, present, and future of phase boundaries, Chem. Rev. 115 (2015) 2559–2595.
- [8] W. Liu, X. Ren, Large piezoelectric effect in Pb-free ceramics, Phys. Rev. Lett. 103 (2009) 257602.

- [9] P. Jaiban, S. Suwanwong, O. Namsar, A. Watcharapasorn, W. Meevasana, Simultaneous tuning of the dielectric property and photo-induced conductivity in ferroelectric Ba_{0.7}Ca_{0.3}TiO₃ via La doping, Mater. Lett. 147 (2015) 29–33.
- [10] B.H. Toby, R.B.V. Dreele, GSAS-II: the genesis of a modern open-source all purpose crystallography software package, J. Appl. Cryst. 46 (2013) 544–549.
- [11] Z.M. Wang, K. Zhao, X.L. Guo, W. Sun, H.L. Jiang, X.Q. Han, X.T. Tao, Z.X. Cheng, H.Y. Zhao, H. Kimura, G.L. Yuan, J. Yin, Z.G. Liu, Crystallization, phase evolution and ferroelectric properties of sol-gel-synthesized Ba(Ti_{0.8}Zr_{0.2})O₃-x (Ba_{0.7}Ca_{0.3})TiO₃ thin films, J. Mater. Chem. C 1 (2013) 522–530.
- [12] R.C. Pullar, Y. Zhang, L. Chen, S. Yang, J.R.G. Evans, A.N. Salak, D.A. Kiselev, A.L. Kholkin, V.M. Ferreira, N.M. Alford, Dielectric measurements on a novel Ba_{1-x}Ca_xTiO₃ (BCT) bulk ceramic combinatorial library, J. Electroceram. 22 (2009) 245–251
- [13] C.X. Li, B. Yang, S.T. Zhang, R. Zhang, W.W. Cao, Effects of sintering temperature and poling conditions on the electrical properties of Ba_{0.70}Ca_{0.30}TiO₃ diphasic piezoelectric ceramics, Ceram. Int. 39 (2013) 2967–2973.
- [14] P. Jaiban, A. Watcharapasorn, R. Yimnirun, R. Guo, A.S. Bhalla, Effects of donor and acceptor doping on dielectric and ferroelectric properties of Ba_{0.7}Ca_{0.3}TiO₃ lead-free ceramics, J. Alloys Compd. 695 (2017) 1329–1335.
- [15] X. Wang, H. Yamada, C.N. Xu, Large electrostriction near the solubility limit in BaTiO₃-CaTiO₃BaTiO₃-CaTiO₃ceramics, Appl. Phys. Lett. 86 (2005) 022905.
- [16] V. Pal, O.P. Thakur, R.K. Dwivedi, Structural investigation of Ca/Zr co-substituted BaTiO₃ through XRD and Raman spectroscopy, J. Alloys Comp. 741 (2018) 707–714
- [17] S.-H. Yoon, C.A. Randall, K.-H. Hury, Effect of acceptor (Mg) concentration on the resistance degradation behavior in acceptor (Mg)-doped BaTiO₃ bulk ceramics: I. Impedance analysis, J. Am. Ceram. Soc. 92 (2009) 1758–1765.
- [18] J. Miao, Z. Zhang, Z. Liu, Y. Li, Investigation on the dielectric properties of Mg-doped (Ba_{0.95}Ca_{0.05})(Ti_{0.85}Zr_{0.15})O₃ ceramics, Ceram. Int. 41 (2015) S487–S491.
- [19] Y. Pu, M. Yao, L. Zhang, M. Chen, Enhanced energy storage density of 0.55Bi_{0.5}Na_{0.5}TiO₃-0.45Ba_{0.85}Ca_{0.15}Ti_{0.85}Zr_{0.1}Sn_{0.05}O₃ with MgO addition, J. Alloys Comp. 702 (2017) 171–177.
- [20] M. Murata, K. Wakino, S. Ikeda, X-ray photoelectron spectroscopic study of perovskite titanates and related compounds: an example of the effect of polarization on chemical shifts, J. Electron Spectrosc. Relat. Phenom. 6 (1975) 459–464.
- [21] M.F. Toomey, K. Gao, G.P. Medis, E.B. Slamovich, J.A. Howarter, Hydrothermal synthesis and processing of barium titanate nanoparticles embedded in polymer films, ACS Appl. Mater. Interfaces 7 (2015) 28640–28646.
- [22] E. Chandrakala, J.P. Praveen, B.K. Hazra, D. Das, Effect of sintering temperature on structural, dielectric, piezoelectric and ferroelectric properties of sol-gel derived BZT-BCT ceramics. Ceram. Int. 42 (2016) 4964–4977.
- [23] F.A. Kröger, H.J. Vink, Relations between the concentrations of imperfections in crystalline solids. Phys. Status Solidi B 3 (1956) 307–335.
- [24] Y. Kozuka, Y. Hikita, T. Susaki, H.Y. Hwang, Optically tuned dimensionality crossover in photocarrier-doped SrTiO₃: onset of weak localization, Phys. Rev. B 76 (2007) 085129.
- [25] P.D.C. King, R.H. He, T. Eknapakul, P. Buaphet, S.K. Mo, Y. Kaneko, S. Harashima, Y. Hikita, M.S. Bahramy, C. Bell, Z. Hussain, Y. Tokura, Z.X. Shen, H.Y. Hwang, F. Baumberger, W. Meevasana, Subband structure of two-dimensional electron gas formed at the polar surface of the strong spin-orbit perovskite KTaO₃, Phys. Rev. Lett. 108 (2012) 117602.
- [26] J. Liqiang, Q. Yichum, W. Baiqi, L. Shudan, J. Baojiang, Y. Libin, F. Wei, F. Honggang, S. Jiazhong, Review of photoluminescence performance of nano-sized semiconductor materials and its relationships with photocatalytic activity, Sol. Energy Mater. Sol. Cells 90 (2006) 1773–1787.
- [27] C. Masingboon, T. Eknapakul, S. Suwanwong, P. Buaphet, H. Nakajima, S.K. Mo, P. Thongbai, P.D.C. King, S. Maensiri, W. Meevasana, Anomalous change in dielectric constant of CaCu₃Ti₄O₁₂ under violet-to-ultraviolet irradiation, Appl. Phys. Lett. 102 (2013) 202903.
- [28] E.A. Forsh, A.M. Abakumov, V.B. Zaytsev, E.A. Konstantinova, P.A. Forsh, M.N. Rumyantseva, A.M. Gaskov, P.K. Kashkarov, Optical and photoelectrical properties of nanocrystalline indium oxide with small grains, Thin Solid Films 595 (2015) 25–31.
- [29] O.P. Taran, A.B. Ayusheev, O.L. Ogorodnikova, I.P. Prosvirin, L.A. Isupova, V.N. Parmon, Perovskite-like catalysts LaBO₃ (B= Cu, Fe, Mn, Co, Ni) for wet peroxide oxidation of phenol, Appl. Catal. B 180 (2016) 86–93.